FLORIDA STATE UNIVERSITY

COLLEGE OF ARTS AND SCIENCES

EXPERIMENTAL INVESTIGATIONS ON THE NUCLEAR STRUCTURE OF THE NEUTRON-RICH NUCLIDES ^{44}S AND ^{20}O

By

DANIEL SANTIAGO-GONZALEZ

A Dissertation submitted to the
Department of Physics
in partial fulfillment of the
requirements for the degree of
Doctor of Philosophy

Degree Awarded:
Fall Semester, 2013

ProQuest LLC.
789 East Eisenhower Parkway
P.O. Box 1346
Ann Arbor, MI 48106 - 1346

Daniel Santiago-Gonzalez defended this dissertation on November 12, 2013.

The members of the supervisory committee were:

Ingo Wiedenhoever
Professor Directing Dissertation

Henry Fuelberg
University Representative

Nicholas E. Bonesteel
Committee Member

Paul D. Cottle
Committee Member

Alexander Volya
Committee Member

The Graduate School has verified and approved the above-named committee members, and certifies that the dissertation has been approved in accordance with the university requirements.

To Melina, my lovely wife

ACKNOWLEDGMENTS

The investigations exposed here could not have been realized without the guidance of my advisor, Dr. Ingo Wiedenhöver. From the moment I joined his group he demonstrated a level of knowledge and skills I had never seen before and that motivates me to become a better scientist. I thank him for all his support and advice throughout my stay at Florida State University.

I thank the members of my dissertation committee Nicholas Bonesteel and Henry Fuelberg for their helpful suggestions and comments and to Paul Cottle and Alexander Volya for many insightful discussions.

Many thanks to all the people involved in the experiment at the NSCL, in particular I appreciate the efforts of Alexandra Gade, Andrew Ratkiewicz, and Dirk Weisshaar. I also extend this recognition to E. C. Simpson, J. A. Tostevin and Alexander Volya, who provided the theoretical calculations that accompany the experimental results. In the same degree, I want to express my gratitude to the ANASEN collaboration, especially to Jeff Blackmon, Laura Linhardt and Kevin Macon from LSU.

My deepest gratitude to the all the staff members at the John D. Fox Superconducting Accelerator Laboratory, whose indispensable work keeps the lab and experiments running. Without them there would not be experiments at FSU. Particularly, I want to express my appreciation to Lagy Baby, whose commitment to the success the experiments at FSU is exemplary. I extend my sincere gratitude to the all graduate and undergraduate students who devoted countless hours to the data taking process. Without them there would not be any data to analyze.

I want to thank my family and friends for their support during my doctoral studies, especially to the Isotonics. Finally, I thank Jorge Piekarewicz for his friendship and for encouraging me to apply to FSU: one of the best decisions of my life.

TABLE OF CONTENTS

LIST OF TABLES

LIST OF FIGURES

ABSTRACT

Experimental results of two independent studies on the nuclear structure of the neutron-rich nuclei $^{44}_{16}$S and $^{20}_{8}$O are presented. A short introduction on the context of these studies within nuclear physics is given in chapter 1. Because of the fundamental differences between the experiments and analysis techniques the investigations have been separated in two chapters.

The investigation of ^{44}S, extracted via the two-proton knockout reaction from ^{46}Ar with intermediate beam energy, is presented in chapter 2. Four new excited states are identified, of which the first 4^+ state presents evidence of deformation, as suggested by line-shape simulations of the detected γ rays. This is also indicated by a shell-model calculation, where the deformation of the first 4^+ state originates in a neutron particle-hole configuration which is fundamentally different from the "intruder" configuration producing the ground state deformation and from the configuration describing the relatively long-lived isomeric 0^+ state. Consequently, not three coexisting shapes, rather three coexisting configurations are found in ^{44}S, corresponding to zero, one and two neutron particle-hole excitations.

In chapter 3, results from the analysis of the ^{19}O$(d,p)^{20}$O reaction in inverse kinematics using the active gas target detector array ANASEN are presented. In order to study the location and fragmentation of the $d_{3/2}$ orbital in ^{20}O, a beam of the short-lived ^{19}O was produced at the RESOLUT radioactive beam facility of the Florida State University. The ejected protons from the (d,p) reaction were measured with large solid angle coverage and for beam energies between 2.2 and 4.3 MeV/A. Data from the ^{17}O$(d,p)^{18}$O reaction was acquired to verify our experimental methods and analysis techniques.

CHAPTER 1

INTRODUCTION

The nuclear weak and strong interactions are of great importance in describing the world we live in, yet their exact nature remains largely unknown[1]. Understanding of the nuclear forces is central to explain phenomena such as the formation and abundance of the different atomic species, radioactive decay and the energy liberated in the stars[2].

Astounding progress has been made since the discovery of the atomic nucleus by Ernest Rutherford and his students H. W. Geiger and E. Marsden at the beginning of the XX-th century. In the decades following this discovery, results from experiments disclosed important properties of the structure of nuclei and the forces of their interacting particles. It was found that, almost all the mass of an atom is concentrated in its nucleus and, while the sizes of the atoms are of the order of 10^{-10} m, the sizes atomic nuclei are on the order of 10^{-14} – 10^{-15} m. Moreover, the nucleus is formed by particles almost two thousand times more massive than the electron, called protons and neutrons (or nucleons, in general). Neutrons do not carry net electric charge and protons have a +1 unit of elementary charge ($e = 1.602 \times 10^{-19}$ Coulombs). From the typical nuclear sizes and the fact that several protons, experiencing a repulsive electromagnetic interaction, can be confined in one nucleus, it can be inferred that the nuclear strong force has a short range and is predominantly attractive. Furthermore, the nuclear density remains approximately constant as the number of protons and neutrons increases, implying that the strong nuclear force *saturates*, this is, most nucleons interact only with a few neighbouring nucleons.

As more experimental data became available through the use of particle accelerators, new features of the nuclear structure were revealed. One of the most striking phenomena in nuclear physics is the sudden increase in the binding energy of nuclei with proton and neutron numbers 2, 8, 20, 28, 50, 82, as well as nuclei with 126 neutrons. These are the so-called *magic numbers* and represent major nuclear shell closings, which arise from considering that protons and neutrons inside the nucleus move rather independently in a central potential with spin-orbit coupling. This was first evidenced in 1949 by M. G. Mayer[3] and independently by Haxel, Jensen and Suess[4]. In recent years, the extension of the research frontier to nuclei far away from the valley of stability has revealed a weakening or even disappearance of shell closures in several neutron-rich nuclei[5]. The first experimental investigation in this dissertation, presented in chapter 2, focuses on the neutron-rich nucleus of $^{44}_{16}$S, where the erosion of the $N = 28$ shell gap enabled unexpected coexistence of the neutron configurations. Three essentially different neutron configurations in ^{44}S are examined from experimental data, acquired using the two-proton knockout reaction from $^{46}_{18}$Ar at intermediate energy. New excited states are reported and spin-parity quantum numbers are assigned where possible. The spins are determined based on the longitudinal momentum distributions of the projectile residues. The observed states include a state with spin-parity $J^\pi = 4^+$ at 2447 keV. Theoretical calculations suggests that this state has a strong prolate deformation, but that the origin of the deformation is based on a neutron configuration which is different from the configuration responsible for the ground state deformation of this nucleus.

Enormous improvements in the technology employed in nuclear accelerators and in the experimental techniques, allow the study of very short-lived exotic nuclei which in the past were only known to be found in stars or stellar explosions (such as novae), and even reaching the limits of bound nuclei at the proton and neutron driplines. This in turn, provides experimental data that challenges the current theoretical models describing the nuclear forces and the structure of nuclei. In particular, the anomalous behavior of the neutron dripline for oxygen isotopes has recently been interpreted in

terms of three-body forces[6]. The contribution of such forces can be determined by measuring the location and fragmentation of the single-particle energies along the oxygen isotopic chain. The nucleus of $^{20}_{8}$O, while it is 4 neutrons away from the dripline, can still provide substantial information on the single-particle energies of the neutron *sd* orbitals. In chapter 3, results from an experimental investigation to to study the location and fragmentation of the neutron $0d_{3/2}$ orbital in ^{20}O are presented. A beam of the short-lived ^{19}O was produced at the RESOLUT radioactive beam facility of the Florida State University and the new the active gas target detector ANASEN was used to measure the light-recoiling particles emitted from the reactions induced in its active volume.

CHAPTER 2

TRIPLE CONFIGURATION COEXISTENCE IN ^{44}S

2.1 Motivation

The emergence of nuclear shells in stable nuclei is among the most important and well documented phenomena in nuclear structure. The nuclear shell model was born as an effort to describe the added stability demonstrated by nuclei with proton and neutron numbers 2, 8, 20, 28, 50, 82, as well as nuclei with 126 neutrons. These are the so-called magic numbers and represent the major nuclear shell closings, which emerge from the splitting of the energy levels of a single particle in a central potential with spin-orbit coupling. This interpretation was proposed in 1949 by M. G. Mayer[3] and independently by Haxel, Jensen and Suess[4] in the same year.

Radioactive beam facilities have had a great impact in nuclear science as they have enabled scientists to study exotic nuclei, which would be otherwise unavailable simply because they would decay into more stable nuclei. From the study of these exotic nuclei, we have learned that the nuclear shells change and some of them erode as we move away from stability. At present, the largest of the neutron shell closures that is accessible to experiments close to the neutron dripline is $N = 28$, and the narrowing of the shell gap was recently established experimentally [7, 8, 9].

Investigations of how the narrowing of the $N = 28$ gap affects nuclear structure have been focused on how two-particle two-hole "intruder" configurations, resulting from the promotion of a pair of neutrons across the $N = 28$ gap, cause deformation in

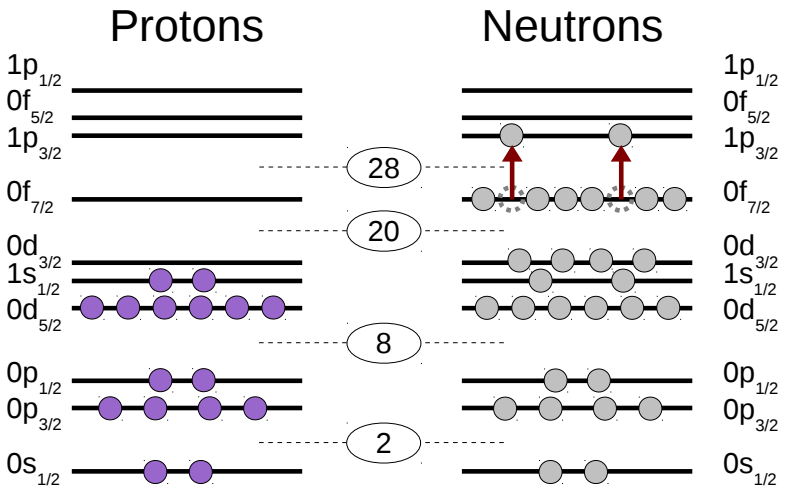

Figure 2.1: Depiction of the "intruder" configuration in the ground state of ^{44}S, where two neutrons have been promoted across the $N = 28$ shell gap present in stable nuclei.

these isotones. This particle configuration is schematically depicted in Figure 2.1. As a consequence of the narrowing of the shell gap, a rich and complex nuclear structure is expected with the possibility of various particle configurations coexisting in one nucleus. Experimental works in heavier nuclei point out that, in single-closed-shell nuclei, a low-lying 0^+ appears as a consequence of the intruder configuration[10].

The nucleus of ^{44}S with 16 protons and 28 neutron is an excellent candidate for studying the effects of the narrowing of the $N = 28$ gap and to test the current theoretical models for exotic nuclei in the intermediate mass region. From a technical point of view, ^{44}S is close but no longer at the limits of the current technological capabilities of the largest radioactive beam facilities, thus it can be produced in large enough quantities allowing us to study its properties in a level of detail never achieved before.

2.2 Previous Experiments on ^{44}S

Not much was known about the nuclear structure of ^{44}S before the decade of the 1990s. Experimental limitations and low production cross sections made infeasible

at the time the study of the $N = 28$ isotones for elements lighter than Ar ($Z = 20$), but since the early 1990s some efforts have been made to study this exotic nucleus. Experimental techniques and results from selected publications on ^{44}S are summarized in this section.

In 1993, a successful measurement of the decay properties of ground state of ^{44}S was achieved in an experiment performed at the Grand Accélérateur National d'Ions Lourds (GANIL) by Sorlin *et al.* [11]. Motivated in part by a nuclear astrophysics stand point, the production and implantation of ^{44}S yielded a precise measurement of the half-life of the ground state of this nucleus, found to be $t_{1/2} = 123(10)$ ms[1]. The nuetron-rich ^{44}S was produced via fragmentation of a 60 MeV/nucleon beam of ^{48}Ca impinging onto a solid ^{64}Ni target. The fragments were separated in-flight by the LISE spectrometer[14] and the desired nuclei were selected by using a telescope of two 300-μm thick Si detectors and one final 5500-μm thick Si(Li) detector where the nuclei were implanted and the decay times measured. Although the authors of Ref. [11] acknowledge that comparing the measured half-life with its theoretical counterpart may not reflect many details of the nuclear structure of ^{44}S, it is interesting to notice that their results were best reproduced by assuming some degree of *oblate* deformation. Naively, one would have expected for this semimagic nucleus a near spherical shape to produce the most accurate results, however, this was not the case.

The first observation of the transition from the first excited state ($J^\pi = 2^+$) to the ground state ($J^\pi = 0^+$) in ^{44}S was done in 1997 at the National Superconducting Cyclotron Laboratory (NSCL) in a Coulomb excitation experiment by Glasmacher *et al.* [15]. A radioactive beam of ^{44}S was produced from fragmentation of a beam of ^{48}Ca onto a thick ^{9}Be target. The ^{44}S beam travelling at approximately 27% the speed of light (corresponding to a total energy of 35 MeV/nucleon) was directed to a solid ^{197}Au target, where the excitations occurred. The excited ^{44}S was then transported to a 0°-telescope of plastic detectors, where the fragment's energy loss and total energy were measured. The γ rays were detected by an array of NaI(Tl)

[1]More current experiments measured the half-life of ^{44}S at $t_{1/2} = 100(1)$ ms [12, 13].

detectors surrounding the gold target. Doppler corrections were necessary due to the relativistic effects of the fast moving sources as shown in Figure 2.2. The peak observed at 1297(18) keV was formed by γ rays emitted from the deexcitation of the first excited state whose spin-parity was determined as 2^+. The electric quadrupole reduced transition probability was reported as $B(E2, 0^+_{\text{g.s.}} \rightarrow 2^+_1) = 314(88)\ e^2\text{fm}^4$ and a *reduced* quadrupole deformation parameter

$$\beta_2 = 4\pi \frac{\sqrt{B(E2 : 0^+_{\text{g.s.}} \rightarrow 2^+_1)}}{3ZR_0^2 e} \tag{2.1}$$

$$\beta_2 = 0.258(36), \tag{2.2}$$

where $R_0 = 1.2A^{1/3}$ fm. Relativistic mean-field calculations predict a statically deformed prolate ground state with a $\beta_2 = 0.31$. Notice the contrast with the oblate deformation suggested by Sorlin *et al.* [11]. The authors concluded that the relatively large $B(E2, 0^+_{\text{g.s.}} \rightarrow 2^+_1)$ and β_2 values demonstrate that ^{44}S has a collective nature.

In 2005, in another experiment performed at GANIL, Grévy *et al.* [16] discovered an isomeric 0^+ state in ^{44}S with an energy of excitation $E_{\text{exc}} = 1365(1)$ keV. To produce ^{44}S, a 60-MeV/nucleon ^{48}Ca primary beam was fragmented on a thick beryllium target. Fragments were separated by the LISE3 spectrometer[17] and selected by means of their energy loss and magnetic rigidity. A telescope of Si detectors provided mass and charge identification for the fragments. The selected nuclei were implanted in a Kapton foil and a thick Si detector, located downstream from the implantation foil, was used to veto undesired events. An array of Si(Li) detectors, perpendicular to the beam axis and above the implantation foil, was arranged for the detection of electrons and two segmented Ge detectors, placed below the foil, were used for the γ rays. Data from the monopole ($E0$) and delayed quadrupole ($E2$) transitions was used to infer the presence of an isomeric 0^+ state with 1365(1) keV of excitation and a half-life of 2.3(3) μs. The presence of a low-lying 0^+ isomer is considered a feature of coexistence between spherical and deformed shapes in the nuclear mean field. Shell model calculations were performed assuming that the two 0^+ states are described by a

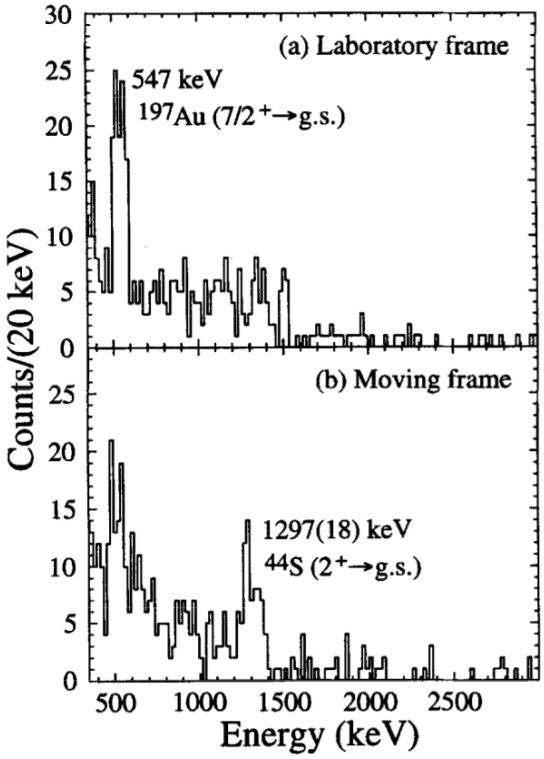

Figure 2.2: Taken from [15]. (a) Spectrum of γ rays, in the laboratory frame, in coincidence with the ^{44}S detected in the 0°-telescope. The peak at 547 keV is due to the deexcitation of the $7/2^+$ state in ^{197}Au. (b) Same data after applying event-by-event Doppler corrections assuming $v = 0.276c$.

mixture of closed-shell and neutron-particle neutron-hole excitations. The calculated levels accurately described the observations of Grévy *et al.* [16].

In 2010, results form a reiteration of the previously mentioned experiment at GANIL were published by Force *et al.* [18], confirming the findings from Ref. [16] and providing further insight on the shape coexistence in this nucleus. The monopole strength $\rho^2(E0, 0_2^+ \rightarrow 0_1^+)$ and reduced transition probability $B(E2, 2_1^+ \rightarrow 0_2^+)$ were determined to be $8.7(7) \times 10^{-3}$ and $8.4(26)$ $e^2\text{fm}^4$, respectively. The authors explained the interaction between the "normal" configuration, in which the neutrons are confined to the orbits below the $N = 28$ gap, and the intruder configuration with a two-level mixing model for the wavefunctions of the 0^+ ground state and the 0^+ isomer. These wavefunctions are described in terms of a linear combination of or-

thogonal wavefunctions that represent a spherical ($|0_S\rangle$) and a deformed ($|0_D\rangle$) state, this is,

$$|0_1^+\rangle = \cos\theta|0_D\rangle + \sin\theta|0_S\rangle \quad (2.3)$$

$$|0_2^+\rangle = -\sin\theta|0_D\rangle + \cos\theta|0_S\rangle, \quad (2.4)$$

where θ is the mixing angle. From Ref. [19] it is known that the mixing angle can be extracted by the relation

$$\tan^2\theta \sim \frac{B(E2, 2_1^+ \to 0_2^+)}{B(E2, 2_1^+ \to 0_1^+)}. \quad (2.5)$$

The reduced transition probability $B(E2, 0_1^+ \to 2_1^+)$ was measured by Glasmacher *et al.* [15] at 314(88) e^2fm^4. The value for the inverse transition can be obtained by recalling[1] that,

$$\frac{B(E2, J_i \to J_f)}{B(E2, J_f \to J_i)} = \frac{2J_f + 1}{2J_i + 2}. \quad (2.6)$$

Then, $B(E2, 2_1^+ \to 0_1^+) = 63(18)$ e^2fm^4. From this value and $B(E2, 2_1^+ \to 0_2^+) = 8.4(26)$ e^2fm^4 the authors were able to obtain the mixing angle $\theta \sim 20°$ (maximum mixing corresponds to $\theta = 45°$). Theoretical calculations predict stronger mixing with $\theta_{\text{theo}} = 26°$. It can be assumed that each state presents an intrinsic deformation parameter, β_D and $\beta_S \equiv 0$, before mixing. The following relation between the mixing angle, the monopole strength and these deformation parameters can be found in Ref. [20],

$$\rho^2(E0) = \left(\frac{3Ze}{4\pi}\right)^2 \sin^2\theta\cos^2\theta\left(\beta_D^2 - \beta_S^2\right)\Big)^2 \quad (2.7)$$

The value $\beta_D = 0.274$ satisfies the equation above and is in good agreement with the value obtained for the ground state deformation in Ref. [15] of $\beta = 258(36)$ and with shell-model calculations $\beta = 0.25$. Altogether these findings again point towards a deformed-spherical shape coexistence in ^{44}S.

Summarizing the mentioned experimental works, it is now known that the ground state of ^{44}S has a half-life of 100(1) s. Also, two excited states at almost degenerate energies corresponding to a 2_1^+ at 1329(1) keV and a 0_2^+ at 1365(1) keV are present

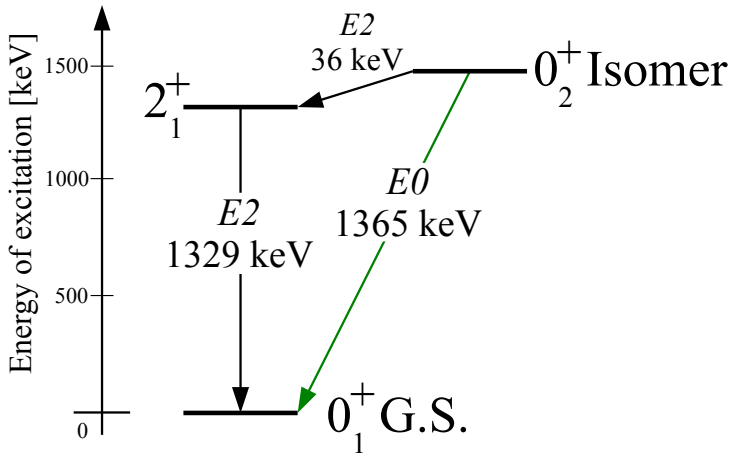

Figure 2.3: Level scheme of ^{44}S as of 2010. $E2$ ($E0$) transitions are represented by black (green) arrows and the energy of the emitted γ ray (electron) is shown under the transition's label.

in this nucleus. The isomeric 0_2^+ state has a half-life of $t_{1/2} = 2.3(3)$ μs. Two reduced quadrupole transition probabilities and the monopole strength, $\rho^2(E0 : 0_2^+ \rightarrow 0_1^+)$ have been measured. From these values, combined with shell-model calculations and a two-level mixing model, it was found that ^{44}S exhibits shape coexistence between a prolate-deformed ($\beta \simeq 0.25$) and a spherical state. The wavefunctions of the ground state and isomeric 0_2^+ can be expressed as linear combinations of the mentioned states with a mixing angle of 20°. In Figure 2.3, the level scheme of the well established states in ^{44}S known by 2010 is presented.

2.3 Experiment

The present experiment was performed at the NSCL in March of 2009. A beam of the radioactive isotope ^{46}Ar was produced via fragmentation of a 140-MeV/nucleon primary beam of ^{48}Ca provided by the Coupled Cyclotron Facility. The primary beam was fragmented on a 705 mg/cm^2 thick beryllium target, and the fragmentation products were separated in the A1900 fragment separator[21]. The separator selected a secondary beam of ^{46}Ar at 99.9 MeV/nucleon, which had a momentum spread of

$\pm 1.3\%$ and a purity greater than 90%. The rate of ^{46}Ar particles impinging on the secondary target averaged 7×10^5 particles/s. The two-proton knock-out reactions were induced on a secondary beryllium target of thickness 188 mg/cm^2. The residual projectile-like nuclei were detected in the S800 spectrograph[22]. γ rays emitted at the secondary target location were detected using SeGA[23], an array of 17 segmented germanium detectors, in coincidence with the residues in the S800 spectrograph. The total peak efficiency of the SeGA array for γ rays emitted in-flight ($v/c = 0.4211$) was 2.5% at 1 MeV and 1.4% at 2 MeV. In the following subsections a brief description of the main experimental components is provided.

2.3.1 Coupled Cyclotron Facility

A cyclotron is a type of particle accelerator where the ions are injected close to its center and then are accelerated outwards following a spiral trajectory. The ions are confined to a relatively small volume by applying a strong magnetic field perpendicular to their velocity and are accelerated by a rapidly varying electric field. This technology has been available since the 1930s but with the introduction of superconducting materials to this type of accelerators a new generation of superconducting cyclotrons was developed and the K500, completed in 1982, was the first of its kind[24]. At the NSCL the Coupled Cyclotron Facility (CCF) consists of two superconducting cyclotrons called K500 and K1200 joint by a coupling line which comprises a superconducting dipole, 9 superconducting quadrupoles and steering magnets[25]. For our experiment the CCF delivered electron striped ions of ^{48}Ca^{+20} as primary beam with 140 MeV/nucleon travelling at approximately 50% the speed of light. The primary beam was impinged on a 705 mg/cm^2 thick beryllium target, then the fragmentation products continued their journey to the A1900 fragment separator.

2.3.2 A1900 Fragment Separator

At the NSCL, the large-acceptance high-resolution fragment separator A1900 is located a few meters down the beam line from the CCF and after the production

target. At the energies used in this experiment, the collisions of the primary beam onto the ^{9}Be target produced a cocktail of nuclides all travelling with velocities similar to the primary beam velocity. The purpose of the A1900 is to filter most of the products and select a radioactive beam with as few contaminants as possible.

When dealing with beams of charged particles a term very frequently mentioned is the *magnetic rigidity* or $B\rho$. This quantity (or product of quantities) is simply derived from the Lorentz force experienced by a charged particle, of charge q and mass m, travelling through a constant magnetic field, $\boldsymbol{B}$, perpendicular to the particle's velocity, $\boldsymbol{v}$. In absence of an electric field and neglecting all other interactions, the Lorentz force is equal to the total (centripetal) force that the particle experiences at a distance ρ from the center of curvature. In magnitude, this can be expressed as,

$$F_{\text{Lorentz}} = F_{\text{centripetal}} \tag{2.8}$$

$$qvB = mv^2/\rho \tag{2.9}$$

$$B\rho = mv/q \tag{2.10}$$

Although this result has been derived from *classical* dynamics, it can be demonstrated that this same expression is obtained from a fully relativistic analysis (see for example Landau and Lifshitz [26]).

An advantage of having a massive primary beam with relatively large kinetic energy ($\sim$ 150 MeV/nucleon) impinging on a production target made of light nuclei (such as ^{9}Be) is that all the created products (or fragments) move approximately with the same velocity. Therefore, setting a $B\rho$ value allows selection of products with specific m/q ratio. Since the mass of a nucleus is proportional to its mass number, A, and (in a fully electron-stripped nucleus) its charge is proportional to its atomic number, Z, the selection of m/q is equivalent to A/Z.

A schematic layout of the CCF connected to the A1900 is shown in Figure 2.4. The fragment selection process can be summarized as follows: the magnetic rigidity of the superconducting dipole magnets in the first section (after the production target and before "image 2") is set, thus selecting A/Z; then, the fragments pass through

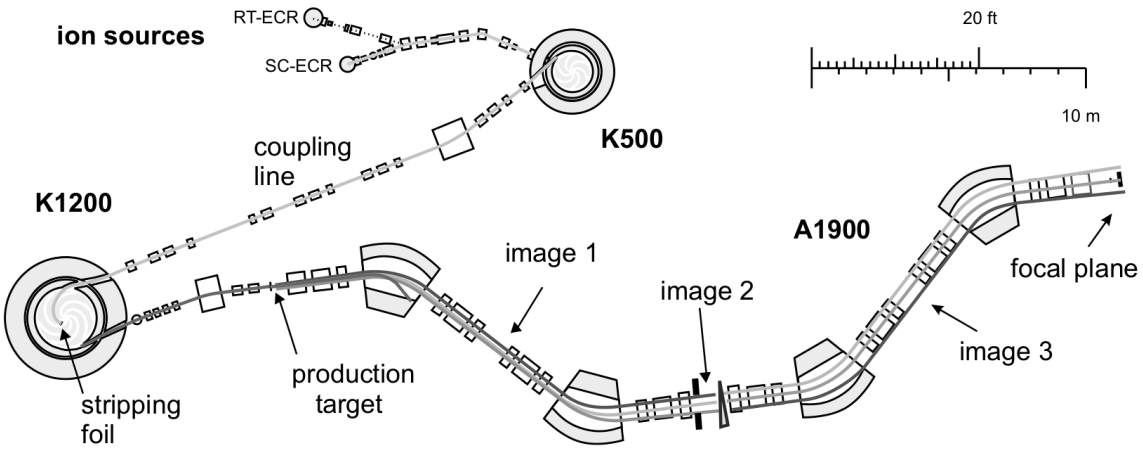

Figure 2.4: Segment of the beam line at the NSCL. The coupled superconducting cyclotron accelerators are labeled as K500 and K1200. The beam hits the production target and then the ejectiles are *filtered* through the fragment separator A1900, which begins after the production target and ends before the focal plane. Image taken from [21].

the "wedge" where they loose energy proportionally to their charge square, this is $\Delta E \sim Z^2$; further separation is achieved by setting the $B\rho$ of the superconducting dipoles in the last section (after the wedge and before the focal plane) corresponding to the A/Z ratio of the fragment of interest, accounting for the new value of the velocity due to the energy lost in the wedge.

Figure 2.4 also shows an illustration of the separation of different fragments. These are represented by the solid lines in shades of gray emerging from the K1200 cyclotron and following the beam line through the A1900. Notice how all of them start together but because of the fixed rigidity of the magnets and the differences in the energy loss in the wedge they get separated, hence creating a beam from a selected fragment. In practice, it is common for radioactive beams to show some contamination by other fragments with similar charge to mass ratios. In the case of the present experiment the A1900 delivered a beam of the radioactive ^{46}Ar with purity of approximately 90%.

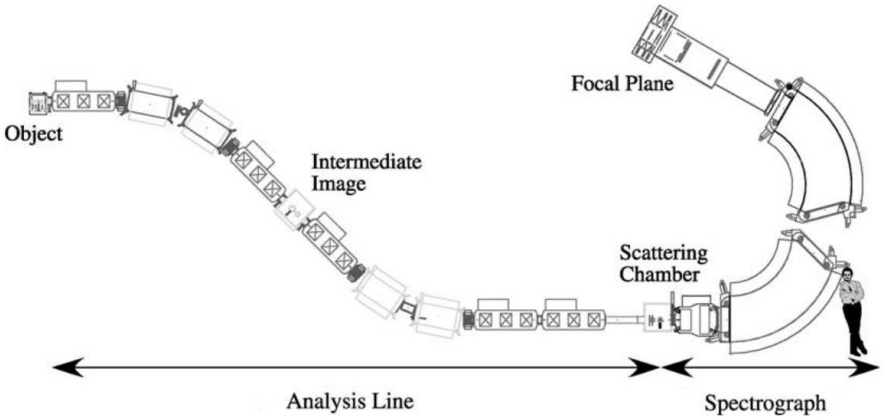

Figure 2.5: Schematic diagram of the S800. Image taken from [22].

2.3.3 The S800 Spectrograph

After the beam leaves the A1900 it enters another analysis line which is connected to a high resolution spectrograph. This system is called the S800 spectrograph. The high resolution is achieved via an analytical reconstruction method in which the aberrations of the spectrograph are calculated *a priori* from the magnetic field maps and used directly to correct the raw data. The focal plane detector system of the S800 consists of a pair of cathode readout drift chambers (CRDC) located about 1 m apart, followed by a multi-segmented ionization chamber and four large plastic scintillators of thicknesses 3 mm, 5 cm, 10 cm and 20 cm, respectively. The active area covered by these detector is about 60 cm by 30 cm. The CRDCs provide a measurement of position and angle in both dispersive and non-dispersive planes, the ion chamber gives an energy loss measurement and the plastic scintillators timing and trigger information. The position resolution achieved on the CRDCs is about 0.5 mm in both directions[22].

For the present experiment, the secondary target was placed at the scattering chamber shown in Figure 2.5 and the beam of ^{46}Ar delivered to it. The S800 was used for identification of ^{44}S and the neighboring reaction channels, and for measuring the momentum of the residual nuclei.

2.3.4 The Segmented Germanium Array

Once the radioactive beam of ^{46}Ar has been selected, it is transported through the beam line to the secondary target which, like the production target, is made of ^{9}Be. In the present experiment the thickness of the secondary target was 188 mg/cm^2. The Segmented Germanium Array (SeGA) was used to detect the γ rays produced at the place were the radioactive beam encounters the secondary target. In the configuration used for this experiment, known as "classic SeGA", the germanium crystals are arranged in two rings, one at 90° and the other at 37° with respect to the axis of the beam line. Normally, in this configuration, the 90° ring has 10 segmented germanium detectors while the 37° ring has 8 of them, however when SeGA is used in combination with the S800 one of the detectors in the forward ring must be removed due to space limitation. Furthermore, 2 crystals were not available for the present experiment, hence, 9 germanium crystals were accommodated in the 90° ring and 6 of them in the 37° ring.

Each of the detectors has a cylindrically-symmetric n-type coaxial germanium crystals. These crystals have an external diameter of 70 mm and length of 80 mm. The outer contacts of the detectors are electronically divided into eight 10 mm wide disks in the lateral direction, and four-fold radial segmentation for a total of 32 segments[23]. A schematic diagram of the segmentation in one germanium crystal is presented in Figure 2.6 (a). Higher angular resolution is achieved from the lateral segmentation of the crystals as shown schematically in Figure 2.6 (b), where, in a hypothetical event, two γ rays have been detected in different segments of the crystals (highlighted in green). The angles at which the γ rays where emitted are approximately the same as the angle at which the segments are positioned with respect to the target.

In actual experiments, the beam particles interact with the target and some of the residual nuclei will eject γ rays in their deexcitation. The higher angular resolution in the SeGA crystals is instrumental for accurately reconstructing the energy of γ rays in the rest frame of their sources when these are emitted by fast-moving nuclei close or at the target position. This correction arises as a consequence of the relativistic

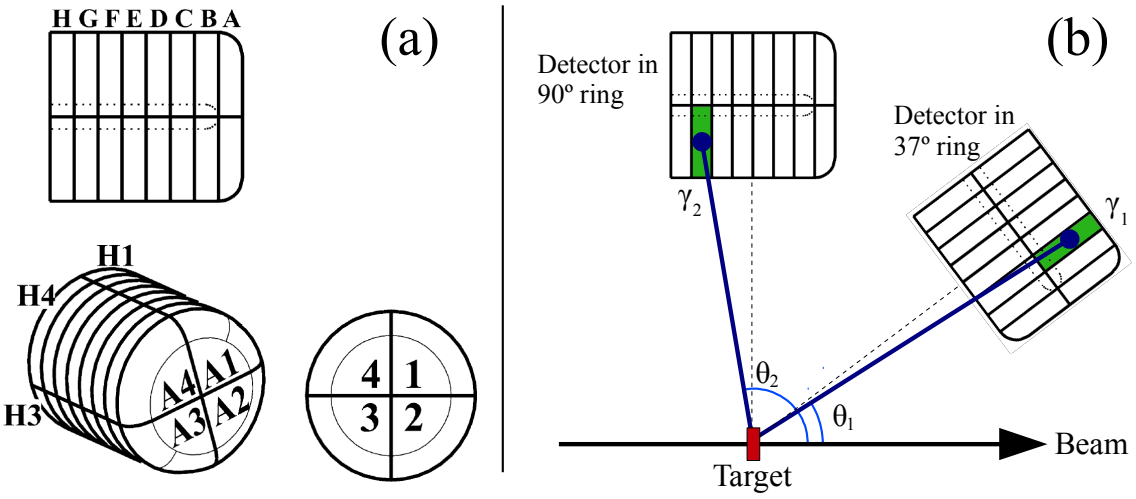

Figure 2.6: (a) Schematic of a germanium crystal in SeGA showing the 32 segments and its geometry (taken from [23]). (b) Schematic representation of an event in which two γ rays have been detected in different segments, highlighting the higher angular resolution due to the lateral segmentation in each crystal.

Doppler effect and is presented in more detail in appendix A. If the γ ray is emitted, not at the target position, but further downstream along the beam path, the error in the angle of detection will cause a broadening of the reconstructed γ-ray energy. This effect is discussed in more detail in section 2.5.3.

2.4 Results

In the previous section, the experimental equipment was described in the same order as the one followed by beam particles as they traversed the beam line. In a similar way, in the following subsections, the experimental results of the current study are presented in a sequence that follows the steps of the data analysis process which finalized in the assembly of the level scheme of ^{44}S, shown in Figure 2.7 (left), and in the estimation of cross sections of direct population of the observed excited states, shown in Table 2.3. In the level scheme of ^{44}S, the excitation energies and their decay paths (denoted by arrows) were deduced from the analysis of the γ rays emitted in the deexcitation of ^{44}S (speculative transitions are denoted by dotted lines), the spin

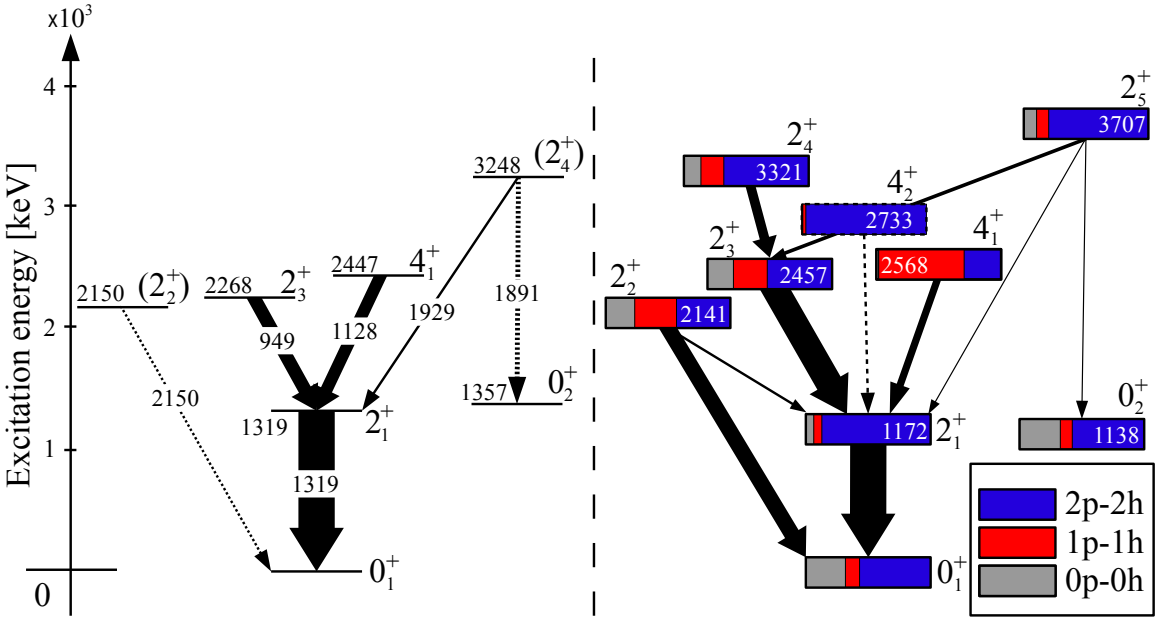

Figure 2.7: (Left) Experimental level scheme of ^{44}S. The arrow widths are proportional to the observed intensity of the transitions. (Right) Level and transition scheme predicted by the shell model (see sec. 2.5.1) where each state is depicted by a box with the fraction of its neutron n-particle n-hole configuration (see sec. 2.5.2). The arrow widths represent the calculated γ intensities based on population cross sections and subsequent γ-decay branching ratios, normalized to the strength of the $2^+_1 \rightarrow 0^+_1$ transition. All predicted transitions calculated larger than 3% of the ground state transition intensity are shown.

assignments to the excited states are based on longitudinal momentum distributions of the residual ^{44}S in coincidence with specific γ rays (tentative assignments are enclosed by parenthesis), the arrow widths are proportional to the transition strengths for which the detection efficiency had to be obtained. There is excellent agreement between the experimental and theoretical level schemes shown in Figure 2.7 (right), although the details of the calculations are not discussed until section 2.5. The most striking feature is the prediction of the 4^+_1 state with a fundamentally different neutron particle-hole configuration, which is discussed in section 2.5.2.

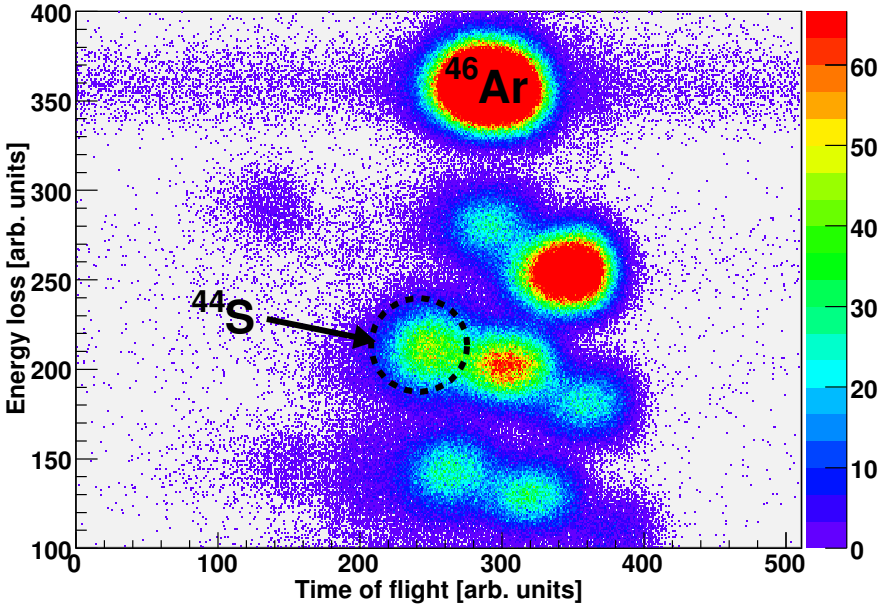

Figure 2.8: Spectrum of residual nuclei identified in the S800 spectrograph. The particles labelled ^{46}Ar correspond to scattered beam particles. The vertical axis displays the energy loss of nuclides measured in the focal plane, and the horizontal axis represents a path-corrected time-of-flight signal measured between a focal plane detector and the accelerator RF reference.

2.4.1 Identification of ^{44}S

The first step in the data analysis is to separate ^{44}S from all other residues. Once the radioactive beam of ^{46}Ar collides with the solid beryllium target located at the focal plane of the S800, γ rays from a multitude of nuclear reactions are detected by the germanium crystals of SeGA. An almost continuous distribution of γ-ray energies would be observed if one were to plot them in a histogram. To distinguish the γ rays coming from the deexcitation of ^{44}S from all other γ rays we use energy loss and time of flight information of the residual nuclei, which are assumed to be fully-stripped of their electrons. In the ionization chamber, located at the end of the S800, the amount of energy loss by the residual nuclei from interactions with the gas molecules is proportional to Z^2, thus residues with larger atomic number (Z) loose more energy. On the other hand, isotopes with larger mass number (A) have

differences in the path-corrected time-of-flight signal measured between a focal plane detector and the accelerator RF reference. Although it may seem counter-intuitive, the way the time-of-flight signal is measured is such that a smaller signal corresponds to a slower particle, or in other words a longer time of flight. These two quantities, the energy loss and the time of flight, allow us to separate different residual nuclei detected by the S800 as show in Figure 2.8. A graphical cut (or gate) can be drawn around the points corresponding to ^{44}S which would then be utilized by the data-sorting codes.

2.4.2 γ Spectra

The γ-ray spectrum in coincidence with the ^{44}S residual nuclei, known as γ-singles spectrum, is shown in Figure 2.9. The data used to generate this spectrum has been Doppler-corrected in an event-by-event basis so that the measured γ-ray energies appear as in the rest frames of the residual nuclei. The experimental uncertainties on the γ-ray energies are 0.5%. The strongest γ-ray peak in the spectrum is at 1319(7) keV. It was first observed in 1997 by Glasmacher *et al.* [15] at 1297(18) keV and assigned to be the γ ray emitted in the $2_1^+ \rightarrow 0_1^+$ transition. All other peaks had never been observed before. One can witness the advancements in the experimental techniques and equipment by comparing the first published γ-singles spectrum of ^{44}S from Glasmacher *et al.* [15] (Figure 2.2) to the one from the present experiment obtained 12 years later.

The inset in Figure 2.9 shows an enlarged version of the γ-singles spectrum in the range $E_\gamma \in [1700, 2400]$ keV. Two peaks only 38 keV apart with energies of 1891(10) and 1929(10) keV have been identified. This postulation can be corroborated by the spectrum of γ rays in coincidence with the 1319-keV γ ray and ^{44}S residue, shown in Figure 2.10. This type of spectrum is known as $\gamma\gamma$ coincidence spectrum. Three peaks seen in the γ-singles spectrum, at 949(5), 1128(6) and 1929(10) keV, are also evident in the $\gamma\gamma$ coincidence one whereas there is no indication of the 1891-keV peak. This firmly establishes the existence of excited states at 2268(8), 2447(9) and

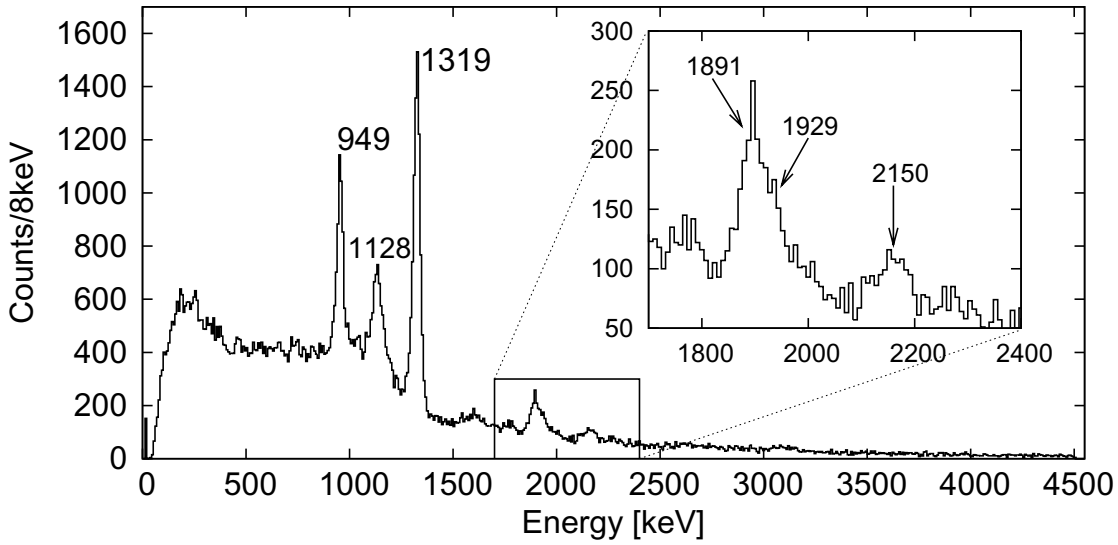

Figure 2.9: Doppler-corrected ($v/c = 0.4211$) energy of γ rays detected in coincidence with the ^{44}S residues. Inset shows a close-up of the 1700-2400 keV region where three less intense photo peaks are identified.

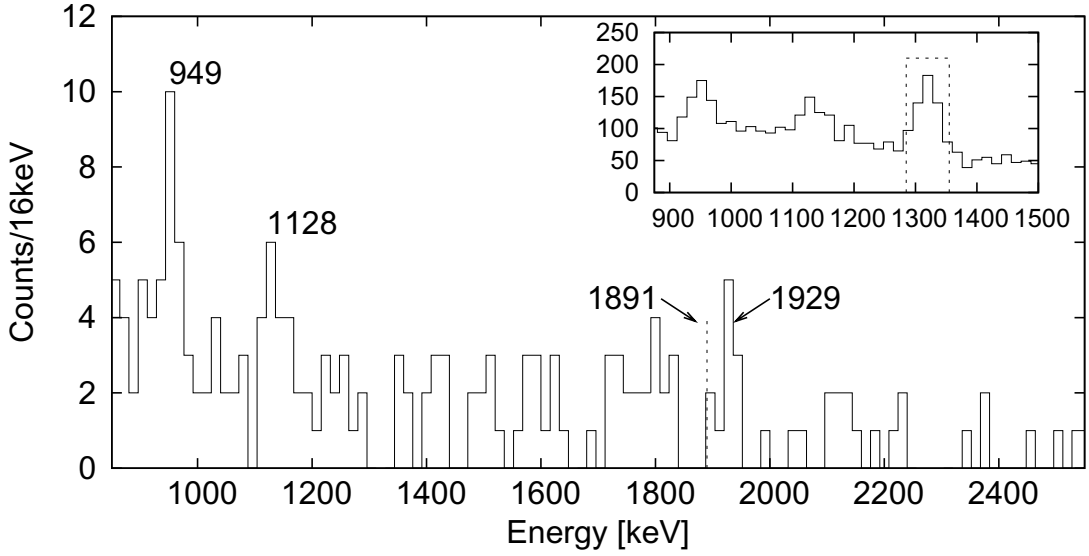

Figure 2.10: Doppler-corrected energy of γ rays detected in coincidence with the 1319-keV γ rays emitted from a ^{44}S nucleus. Inset: Projected spectrum of $\gamma\gamma$ events showing energy coincidence window in dotted lines.

3248(12) keV which decay to the first excited state. Figure 2.9 also shows γ rays at 2150 keV that are not seen in the 1319-keV coincidence spectrum. The statistics in the spectra gated on the 949-, 1128- and 1929-keV peaks are not sufficient to establish coincidence relationships among these three γ rays.

Force *et al.* [18] reported the existence of two states in ^{44}S, the 2_1^+ 1st excited state at 1329(1) keV (1319 keV in the present experiment) and the isomeric 0_2^+ at 1365(1) keV, separated by 36 keV. Within the experimental error, this energy gap is the same as the one between the 1891- and 1929-keV γ rays observed in the current experiment. On this basis, it is suggested that the 1891-keV γ ray is emitted in the deexcitation of the 3248-keV excited state to the isomeric 0_2^+, which in our case would present an excitation energy of 1357(15) keV. The only decay of the 0_2^+ state would be to the ground state via the emission of conversion electrons, so this decay could not be observed in the present experiment. The 3248-keV state would most likely have a spin-parity of 2^+ allowing decay to the 2_1^+ and 0_2^+ via $E2$ transitions.

With the information exposed thus far, the existence of excited states at 2268(8), 2447(9) and 3248(12) keV which decay to the first excited state is firmly established. Another exited state is tentatively placed at 2150(11) keV. The deduced level scheme shown in Figure 2.11 does not yet include the relative transition strengths but they are calculated with the results laid out in section 2.4.5. A discussion of the spin assignment of the first two states is presented in section 2.4.4.

Sohler *et al.* [27] published a level scheme for ^{44}S deduced from γ rays observed during the fragmentation of a beam of ^{48}Ca at intermediate energy. The only γ transition that is unambiguously common to the spectra of Sohler *et al.* [27] and the present work is the $2_1^+ \rightarrow 0_1^+$. The energy of the γ rays ejected in this transition was quoted as 1350(10) keV while here is 1319(7) keV. Sohler *et al.* [27] also assigned a 988-keV transition to ^{44}S and assumed it deexcites a state at 2632 keV. There is a 31 keV difference between the 2_1^+ state energies quoted here and by Sohler *et al.* [27], so there is a remote possibility that the 949-keV γ ray observed here is identical to the one at 988(15) keV reported by Sohler *et al.* [27]. However, if the two γ rays

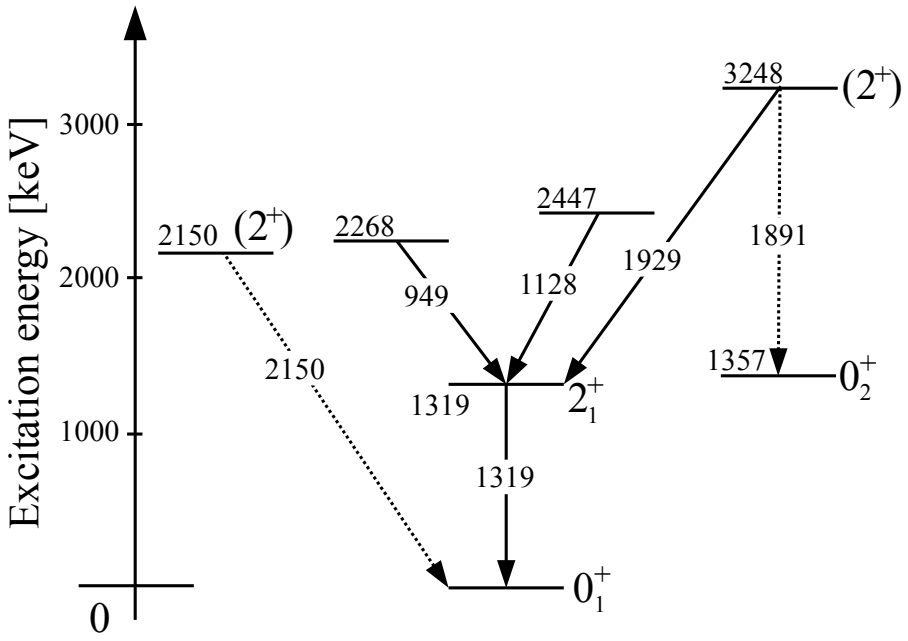

Figure 2.11: Experimental level scheme of ^{44}S obtained only from the analysis of the γ-singles and $\gamma\gamma$ spectra. Speculative transitions and spin-parities are denoted by dotted lines and by numbers in parenthesis, respectively.

are identical, it is clear that the γ ray was misplaced in the level scheme of the the previous study.

2.4.3 Detection Efficiency

A precise measurement of the detection efficiency of SeGA is necessary in order to accurately compare the strength of the observed transitions in ^{44}S. It is well-known that the efficiency of germanium detectors, such as the ones used in SeGA, decreases as the γ-ray energy increases. Moreover, when dealing with relativistic beams, a *boosted* efficiency is required to account for the relativistic Doppler effect. For the present experiment data from a ^{152}Eu γ-ray source was used to estimate the detection efficiency in the laboratory reference frame.

The detection efficiency is a measurement of the probability of a particle to be absorbed in the active volume of a detector. Since uncharged particles, such as photons, can travel large distances through material without interacting, knowing

the detection efficiency is necessary to estimate the number of particles that actually traversed the detector's active volume for a given number of pulses counted. There are several ways in which counting efficiencies can be categorized. In this work the *absolute* efficiency is used and it is defined as,

$$\epsilon_{\text{abs}} \equiv N_{\gamma,\text{obs}}/N_{\gamma,\text{emit}}, \tag{2.11}$$

where $N_{\gamma,\text{obs}}$ is the number of observed γ rays (or recorded pulses) and $N_{\gamma,\text{emit}}$ is the number of radiation quanta emitted by the source. The absolute efficiency not only depends on the properties of the detector material but also on its geometry, on the distance from the source to the detector and on the energy of the incident particle. Because of these reasons, absolute detection efficiency of less than 1% is typical for each detector in SeGA when placed 25 cm away from a γ-ray source[23].

In naturally decaying radionuclides, such as Europium-152, the number of decays of a species of nuclei per unit time, also known as *activity* (A), is proportional to the number of nuclei of the same species existing at that time (N),

$$A(t) = -\frac{dN}{dt} = \lambda N(t), \tag{2.12}$$

where λ is a positive real number known as the *decay constant*. The solution of the differential equation 2.12 is

$$N(t) = N_0 e^{-\lambda t}, \tag{2.13}$$

where N_0 is the number of nuclei at time $t = 0$. The parameter known as the *half-life* is the time it takes for these radionuclides to dacay from N_0 to $N_0/2$, therefore, $\lambda = \ln 2/t_{1/2}$. After defining the initial activity as $A_0 \equiv \lambda N_0$, the activity at a time t can then be written as

$$A(t) = A_0 e^{-\ln 2(t/t_{1/2})}. \tag{2.14}$$

The half-life of ^{152}Eu is $t_{1/2} = 13.528(14)$ years [28] and the activity of the γ-ray source used for our calibration was reported in May 1st, 1978, to be $A_0 = 3.131(44) \times 10^5$ decays/s [29]. The timespan from May 1st, 1978 to March 27th, 2009 (date of initial

calibration run) is $t_{\text{span}} = 30.90$ years[2]. By substituting these values in equation 2.14, the activity of the source at the time of the calibration can be computed,

$$A_1 \equiv A(t_{\text{span}}) = A_0 e^{-\ln 2(t_{\text{span}}/t_{1/2})} = 6.428(101) \times 10^4 \text{ decays/s.} \tag{2.15}$$

Because of the relatively high count rate experienced by the detectors, the computers and electronic modules used to process and record the data exhibit a *dead time*. This could reduce the number of recorded event that would otherwise be detected, given the right circumstances. Every *event file*, from the data acquisition software used at the NSCL, is accompanied by its corresponding *scalers file* which can be used to extract information regarding the dead time. From the scalers file of the ^{152}Eu data it can be found that the time the computer was active was $t_{\text{raw}} = 4384$ s (*raw clock*), while the time it was recording the pulses was $t_{\text{live}} = 1399$ s (*live clock*). A simple correction for the dead time, such as multiplying the number of recorder γ rays by the ratio $t_{\text{raw}}/t_{\text{live}}$, is sufficient for the purposes of this study.

The number of γ rays emitted isotropically from a particular electromagnetic transition, $N_{\gamma,\text{emit}}$, can be estimated by integrating the activity of the source from $t = 0$ to $t = t_{\text{raw}}$, this is,

$$N_{\gamma,\text{emit}} = b_\gamma \int_0^{t_{\text{raw}}} A(t)dt \tag{2.16}$$

where b_γ is the branching ratio of the transition and $A(t) = A_1 \exp[-\ln 2(t/t_{1/2})]$ is the activity of the source when the data was taken as a function of time. Even though the integral above can be easily calculated it is worth noticing that, in our case, $A(t)$ is approximately constant because the half-life of the source is of the order of years and the time data was collected was close to 23 minutes. Thus,

$$N_{\gamma,\text{emit}} = b_\gamma A(0) t_{\text{raw}} \tag{2.17}$$

$$N_{\gamma,\text{emit}} = b_\gamma A_1 t_{\text{raw}} \tag{2.18}$$

$$N_{\gamma,\text{emit}} = b_\gamma \times 2.818(44) \times 10^8 \tag{2.19}$$

[2]Wolfram Alpha website: `http://www.wolframalpha.com`. Input: "days from 1978/5/1 to 2009/3/27".

Table 2.1: Number of γ rays detected in each SeGA ring (with no dead time correction) and absolute ring efficiency tabulated for the energy of γ rays emitted in the decay of ^{152}Eu.

E_γ [keV]	b_γ	$N_{\gamma,\mathrm{obs}}^{(90^\circ)}$	$\epsilon_{\mathrm{abs}}^{(90^\circ)}$	$N_{\gamma,\mathrm{obs}}^{(37^\circ)}$	$\epsilon_{\mathrm{abs}}^{(37^\circ)}$
121.78	0.2837(13)	1239092(1222)	0.04857(79)	889336(1175)	0.03486(57)
244.7	0.0753(4)	247122(603)	0.03649(61)	176570(629)	0.02608(44)
344.28	0.2657(11)	704385(882)	0.02948(48)	504782(870)	0.02113(34)
778.9	0.1297(6)	193981(486)	0.01663(27)	139844(477)	0.01199(34)
964.1	0.1463(6)	189811(467)	0.01443(24)	135328(423)	0.01029(17)
1112.07	0.1354(6)	161251(432)	0.01324(22)	116227(366)	0.00955(16)
1408.01	0.2085(9)	210156(466)	0.01121(18)	149243(392)	0.00796(13)

The error of this approximation is of the order $(t_{\mathrm{raw}}/t_{1/2})^2 = \left(\frac{4.384\times10^3\ \mathrm{s}}{4.266\times10^8\ \mathrm{s}}\right)^2 \approx 10^{-10}$ which is much smaller than the error in A_1, justifying the approximation. Therefore, from equation 2.19, the number of emitted γ rays by the ^{152}Eu source can be computed by substituting known values of the branching ratios.

The recommended E_γ values for the most intense γ rays emitted from the decay of ^{152}Eu are listed in Table 2.1 as well as their branching ratios, number of γ rays observed in each SeGA ring[3] before correcting for the dead time and the absolute ring efficiency. The E_γ measured in each ring differed by less than 1 keV from the recommended values shown in the first column and, for compactness, are not shown in the table. The number of γ rays detected at the given E_γ values, $N_{\gamma,\mathrm{obs}}$, is obtained by integrating the background-subtracted area of the corresponding peak in the γ-singles spectra. Raw values obtained directly from the spectra are reported in the table as $N_{\gamma,\mathrm{obs}}^{(90^\circ)}$ and $N_{\gamma,\mathrm{obs}}^{(37^\circ)}$ for the respective rings, however, in the calculation of the absolute efficiencies the dead time correction was taken into account.

As mentioned above, the absolute counting efficiency of the detectors depends on the energy of the observed γ ray, E_γ. From the absolute efficiency values in Table 2.1

[3]Recall from section 2.3.4 that the detectors in SeGA were arranged in two rings: 9 in the 90° ring and 6 in the 37° ring.

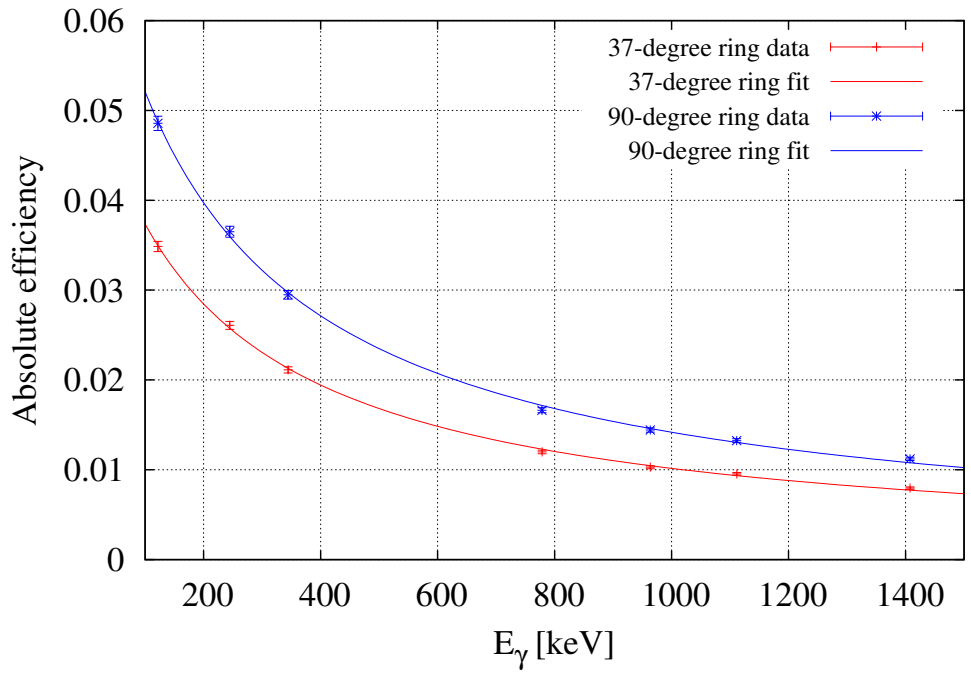

Figure 2.12: Absolute efficiencies of the detectors composing the SeGA rings measured from known decay radiation from ^{152}Eu. The solid lines represent the corresponding fits.

it is clear that ϵ_{abs} decreases with increasing E_γ. In practice, this behavior can be parametrized by the formula

$$\epsilon_{\text{abs}}(E_\gamma) = \frac{a}{(E_\gamma - c)^b}. \tag{2.20}$$

Measured efficiencies from the data of the ^{152}Eu γ source and their fits are shown in Figure 2.12. The parameters a, b and c in equation 2.20 were acquired by performing a least-square fit for the data of each ring of detectors. Their numerical values are $a = 7.32$, $b = 0.9287$, $c = -193.7$ for the 37-degree ring and $a = 10.57$, $b = 0.9332$, $c = -196.8$ for the 90-degree ring. The determined efficiency formulas would be enough to extract the values at the energies of the main peaks observed in the ^{44}S γ-singles spectrum if these nuclei where stationary in the laboratory reference frame. However, due to the high speeds at which the excited ^{44}S are travelling, relativistic effects must be considered to extract the *true* efficiency in the rest frame of these nuclei. The so-

Table 2.2: Boosted efficiencies, observed (measured) and emitted (calculated) number of γ rays in each SeGA ring tabulated for the energy of the observed γ rays in the deexcitation of ^{44}S.

E_γ [keV]	$\varepsilon_{\rm abs}^{(90^\circ)}$	$N_{\gamma,\rm obs}^{(90^\circ)}$	$N_{\gamma,\rm emit}^{(90^\circ)} \cdot 10^{-4}$	$\varepsilon_{\rm abs}^{(37^\circ)}$	$N_{\gamma,\rm obs}^{(37^\circ)}$	$N_{\gamma,\rm emit}^{(37^\circ)} \cdot 10^{-4}$
949	0.0135(2)	2000(77)	14.79(62)	0.0158(3)	2100(77)	13.31(66)
1128	0.0118(2)	1056(133)	8.92(113)	0.0137(2)	2165(133)	15.79(112)
1319	0.0104(2)	4461(83)	42.72(106)	0.0120(2)	3944(91)	32.82(93)
1891	0.0078(1)	512(49)	6.58(64)	0.0089(2)	307(51)	3.46(58)
1929	0.0077(1)	233(35)	3.03(46)	0.0088(1)	128(40)	1.46(46)
2150	0.0069(1)	200(32)	2.90(47)	0.0086(1)	182(35)	2.12(41)

called *boosted* efficiencies (here denoted by $\varepsilon_{\rm abs}$) are calculated from a GEANT3[30] simulation which models the boost of the in-flight γ rays. The simulation takes the functions of the observed efficiencies, then, assumes the source is moving at the same speed as the residual nuclei of interest (in this case ^{44}S with $v/c = 0.4211$) and performs a Lorentz boost (transformation) to the rest frame of the source.

The number of emitted γ rays can then be obtained from the number of observed γ rays by diving the latter number over the boosted efficiency for the γ-ray energy, this is,

$$N_{\gamma,\rm emit} = N_{\gamma,\rm obs}/\varepsilon_{\rm abs}. \tag{2.21}$$

The *boosted* efficiencies, $\varepsilon_{\rm abs}$, as well as $N_{\gamma,\rm emit}$, were calculated for the peaks in the γ-singles spectrum of ^{44}S for each ring assuming that all γ rays emerged with an isotropic distribution. Final values of the boosted efficiencies, number of observed γ rays and number of emitted γ rays are shown in Table 2.2 for the energy of the γ rays observed in the deexcitation of ^{44}S. Even though the present experiment was not designed to measure cross section, since the intensity of the incoming beam was not measured, the determination of the $N_{\gamma,\rm emit}$ values permits the evaluation of cross sections of the populated excited states in ^{44}S and their relative transition strengths.

2.4.4 Longitudinal Momentum Distributions

To determine the spin-parity (J^π) of the observed excited states of ^{44}S at excitation energy of 2268 and 2447 keV, longitudinal momentum distributions were extracted for ^{44}S residues in coincidence with the 949- and 1128-keV γ rays, respectively. In addition, a distribution was extracted for the direct population of the first excited state, at 1319 keV, by proportionally subtracting the two distributions mentioned above from the one acquired from ^{44}S in coincidence with the 1319-keV γ rays.

The longitudinal momentum of the residual nucleus is a projection onto the beam axis at the target position of the final (linear) momentum of the residual nucleus measured at the focal plane of the S800 spectrograph. In Figure 2.13, the observed momentum distributions are compared with the final forms of those calculated for states with different J^π values, which were corrected for the broadening induced by the experimental momentum distribution of the ^{46}Ar beam and by the differential energy losses of the beam and residue. The momentum distribution for the 1319-keV state is consistent with an assignment of 2^+, originally set by Glasmacher *et al.* [15]. The observed distribution in coincidence with the 949-keV γ ray is also best reproduced by a 2^+ assignment for the 2268-keV state. However, the experimental distribution in coincidence with the 1128-keV γ ray indicates a 4^+ assignment for the 2447-keV state. The details for obtaining the theoretical momentum distributions are described below.

The reaction theory, first presented in Refs. [31, 32] and extended in [33, 34], demonstrates that the reaction dynamics restrict direct two-nucleon removal events to grazing collisions. The model used for calculating the longitudinal momentum distributions assumes sudden, direct two-proton removal reactions and combines eikonal dynamics and shell-model wavefunctions. In this way, the collision samples the joint position and momentum configurations of the two removed nucleons[35]. The shell-model calculations provide the two-proton amplitudes connecting the ground state of the parent nucleus (in our case ^{46}Ar) with the final states of the daughter nucleus (^{44}S). In general, the wider the longitudinal momentum distribution, the higher the

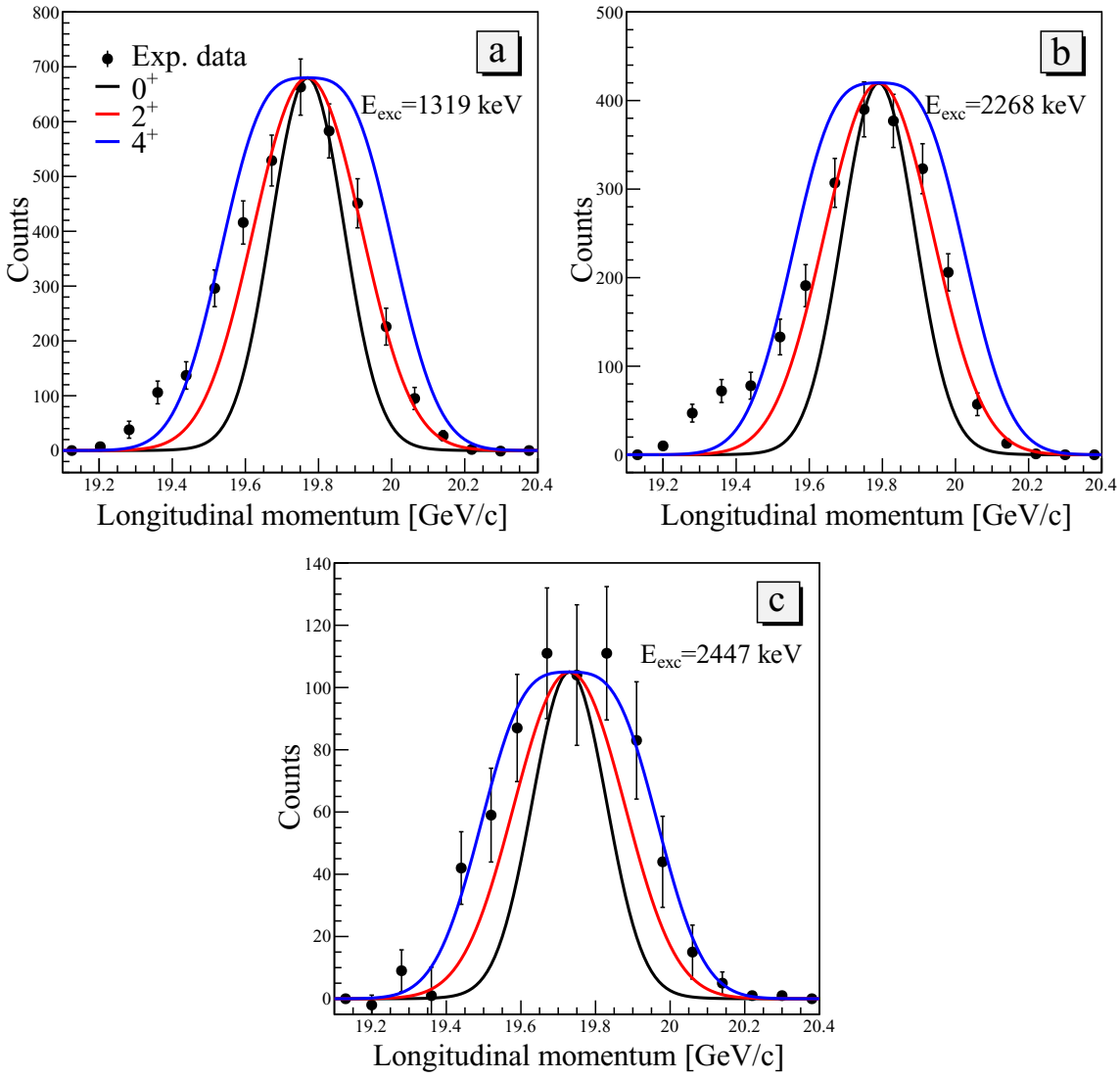

Figure 2.13: Observed and final form of the calculated longitudinal momentum distributions for the direct population of the 1319-keV state (a), the 2268-keV state (b) and the 2447-keV state (c). The experimental data is compared to the distributions calculated from the two-proton knockout mechanism for different final state spin hypotheses (see text).

J of the populated final state in the residual nucleus.

Longitudinal momentum distributions were calculated using shell-model wavefunctions from the SDPF-U interaction[36], which was deduced from a fit to data on the Z =8-20 and N= 20-40 region, and the reaction theory mentioned above. Figure 2.14 (a) shows the theoretical momentum distributions in colored solid lines for final states with spin-parity 0^+ (black), 2^+ (red) and 4^+ (blue) in the ^{44}S residual nucleus. It was assumed that beam particles of ^{46}Ar travelling with 99.9 MeV/A experienced two-proton knockout reactions (the conditions of the present experiment). Figure 2.14 (b) shows the longitudinal momentum profile obtained from unreacted beam data (statistical error bars are included but not visible in this scale). The solid gray line represents a Gaussian fit of the form $A_0 \exp[(p - p_0)^2/(2\sigma^2)]$, with amplitude $A_0 = 3.02 \times 10^5$, centroid $p_0 = 20.365$ GeV/c and standard deviation $\sigma = 0.0403$ GeV/c, or equivalently FWHM of 0.095 GeV/c. The last quantity provides a measurement of the momentum resolution found in the present experiment. To determine experimentally the longitudinal momentum, a precise map of the geometry of the S800 spectrograph as well as the settings of its magnets was necessary to reconstruct this quantity, given the final energy and momentum measurements at the end of the spectrograph. Said map and values were provided by NSCL scientists.

As indicated by Simpson and Tostevin [35], the theoretical momentum distributions need to account for the momentum profile of the unreacted beam, in order for them to show a more realistic shape, given the experimental conditions. This can be achieved by the convolution

$$F_1(p) = \int_{-\infty}^{\infty} f(p')g(p - p')dp'. \tag{2.22}$$

Here, $f(p)$ is a theoretical momentum distribution, $g(p)$ is the Gaussian fit to the experimental momentum profile and $F_1(p)$ the resulting convoluted momentum distribution. In general, $F_1(p)$ is broader and flatter than the original $f(p)$, nonetheless, this effect was not so strong in the current experiment because of the relatively narrow width of the beam momentum profile.

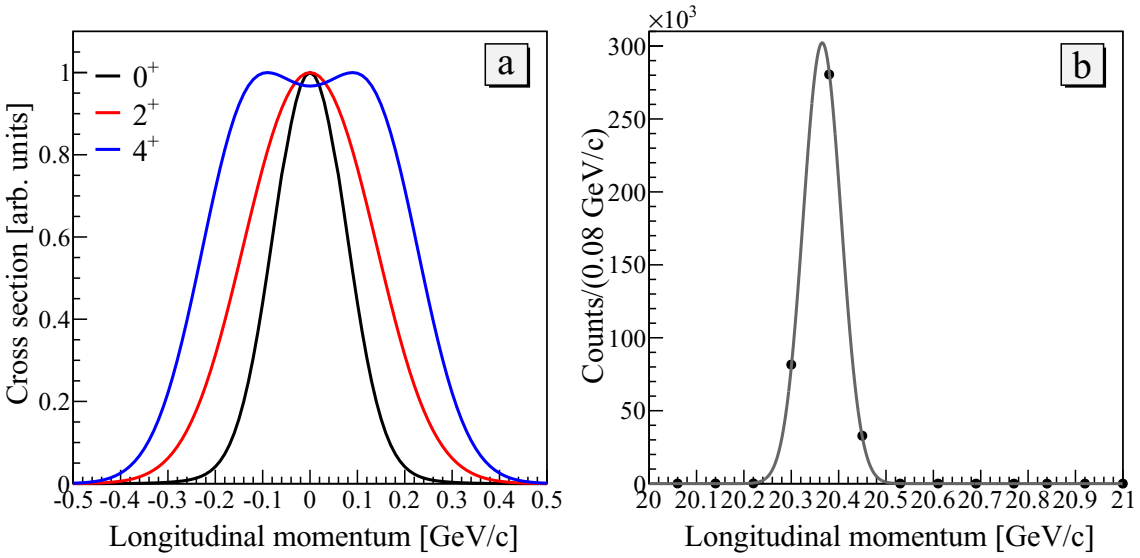

Figure 2.14: (a) Longitudinal momentum distributions calculated for different final J^π states of the residual nucleus ^{44}S assuming a two-proton removal from ^{46}Ar at 99.9 MeV/A. (b) Longitudinal momentum profile measured for the ^{46}Ar unreacted beam.

A second convolution is required to account for the differential energy losses of the beam and residual nucleus, due to the unknown location of the reaction vertex. The differential energy losses can be translated into a momentum width given by the difference of the maximum and minimum values of the momentum of the residue once it leaves the target. Since the energy loss of an ion travelling through the target depends on the ion's charge, Z, and is proportional to Z^2, the ^{46}Ar beam particles loose more energy in the target than the ^{44}S residues. Therefore, the maximum final momentum of the residue, $p^{\rm max}_{^{44}S}$, is reached when the two-proton knockout reaction occurs at the beginning of the target. The final momentum of the residue decreases until it reaches the minimum value, $p^{\rm min}_{^{44}S}$, when the reaction takes place at the end of the target. In our experiment, the ^{46}Ar beam had a kinetic energy of 99.9 MeV/A, or equivalently $v/c = 0.4295$, and the thickness of the ^{8}Be target was 188 mg/cm^2. Using the program LISE++[37] and the experimental values mentioned above, the calculated magnitudes of the maximum and minimum final momenta of the residual ^{44}S are $p^{\rm max}_{^{44}S} = 18.797$ GeV/c and $p^{\rm min}_{^{44}S} = 18.645$ GeV/c. Thus, the momentum width

due to the differential energy losses is

$$\delta p = p_{^{44}S}^{\max} - p_{^{44}S}^{\min} = 0.152 \text{ GeV}/c. \tag{2.23}$$

The final form of the theoretical momentum distribution, shown in Figure 2.13, is obtained by the convolution

$$F_2(p) = \int_{-\infty}^{\infty} F_1(p')s(p-p')dp', \tag{2.24}$$

where $s(q)$ is equal to 1 if $|q| \leq \delta p/2$ and 0 otherwise, and $F_1(p)$ is given by equation 2.22.

2.4.5 Cross Sections

As mentioned before, the present experiment was not capable to measure absolute cross sections since the beam intensity was not monitored while taking data from the two-proton knockout reaction. The scintillators available could not tolerate the count rate of the beam used in this experiment. On the other hand, the evaluation of the detection efficiency of SeGA (in section 2.4.3) enable the estimation of (relative) cross sections of the observed excited states. This can be done because the cross section, σ, of populating an excited state, labelled J_n^π, is proportional to the number of reactions yielding such state, $N_{J_n^\pi}$, upon the beam intensity, I_{beam}. Thus,

$$\sigma(J_n^\pi) = k\frac{N_{J_n^\pi}}{I_{\text{beam}}}, \tag{2.25}$$

where k is a positive constant. This can also be called the *exclusive* cross section. The value of $N_{J_n^\pi}$ can be computed from the number of detected γ rays, $N_\gamma(J_n^\pi)$, from the deexcitation of the state corrected for the detection efficiency. Transitions from higher excited states may be indirectly populating the state under consideration. If that is the case, $N_\gamma(J_n^\pi)$ must be decreased by the number of γ rays emitted from all other states deexcitating to the specified state. The remaining unknown factors in equation 2.25 can be eliminated if the so-called *inclusive* cross section has been

measured. In this case, the inclusive cross section is related to the probability of producing a residual ^{44}S. This is,

$$\sigma_{\text{inc}} = \sum_i \sigma(i) = \frac{k}{I_{\text{beam}}} \sum_i N_i, \tag{2.26}$$

where i represents any state in ^{44}S, whether ground state or excited state. From the ratio of 2.25 upon 2.26 and solving for $\sigma(J_n^\pi)$, the exclusive cross section can be expressed as a fraction of the inclusive cross section,

$$\sigma(J_n^\pi) = \sigma_{\text{inc}} \frac{N_{J_n^\pi}}{\sum_i N_i}. \tag{2.27}$$

The case of the first excited state ($J_n^\pi = 2_1^+$ and $E_{\text{exc}} = 1319$ keV) is taken as an example of the cross section calculation. From the findings presented in this study, it is known that three excited states in ^{44}S, with excitation energies of 2268(8), 2447(9) and 3248(12) keV, decay to the first excited state. The energy of the γ rays observed from the corresponding transitions are 949(5), 1128(6) and 1929(7), respectively. The number γ rays observed with the mentioned energies, $N_\gamma(E_\gamma)$, was computed by integrating the area of the matching (background subtracted) peak in the γ-singles spectrum. In addition, the *boosted* efficiency of the detectors must be taken into account in order to get the *true* number of emitted γ rays (see section 2.4.3). Then, the number of reactions directly populating the first excited state is

$$N_{2_1^+} = N_{\gamma,\text{emit}}(1319) - N_{\gamma,\text{emit}}(949) - N_{\gamma,\text{emit}}(1128) - N_{\gamma,\text{emit}}(1929). \tag{2.28}$$

From the values in Table 2.2 we get

$$N_{2_1^+} = 1.82(24) \times 10^5. \tag{2.29}$$

The number of ^{44}S residues produced in the two-proton knockout reaction can be extracted by integrating the regions in the particle identification plots (see Figure 2.8) where this nucleus is located. Technically, the reaction data was acquired from the combined *trigger*: SeGA single hits or S800 single hits downscaled by a factor of

500. Once the downscale factor is considered in the events that did not present a γ ray, the value

$$N_{^{44}\mathrm{S}} \equiv \sum_i N_i = 2.68(27) \times 10^6 \tag{2.30}$$

can be retrieved. From a similar experiment by Fridmann *et al.* [38] it is known that the inclusive cross section for producing ^{44}S via two-proton knockout reaction from a 98.6-MeV/A ^{46}Ar beam is 0.23(2) mb. Because of the nearly identical conditions between the two experiments it can be assumed that the same cross section value is encountered in the present experiment. Therefore, the exclusive cross section for directly populating the first excited state in ^{44}S is obtained after substitution of the values from 2.29, 2.30 and $\sigma_{\mathrm{inc}} = 0.23(2)$ mb in equation 2.27,

$$\sigma(2_1^+) = 0.016(3) \text{ mb}. \tag{2.31}$$

The same steps can be followed to compute the exclusive cross sections of the rest of the observed excited states.

The results are presented in Table 2.3, which lists the individual experimental and calculated cross sections for the observed states (details on the theoretical cross sections are given in section 2.5.1). The ground state and the excited 0^+ states are calculated to carry more than 50% of the total cross section. Among the excited states populated in our experiment, the 2_3^+ and 4_1^+ carry the largest individual cross sections, larger than the 2_1^+, which, in agreement with the calculation, is populated mostly indirectly. The tentatively identified 2150 keV (2_2^+) state is only weakly populated, while the reaction model predicts a strong population. It is interesting to note that the calculation predict an unobserved 4_2^+ state with a cross section of less than 1 μb. This is discussed in more detail in section 2.5.2. The inclusive cross section of the two-proton knockout reaction is 0.23(2) mb[38], while the reaction model calculates 0.87 mb. These observed cross sections are smaller than those calculated with the shell model and reaction model. However, it has been noted [32] that theoretical cross sections systematically overestimate experimental cross sections by a factor of 2 and the present results do not deviate significantly from this tendency.

Table 2.3: Deduced excitation energies of ^{44}S, $E_{\rm exc}$, with their spin and parity, J^π, measured deexcitation energy, E_γ placed towards the final level. Tentative placements are marked with an asterisk (*). Experimental and theoretical cross sections for populating the levels are also listed.

$E_{\rm exc}$ [keV]	J^π_n	E_γ [keV]	$J^\pi_{\rm final}$	σ [mb]	$\sigma_{\rm theo}$ [mb]
0	0^+_1				0.334
1319(7)	2^+_1	1319(7)	0^+_1	0.016(3)	0.028
1357(15)	0^+_2				0.163
2150(11)*	(2^+_2)	2150(11)	0^{+*}_1	0.004(1)	0.076
2268(8)	2^+_3	949(5)	2^+_1	0.024(3)	0.082
2447(9)	4^+_1	1128(6)	2^+_1	0.021(3)	0.032
3248(12)	(2^+_4)	1891(10)	0^{+*}_2	0.012(2)	0.033
		1929(7)	2^+_1		

2.5 Theoretical Calculations

2.5.1 Excited States and Cross Section

The shell-model states were calculated using the SDPF-U interaction[36], which was recently deduced from a fit to data on Z = 8-20 nuclei ranging from near-proton dripline to near-neutron dripline systems, and the Continuum Shell Model code[39, 40] for the diagonalization of the many-body Hamiltonian. The effective charges $e_n = 0.5$ and $e_p = 1.5$ were used for neutrons and protons, respectively. In the calculations, motion of the 8 protons and 8 neutrons most deeply bound was suppressed, effectively creating a ^{16}O core. The next 8 interacting protons were confined to the orbitals in the *sd* shell ($0d_{5/2}$, $1s_{1/2}$ and $0d_{3/2}$). Out of the next 20 neutrons, 12 were constrained as well to the orbitals in the *sd* shell and the remaining 8 neutrons were free to interact in the $0f_{7/2}$, $1p_{3/2}$, $0f_{5/2}$ and $1p_{1/2}$ orbitals. A depiction of the proton and neutron orbital can be seen in Figure 2.1.

The reaction theory, presented in Ref. [35], was utilized to calculate theoretical

cross sections for two-proton knockout from ^{46}Ar with 99.9 MeV/A kinetic energy, populating excited states in ^{44}S with $E_{\text{exc}} < 3.8$ MeV. The inclusive cross section was calculated at 0.87 mb.

A list of the calculated energy levels with their corresponding energy of excitation, E_{exc}, spin-parity, J^{π}, and cross section for directly populating the state via two-proton knockout is presented in Table 2.4.

Table 2.4: Calculated energy levels for eigenstates of the ^{44}S many-body Hamiltonian. The theoretical cross section is for the direct population of the J_n^{π} state via two-proton knockout ($2pKO$) from ^{46}Ar with 99.9 MeV/A.

E_{level} [keV]	E_{exc} [keV]	J_n^{π}	$\sigma_{\text{theo}}(2pKO)$ [mb]
-262.335	0	0_1^+	0.334
-261.197	1.139	0_2^+	0.163
-261.163	1.172	2_1^+	0.028
-260.194	2.141	2_2^+	0.076
-259.878	2.457	2_3^+	0.082
-259.767	2.569	4_1^+	0.032
-259.729	2.607	3_1^+	0.002
-259.603	2.733	4_2^+	0.000
-259.043	3.292	0_3^+	0.010
-259.014	3.321	2_4^+	0.045
-258.976	3.359	1_1^+	0.002
-258.871	3.464	3_2^+	0.020
-258.628	3.707	2_5^+	0.033

2.5.2 Particle-Hole Projections

Let a calculated Slater determinant from the solution of the many-body Hamiltonian of ^{44}S following a shell-model approach be denoted by $|i\rangle$. Each of the Slater determinants can be expanded as a linear superposition of orthonormal "configuration states", $|c_n\rangle$, representing possible combinations of neutrons occupying the $0f_{7/2}$

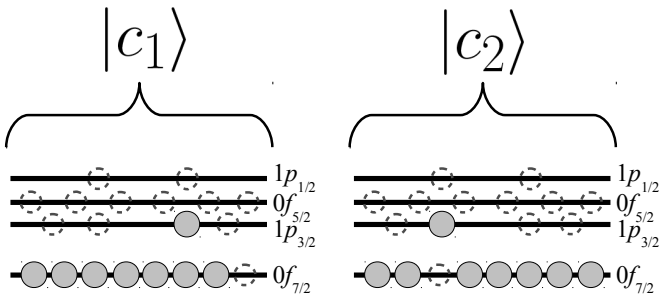

Figure 2.15: Example neutron configuration states in the {1p-1h} set.

shell and the pf shell (composed by the $1p_{3/2}$, $0f_{5/2}$, $1p_{1/2}$ orbitals). This is,

$$|i\rangle = \sum_n \alpha_{i,n}|c_n\rangle, \tag{2.32}$$

where the coefficients $\alpha_{i,n}$ are such that $\sum_n |\alpha_{i,n}|^2 = 1$ and the summation is over all possible neutron configurations. The set of configuration states in which n neutrons are in the orbitals $1p_{3/2}$, $0f_{5/2}$ or $1p_{1/2}$ is here denoted by {np-nh} and is called the "n-particle n-hole" set. In ^{44}S, there are 8 neutrons that can occupy the shells mentioned above. As an example, a particular neutron configuration where one neutron in the $0f_{7/2}$ orbital (with projection 7/2) has been promoted to the $1p_{3/2}$ orbital (with projection 1/2) can be represented by the state $|c_1\rangle$. Promotion of a neutron with a different projection leads to another state, $|c_2\rangle$, with equivalent {1p-1h} neutron configuration. This is pictorially described in Figure 2.15.

The probability of finding the state $|i\rangle$ in a particular neutron configuration can be calculated from sum of the square modulus of the projection of $|i\rangle$ onto each state in the set {np-nh}. This is,

$$P_n = \sum_{m\,\in\{n\text{p-}n\text{h}\}} |\langle i|c_m\rangle|^2 = \sum_{m\,\in\{n\text{p-}n\text{h}\}} |\alpha_{i,m}|^2 \,. \tag{2.33}$$

Results from the calculations of the probabilities of different states in ^{44}S to be in a {0p-0h} (gray), {1p-1h} (red), {2p-2h} (blue) or any other neutron configuration (green) are shown as a bar chart in Figure 2.16. In general, the contributions from

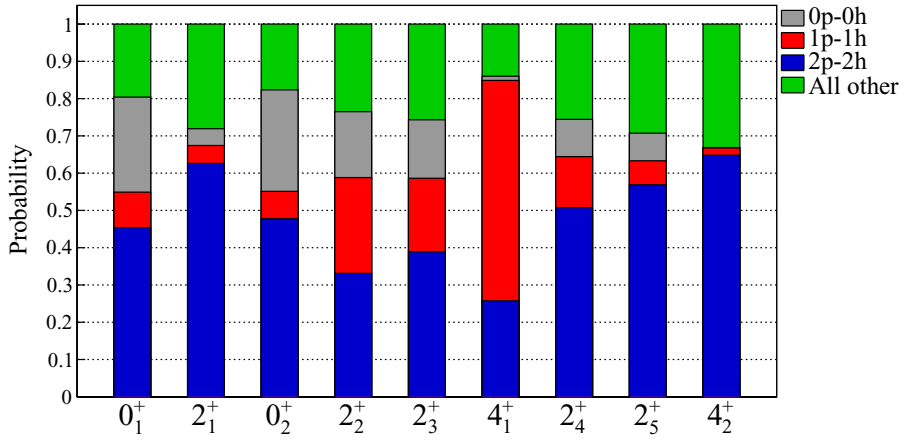

Figure 2.16: Probability of finding excited states in ^{44}S in different neutron configurations.

"all other" configurations are less than 30% in the wavefunctions of the states shown. The ground state, 0_1^+, and the isomeric 0_2^+ present similar configuration probabilities pointing towards strong mixing between these states. This agrees with the results by Force *et al.* [18] on these two states. Almost all of the calculated 2^+ states show mixed configurations except the first excited state, 2_1^+, which is mostly dominated by the {2p-2h} configuration. The other state dominated by such neutron configuration is the unobserved 4_2^+ state. In the conditions of the present experiment, the 2_1^+ was predicted to be populated with cross section of $\sigma(2_1^+) = 0.028$ mb, while the 4_2^+ state with $\sigma(4_2^+) \lesssim 1$ μb. However, calculations for the transition $4_2^+ \rightarrow 2_1^+$ showed a $B(E2) = 170$ e^2fm^4 and branching ratio of 99.9%. In the same calculation the transition $2_1^+ \rightarrow 0_1^+$ is reported with $B(E2) = 109$ e^2fm^4 and the experimental value is 63(18) e^2fm^4. These results suggest that, in analogy to the rotational spectra in heavier nuclei, the states 0_1^+, 2_1^+ and 4_2^+ could be members of a rotational band in ^{44}S, all connected by relatively strong $E2$ transitions. Experiments where the 4_2^+ state in ^{44}S is populated are necessary to corroborate this hypothesis.

The most notable configuration in Figure 2.16 is the one of the 4_1^+. The probability of finding this state in the {1p-1h} neutron configuration overshadows the ones of the other configurations. The transition $4_1^+ \rightarrow 2_1^+$ was one of the most in-

tense ones observed in the γ-singles spectrum, yet the calculations of P_n show that the wavefunction of the 2_1^+ state is dominated by {2p-2h} and in the case of the 4_1^+ by {1p-1h}. This suggests that the transition could in fact be hindered and as a consequence the 4_1^+ state would exhibit a relatively long half-life. This supposition agrees with the calculated half-life of the mentioned state, $t_{1/2} = 102$ ps. For comparison, half-lives calculated for all other observed states are of the order of 1 ps. More evidence supporting this hypothesis is presented in the next section.

2.5.3 Simulation of Line Shapes

At the NSCL a program based on GEANT3 was developed to simulate the response of the detectors in SeGA to γ rays emitted in flight. It accounts for the geometry of the detectors, interaction of radiation with matter, the half-life of the γ transition, as well as relativistic kinematics to generate the so-called simulated γ-ray *line shapes*, denoted here by $I_\gamma(E_\gamma)$. Examples of these line shapes can be seen in Figure 2.17. The main features of such line shapes are the full-energy peak of the mono-energetic γ ray (whose energy enters as a parameter in the simulation) and the Compton background, arising from consecutive Compton scatterings and photoelectric absorption of the incident γ ray. The γ-ray energy at which the Compton background is most intense is known as the *Compton edge*, $E_{C.E.}$. It corresponds to the maximum energy transferred to an electron through a single Compton scattering and is given by (see Chapter 10 in Ref. [41])

$$E_{C.E.} = \frac{E_\gamma}{1 + 2E_\gamma/m_e c^2}, \tag{2.34}$$

where $m_e = 0.511$ MeV/c^2 is the mass of the electron and E_γ the energy of the incident γ ray.

The intensities of the simulated line shapes shown in Figure 2.17 were only fit to the maximum hight of the corresponding peaks since the purpose of the figure is to display the main characteristics of the simulated line shapes. The total line shape, $I_{\rm tot}$, is actually a superposition of the individual line shapes and background. Furthermore,

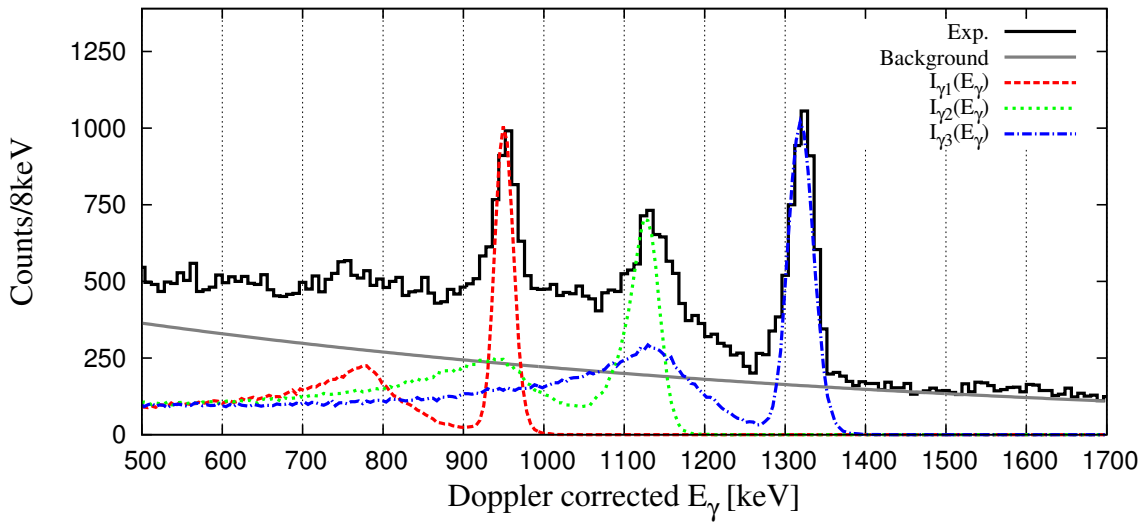

Figure 2.17: Simulated line shapes (I_γ) of the γ rays with energy centroids at 949, 1128 and 1319 keV in red (dashed), green (dotted) and blue (dot-dash) lines, respectively. Full response not yet fit to the observed γ-singles spectrum of ^{44}S (only from detectors in ring at 37°), in black. The solid gray line represents the exponentially decaying component of the background.

because of the relativistic Doppler effect line shapes simulated for detector in the 90° and 37° ring are different. Therefore, independent full responses of the form

$$I_{\rm tot}^{(\theta_r)}(E_\gamma) = B^{(\theta_r)}(E_\gamma) + a_1^{(\theta_r)} I_{\gamma 1}^{(\theta_r)}(E_\gamma) + a_2^{(\theta_r)} I_{\gamma 2}^{(\theta_r)}(E_\gamma) + a_3^{(\theta_r)} I_{\gamma 3}^{(\theta_r)}(E_\gamma) \qquad (2.35)$$

are fit to the experimental γ-singles spectra of each SeGA ring, hence the superscript (θ_r). In equation 2.35, the overall background function is of the form $B^{(\theta_r)}(E\gamma) = a_0^{(\theta_r)} \exp(-b_0^{(\theta_r)} E_\gamma)$ and $a_n^{(\theta_r)}$, with $n = 0, 1, 2, 3$, are positive constants. The background function parameters, $a_0^{(37^\circ)} = 600$, $a_0^{(90^\circ)} = 500$ and $b_0^{(37^\circ)} = b_0^{(90^\circ)} = 1/1000$, are selected to reproduce the data in the γ-singles spectra for $E_\gamma > 1350$ keV. From a reduced χ^2 numerical minimization[42] the coefficients of the $I_{\gamma n}^{(\theta_r)}$ are obtained. Explicitly, the quantity to minimize can be expressed as

$$\chi^2_{\rm reduced} \equiv \frac{\chi^2}{\nu} = \frac{1}{\nu} \sum_{p=1}^{p_N} \frac{(I_{\rm exp} - I_{\rm tot})^2}{I_{\rm tot}}, \qquad (2.36)$$

for all the points, p, such that $E_\gamma \in [500, 1500]$ keV. This quantity is computed and minimized for each ring but for simplicity the superindex in equation 2.36 has been

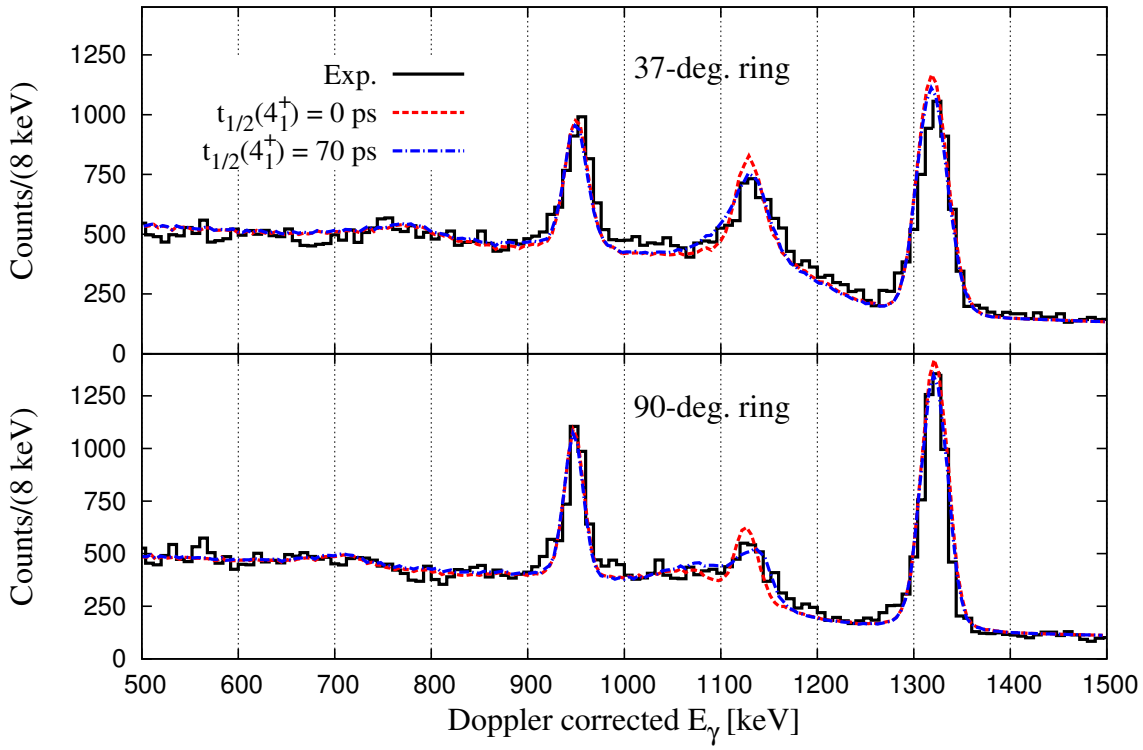

Figure 2.18: Total line shapes and experimental γ-singles spectrum for the 37° ring (top) and the 90° ring (bottom). The green (dotted) and blue (dot-dashed) lines corresponds to total line shapes where half-lives of the 4_1^+ state were set to 0 ps and 75 ps, respectively. All other γ transitions are assumed to be instantaneous.

dropped. The number of degrees of freedom, ν, is the total number of points minus the number of fit parameters (three in this case) minus 1, $\nu = p_N - 4$. The three parameters are the coefficients of the simulated line shapes, a_1, a_2 and a_3.

In the case of the simulated line shapes centered at 948 and 1319 keV, instantaneous ($t_{1/2}(J_n^\pi) = 0$ ps) γ transitions are assumed for the deexcitation of the corresponding states in ^{44}S, however, two line shapes are calculated for the 1128-keV peak for each ring: one with $t_{1/2}(4_1^+) = 0$ ps and another one with $t_{1/2}(4_1^+) = 75$ ps. The χ^2 minimization procedure is applied to the four sets of line shapes. The extracted total line shapes are shown in Figure 2.18 and the minimum reduced χ^2 values are shown in Table 2.5. The values are systematically smaller when the longer half-life is

assumed, independently of which ring is analyzed, but the differences between both cases are not large enough to be considered as strong evidence for a long-lived 4^+ state. Similarly, the total line shapes in Figure 2.18 are indeed suggestive of a broadened 1128-keV peak, consistent with emission with a half-life around 75 ps. However, proof of a delayed emission will have to come from a Recoil-Distance Method experiment. Such measurements will provide a strong confirmation of the deformed nature of the 4_1^+ state and of triple configuration coexistence in this nucleus.

Table 2.5: Reduced χ^2 values for the total line shapes of each SeGA ring, assuming two possible values of the half-life of the 4_1^+ state in ^{44}S.

Ring	$t_{1/2}(4_1^+) = 0$ ps	$t_{1/2}(4_1^+) = 75$ ps
37°	5.82	5.26
90°	9.03	8.40

2.6 Conclusions

Figure 2.11 compares the states observed in the present experiment with the predictions of the shell model calculation. The calculation predicts five excited states below 2.7 MeV in agreement with the current observations. The inclusive cross section under almost identical experimental conditions is 0.23(2) mb[38]. Using this value, cross sections for direct population of the 1319-, 2268- and 2447-keV states were estimated at 0.016(3), 0.024(3) and 0.021(3) mb, respectively. These measured cross sections are significantly smaller than those calculated with the shell model and reaction model outlined above (0.87, 0.028, 0.082 and 0.032 mb for the total, the 2_1^+, 2_3^+ and 4_1^+ states, respectively). However, theoretical cross sections systematically overestimate experimental cross sections by a factor of 2 [32] and the present results do not deviate significantly from this reduction.

The predictions of γ-ray intensities, represented by arrow widths in Fig. 2.11 (right), are derived from the calculated cross sections for the direct population of the

excited states and their corresponding γ-decay branches, where the effective charges $e_p = 1.5$ and $e_n = 0.5$ and the free-nucleon M1 operator were used. The calculation reproduces the pattern of strongly populated excited states, but overpredicts the population of the 2_2^+ state. It is interesting that the unobserved rotational 4^+ state is calculated to lie only 164 keV above the 4_1^+, and shows a theoretical population cross section smaller than 1 μb. Despite the proximity there is virtually no mixing between these states.

The role of the two-particle two-hole ({2p-2h}) neutron "intruder" configurations in inducing deformation in ^{44}S was first illustrated by Glasmacher *et al.* [15] who observed a large $B(E2 : 0^+_{\text{g.s.}} \rightarrow 2^+_1)$ value of 314(88) $e^2\text{fm}^4$, implying significant collectivity or permanent quadrupole deformation. The recent electron spectroscopy studies of Grévy *et al.* [16] and Force *et al.* [18] demonstrated that the ground state represents the prolate deformed intruder {2p-2h} neutron configuration and the excited 0^+ state at 1357 keV is a spherical state originating in the normal neutron configuration, {0p-0h}.

The shell-model calculation of this work gives a large laboratory frame electric quadrupole moment, 26 $e\,\text{fm}^2$, for the 4^+ state observed in the present experiment. However, this 4^+ state is not connected to the deformed ground state band by the strong $E2$ transitions that would be characteristic of in-band transitions. Instead, the calculation predicts that the 4^+ state is deexcited by a hindered $E2$ transition to the 2_1^+ so that it has a long half-life (about 75 ps). An examination of the wavefunction of this state reveals that the dominant neutron contribution is not the {2p-2h}, but instead is a {1p-1h} neutron excitation, $f_{7/2}^{-1}p_{3/2}$ (which accounts for $\sim 60\%$ of the wavefunction, according to the shell-model calculation). In fact, in a heavier rotational nucleus this 4^+ state would be called a "high-K" isomer because it appears to be the band head of a $K = 4$ band. By transforming the shell model result for the quadrupole moment of this state to an intrinsic frame (using a rotational model), it can be found that the intrinsic deformation is prolate with a magnitude of 51 $e\,\text{fm}^2$. While the ground state band has a prolate deformation as well (according to the

shell-model calculation), the microscopic origins of these prolate deformations are quite different. Thus, not three coexisting shapes, but three coexisting neutron configurations are found in ^{44}S, corresponding to zero, one and two neutron particle-hole excitations.

2.7 Summary

The configuration coexistence in ^{44}S is examined using the two-proton knockout reaction from a ^{46}Ar beam at intermediate energy. Four new excited states are observed. Two new spin assignments are made based on the longitudinal momentum distributions of the projectile residues. The observed states include a 4^+ state at 2447 keV. A shell-model calculation using the SDPF-U interaction suggests that this state has a strong prolate deformation in both the lab and intrinsic frames, but that its deformation is based on a one-particle one-hole neutron configuration which is different from the two-particle two-hole neutron intruder configuration responsible for the ground state deformation of this nucleus. These results were published in [43]. A Recoil Distance Method measurement of the lifetime of the 2447 keV 4^+ state could confirm its deformed nature and the presence of triple configuration coexistence within 2.4 MeV in ^{44}S.

CHAPTER 3

STUDY OF ^{20}O THROUGH THE $(\mathbf{d}, \mathbf{p})$ DIRECT REACTION WITH ANASEN

3.1 Motivation

In a given isotopic chain (nuclides with the same number of protons), the boundary between the last neutron-bound isotope and the first neutron-unbound isotope is known as the neutron *dripline*. This boundary also becomes evident when considering the lifetimes of neutron-rich nuclei. The shortest β-decay lifetimes are of the order of milliseconds while neutron emission lifetimes are generally much shorter than picoseconds[44]. A unified description of all nuclides, based on the underlying forces between neutrons and protons, should be able to reproduce the sequences of isotopes in the nuclear chart, from the limits of proton-rich nuclei to the neutron dripline[6].

The position of the neutron dripline for the oxygen isotopes ($Z = 8$), firmly established at ^{24}O by the experimental works of Fauerbach *et al.* [45] and Hoffman *et al.* [46], has attracted interest for a number of years because it does not follow the pattern set by nuclides with smaller or larger proton number. By adding one proton, from oxygen to fluorine, 6 more neutrons are bound, yet the observed neutron dripline continues with its the regular trend for larger Z. This can be seen in Figure 3.1, which also shows the year of discovery of the most neutron-rich nuclides for a given Z. From an experimental point of view, it is worth noting the enormous advances made over the last decade in the determination of the neutron dripline. However, this task becomes rapidly more difficult as scientist push the limits of the largest nuclear accelerators

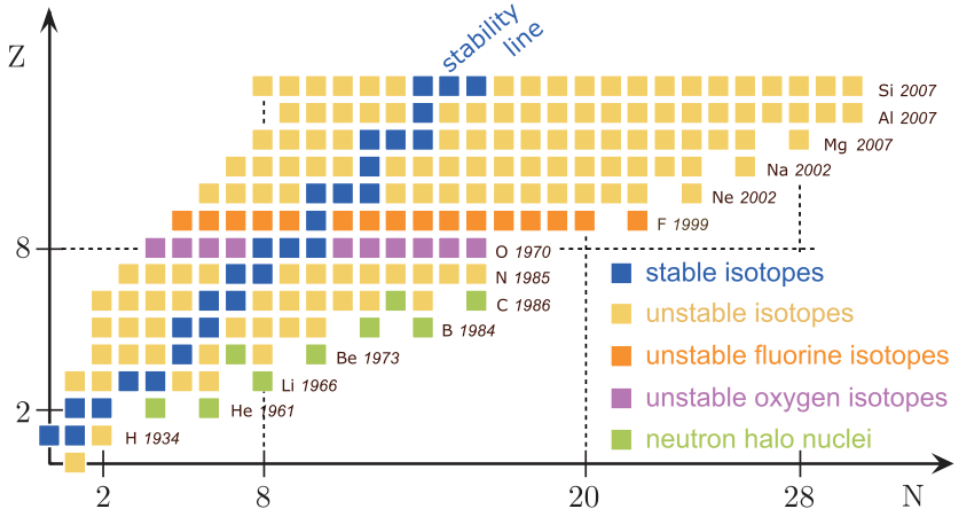

Figure 3.1: Chart of nuclides for $Z < 14$, highlighting the anomaly in the neutron dripline for the oxygen isotopes. Conventional magic numbers are shown on both axes. Image taken from [6].

to produce very neutron-rich nuclides with $Z > 14$.

In the framework of the shell model, the theoretical location of the neutron dripline for the oxygen isotopes depends on the single-particle energies (SPEs) of the orbitals in the neutron *sd* shell. Starting from ^{16}O, neutrons first fill the $0d_{5/2}$ orbital, with a closed subshell configuration at ^{22}O ($N = 14$), then the $1s_{1/2}$ orbital at ^{24}O ($N = 16$), and finally the $0d_{3/2}$ orbital at ^{28}O ($N = 20$). Addition of more neutrons would require placing them in higher orbitals, such as the $0f_{7/2}$. This is would be very energetically unfavorable, making such scenario unlikely. Thus, only neutron configurations in the *sd* orbitals are considered. In particular, the location of the neutron dripline exhibits a strong dependence on the SPEs of the $0d_{3/2}$ orbital. The role of the $0d_{5/2}$ and $1s_{1/2}$ orbitals is not as critical since they are predicted to have negative SPEs in the region of interest. This is illustrated in Figure 3.2, where calculations of the SPEs of the neutron *sd* orbitals are shown from $N = 8$ to $N = 20$. The SPEs vary drastically depending on the type of interaction used, yielding to different prediction for the last neutron-bound oxygen isotope. For example, in Figure 3.2 (a), calculations from pure

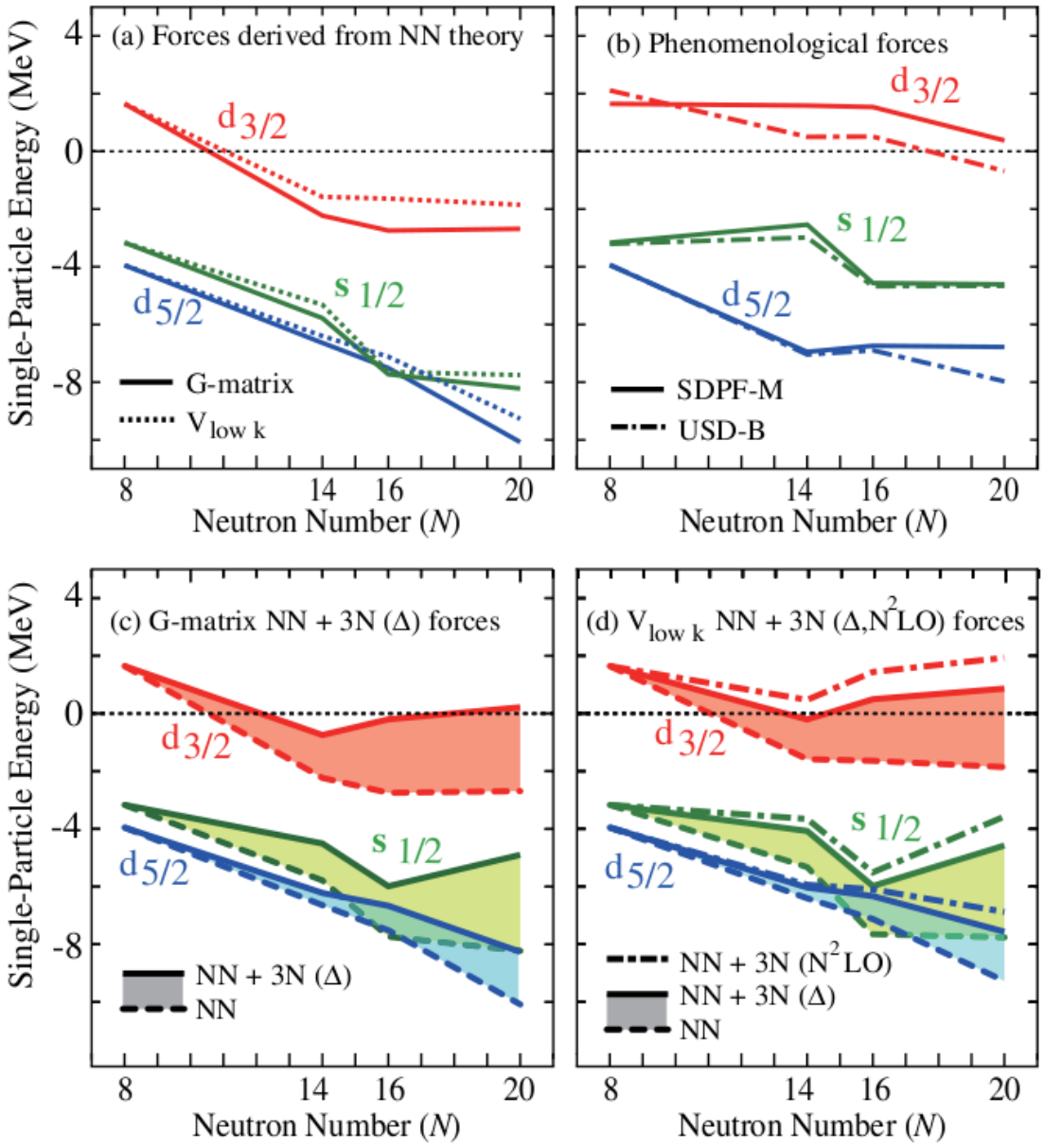

Figure 3.2: Single-particle energies of the neutron *sd* orbitals for isotopes of oxygen calculated using different interactions plotted as a function of neutron number N. Taken from [6].

nucleon-nucleon interactions give negative SPEs for the $0d_{3/2}$ orbital (red lines) for N between 16 and 20, implying that the last bound oxygen isotope is ^{28}O. Figure 3.2 (b) shows that, when using phenomenological forces (from interactions such as the SDPF-M) the $0d_{3/2}$ orbital is in general unbound (*i.e.* SPE > 0) but has a tendency of decreasing the SPEs as it approaches $N = 20$. Finally, Figure 3.2 (c) and (d) display results when three-body terms are included in the interactions and, in these two cases, the prediction of the neutron dripline, at or close to ^{24}O, is in better agreement with the experimental results in [45, 46].

To ascertain which one of the interactions presented in Figure 3.2 provides a better description of the nuclear force, measurements of the SPEs in the neutron-rich isotopes of oxygen are necessary. Empirically, it is possible to measure the SPEs with one-nucleon transfer reactions, such as (d, p)[1]. In this reaction, a neutron is stripped off the deuteron and transferred into the receiving nucleus, ^{A}Z (with atomic number Z and mass number A), while the proton proceeds without exciting the internal degrees of freedom of the receiving nucleus. Excited states of the resulting ^{A+1}Z nucleus (formed in the transfer reaction) can be populated if the center-of-mass energy of the $^{A}Z + d$ system is sufficiently large. From the energy and momentum of the outgoing protons the kinematics of the event can be reconstructed. Furthermore, the matrix elements corresponding to final single-particle states can be extracted from the cross sections of the reaction. Such matrix elements are a measurement of the purity of the single-particle states and are embodied in the so-called spectroscopic factor, C^2S[47]. The spectroscopic factor does not depend on the transition operator that takes $^{A}Z+n$ to ^{A+1}Z. Instead, it only depends on the overlap of their wave functions, and therefore can be calculated rather reliably for many nuclei[48]. A relatively large spectroscopic factor ($C^2S \sim 1$), corresponds to a pure single-particle neutron wave function coupled to the receiving nucleus. Thus, experiments employing the (d, p) reaction on oxygen isotopes provide the means to trace the evolution of the SPEs as a function of the neutron number.

3.2 Single-Particle States in ^{20}O

In 2010, I participated in an experiment, led by C. R. Hoffman, to study the neutron-rich ^{20}O via the ^{19}O(d,p) reaction in inverse kinematics. The experiment was performed at Argonne National Laboratory where a radioactive ^{19}O beam produced by the Argonne Tandem-LINAC Accelerator System (ATLAS) In-Flight Facility[49]. The primary beam was $^{18}O^{5+}$ with a kinetic energy of 8.06 MeV/A. A cryogenically cooled gas cell held the deuterium gas target from which the radioactive beam originated through the ^{2}H(^{19}O,^{19}O)^{1}H reaction. The energy of the ^{19}O beam was 6.61(3) MeV/A and its typical purity approximately 50%, with the remaining intensity coming from ^{18}O particles of the primary beam. The radioactive beam was transported into the Helical Orbit Spectrograph (HELIOS)[50, 51], where solid deuterated polyethylene (CD_2) target of thickness 260 μg/cm^2 was placed. Back-scattering protons, emerging from the reactions of the beam with the CD_2 target, were analyzed with an array of position-sensitive Silicon detectors and the heavy recoils were measured downstream in a telescope of Silicon detectors. Events from proton-^{20}O coincidences generated the excitation energy spectrum of ^{20}O, shown in Figure 3.3. A total of 8 peaks were identified below 6 MeV. Known levels at 0.00, 1.67, 3.57, and 4.07 MeV were used to calibrate the excitation energy which had a resolution of approximately 175 keV FWHM. Where possible, orbital angular momentum assignments and spectroscopic factors were deduced through comparison of theoretical cross sections, obtained from distorted wave Born approximation (DWBA) analysis of the measured cross sections. The results were publish in 2012 in Ref. [52].

The location and fragmentation of the neutron *sd* orbitals can be observed by comparing the extracted spectroscopic factors to theoretical calculations. In Figure 3.4, the deduced spectroscopic factors (black circles) along with calculations from the USD-A and USD-B[53] shell-model interactions (green and blue circles, respectively) are shown. The experimental points are extracted from Hoffman *et al.* [52] and the calculations are performed using the Continuum Shell Model code[39, 40]. Each

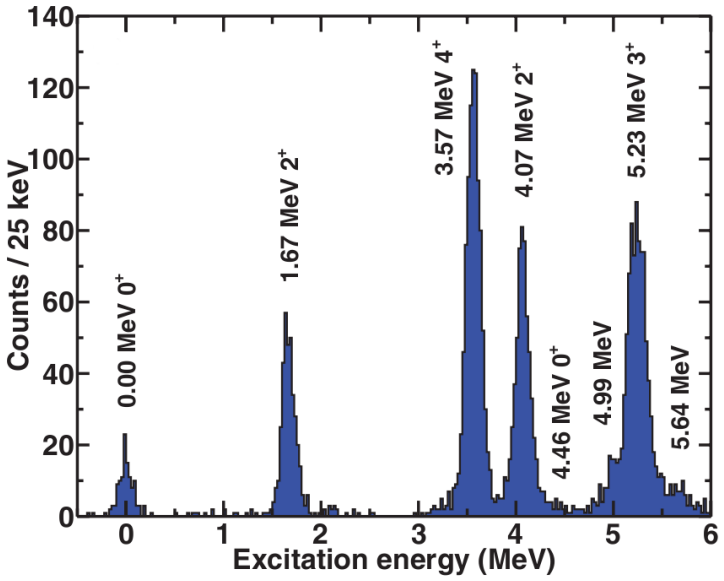

Figure 3.3: Excitation energy spectrum of ^{20}O states populated via the ^{19}O(d,p) reaction in inverse kinematics. Taken from [52].

graph in the figure contains the spectroscopic factors, C^2S, of overlaps of the ground state of ^{19}O plus a single neutron in a specific *sd* orbital and final states in ^{20}O with total angular momentum, J, and positive parity. The C^2S are plotted against the excitation energy of the final state. From left to right the panels show the overlaps with the neutron *sd* orbitals, $d_{5/2}$, $s_{1/2}$ and $d_{3/2}$, and from top to bottom excited states in ^{20}O with spin-parity $J^\pi = 0^+, 2^+, 4^+$. In general, the calculations and the extracted spectroscopic factors show that most of the single-particle strength for $E_{\text{exc}} < 6$ MeV is distributed in the $d_{5/2}$ and $s_{1/2}$ orbitals. The calculations predict that $d_{5/2}$ orbitals are fragmented upon excited states with $E_{\text{exc}} > 6$ MeV. Such highly excited states were not observed in the experiment by Hoffman *et al.* [52], since the energy of the back-scattering protons, emerging from the ^{19}O$(d,p)^{20}$O reaction and leaving the ^{20}O in such states, approaches zero as the scattering angle increases, thus preventing them from being detected with the utilized experimental methods.

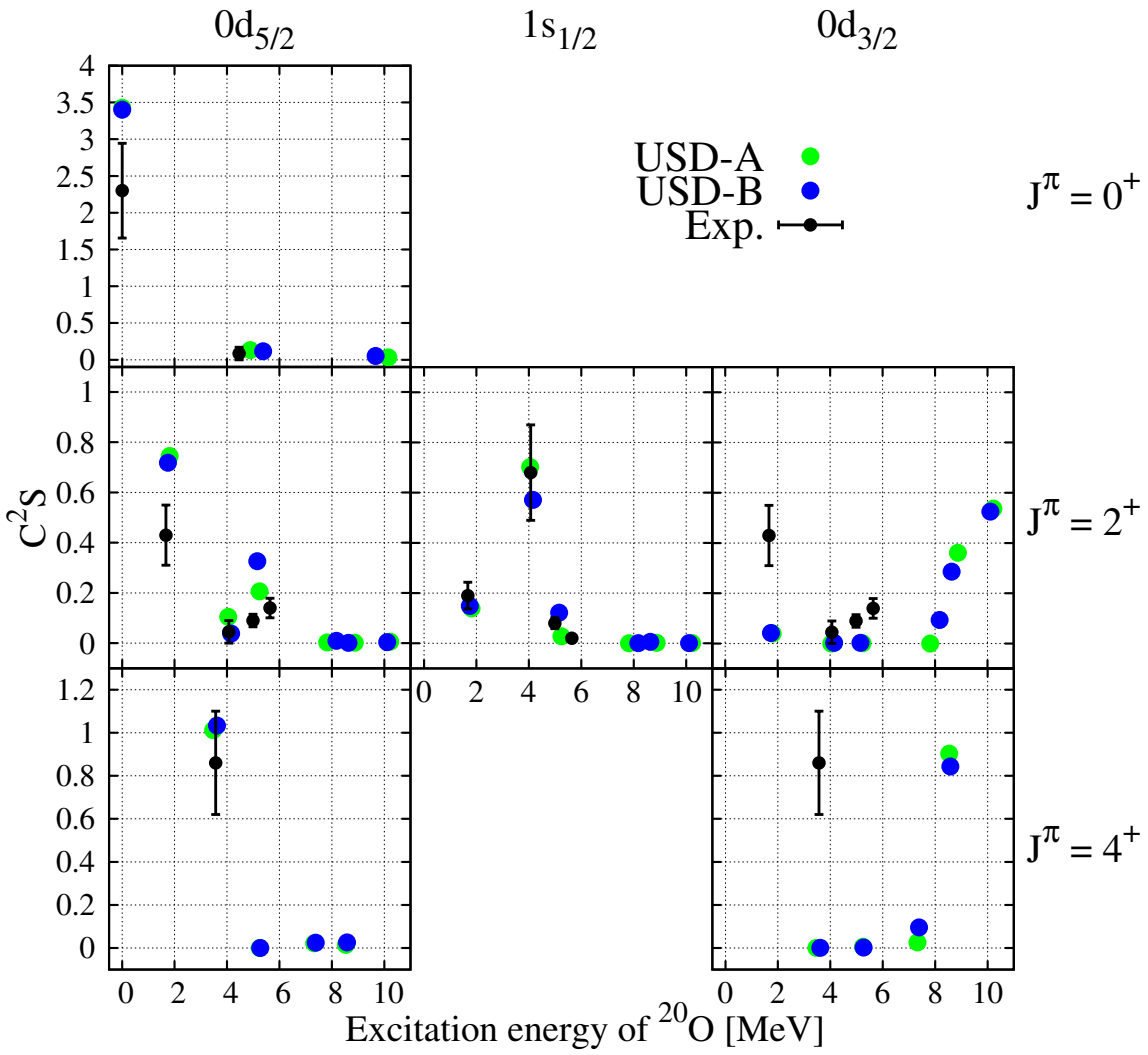

Figure 3.4: Deduced (black) and calculated (green and blue, from USD-A and USD-B interactions, respectively) spectroscopic factors of the overlap of final states in ^{20}O and single-neutron addition to the ground state wavefunction of ^{19}O plotted against the energy of excitation of states in ^{20}O. The columns represent different single-particle orbitals of the transferred neutron, while the rows represent different total angular momentum quantum numbers of the states in ^{20}O. The data of the overlaps of the $0d_{5/2}$ and $0d_{3/2}$ orbitals with the $J^\pi = 2^+, 4^+$ states are repeated, since the two $l = 2$ orbitals cannot be distinguished experimentally.

3.3 Experiment

In order to study the location and fragmentation of the $0d_{3/2}$ orbital in ^{20}O a beam of the short-lived ^{19}O was produced at the RESOLUT radioactive beam facility in the John D. Fox Superconducting Accelerator Laboratory, located on the main campus of the Florida State University. The Tandem Van de Graaff accelerator and the LINAC booster delivered a primary beam of ^{18}O with kinetic energy of 6.33 MeV/A to the deuterium gas (D_2) primary target. A radioactive ^{19}O beam with purity of 65% and kinetic energy of 5.11 MeV/A was selected from the reaction products by the recoil mass spectrometer RESOLUT. The radioactive beam intensity was 1×10^5 pps. A detailed explanation on the experimental equipment utilized to produce radioactive beams at the John D. Fox Superconducting Accelerator Laboratory is available in the dissertation by Rojas [54].

The radioactive beam was delivered to the chamber of active gas target/detector ANASEN, which was filled with D_2 gas. The ^{20}O was produced via the ^{19}O(d,p) reaction in inverse kinematics. It is worth noting that this experiment is pioneering in using pure D_2 gas as target and ionizing medium of the proportional counter in ANASEN. The beam energy range covered inside the chamber was from 2.21 to 4.24 MeV/A. The light recoils were measured with large solid angle coverage and were identified by the differences in their specific energy loss in the gas plotted against their final energy. Because ANASEN was still under development at the time the present experiment was realized, an attenuated stable beam of ^{17}O was sent into the detector before producing the radioactive beam. Data from the ^{17}O$(d,p)^{18}$O reaction was acquired to verify our experimental methods and analysis techniques. This reaction was selected because of its similarities with ^{19}O(d,p) and because of the available data from previous experiments[55]. For comparison, Table 3.1 shows a summary of important physical quantities for the mentioned oxygen isotopes. In the next section, an overview of ANASEN and its components is presented.

Table 3.1: Comparison of oxygen isotopes present in the experiments.

Isotope	Half-life [s]	Main decay mode	Ground state	1st exc. state	N
^{17}O	stable	—	$5/2^+$	$1/2^+$ at 0.87 MeV	9
^{18}O	stable	—	0^+	2^+ at 1.98 MeV	10
^{19}O	26.88	β^-	$5/2^+$	$3/2^+$ at 0.096 MeV	11
^{20}O	13.51	β^-	0^+	2^+ at 1.67 MeV	12

3.4 The Active Gas Target Detector: ANASEN

The Array for Nuclear Astrophysics and Structure of Exotic Nuclei (ANASEN) is a charged-particle detector array developed by Louisiana State University and the Florida State University. The array consists of 30 silicon-strip detectors backed with Caesium-Iodide (CsI) scintillators[1]. Although experiments can be performed simply by placing a solid target in the evacuated ANASEN chamber and directing a beam to it, a position-sensitive cylindrical gas proportional counter is also included in the detector array. This allows ANASEN to be used as an active gas target/detector, which was the selected mode of operation in the present experiment. In this mode, the beam enters the gas filled chamber through a Kapton window, which restrains the gas (at pressure ranging from 10 to 500 Torr) from escaping to the evacuated beam line (usually at 10^{-7} Torr). Then, the beam particles loose energy as they ionize the gas molecules on their path. If a beam particle interacts with a nucleus of a gas molecule a nuclear reaction may occur, thus emitting light particles, such as protons, neutron, alphas, etc. The location of the interaction along the z-axis is directly correlated with the energy loss of the beam particle. Therefore, reactions at multiple beam energies can be measured without changing the parameters of the accelerator.

An example of a reconstructed event of the reaction $^{17}\mathrm{O}(d,p)^{18}\mathrm{O}$ is displayed in Figure 3.5 (this is not just an illustration of the event but actual particle tracks calcu-

[1]This was the configuration at the time the present experiment was realized, nonetheless upgraded forward detectors were installed shortly afterwards.

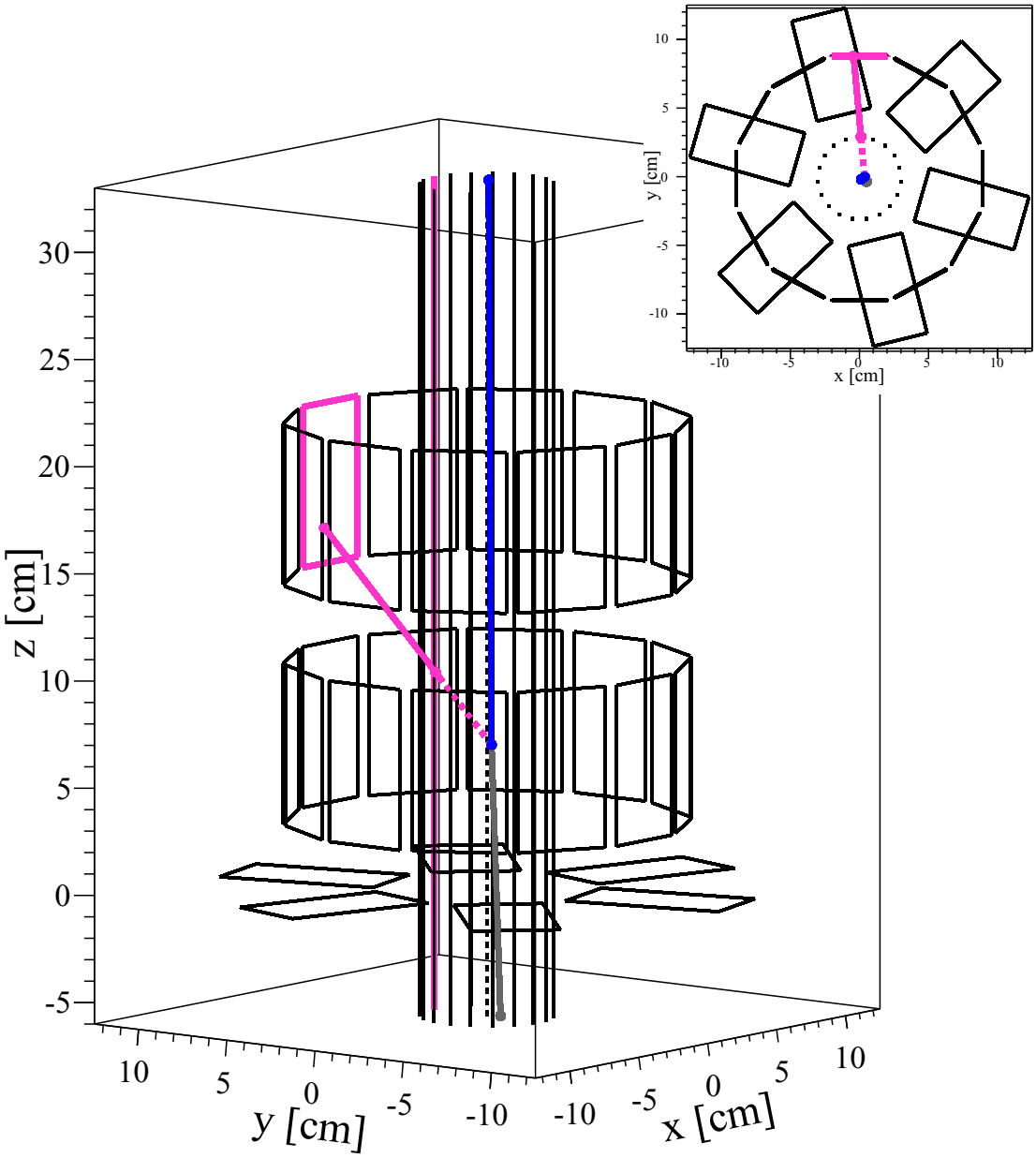

Figure 3.5: Particle tracks from a reconstructed event. The color coding is as follows: pink for the detected proton, blue for the beam particle, gray for the (undetected) heavy recoil. SX3 detectors and PC wires are outlined by solid black lines, except the ones from which the proton was observed (highlighted in pink). The inset show a downstream view of the event.

lated from real data). From the same figure, one can get a perspective of the detector geometry, since the active area of the silicon detectors is delineated by polygons and the proportional counter wires by black solid lines parallel to the z-axis and extending from -6 to 33 cm. The silicon detectors arranged in a cylinder around the z-axis are called *ring* detectors while the ones placed on the xy-plane at $z = 0$ are called *forward* detectors. In reality, the xz-plane is parallel to the floor of the laboratory , the y-axis points vertically up and the downstream direction points towards the $(-z)$-axis.

The silicon-strip detectors are manufactured by Micron Semiconductor[2] using the Super X3 (SX3) design, which was developed for ANASEN. A computer-aided design of the SX3 detector can be found in Figure 3.6. Each of the SX3 detectors has 4 ohmic back segments and 4 resistive front strips. Once the detectors are calibrated, the energy deposited by a charged particle is obtained from the back segment signals while the position of the particle hit along the main axis of the detector is given by the front strips. A total of 24 detectors were arranged in 2 cylinders around the z-axis and 6 of them were used as forward detectors.

The proportional counter (PC) is composed of 19 carbon fiber wires (resistance ~ 4 kΩ/cm and 7 μm in diameter) extended parallel to the z-axis. Each PC wire is tensioned by metal springs at both ends to prevent sagging. The PC wires require to be surrounded by a gas for the detection of charged particles. When travelling through the gas, protons, alphas, and other recoiling particles emerging from the reactions may ionize nearby gas molecules. The freed electrons from the ion pair formation are then attracted by the PC wires, which are set to a positive voltage. If the kinetic energy of one electron is larger than the ionization energy of the neutral gas molecule, it is possible to create an additional ion pair in a collision between both particles. Subsequent collisions free more electrons which are also accelerated to the wire, thereby generating an avalanche of electrons. This phenomenon is known as *gas multiplication* and is discussed in detail in Ref. [41]. The thin diameter of the anode wires allows high gain to be achieved at modest voltages, which is necessary for the

[2]Website: `http://www.micronsemiconductor.co.uk/index.asp`

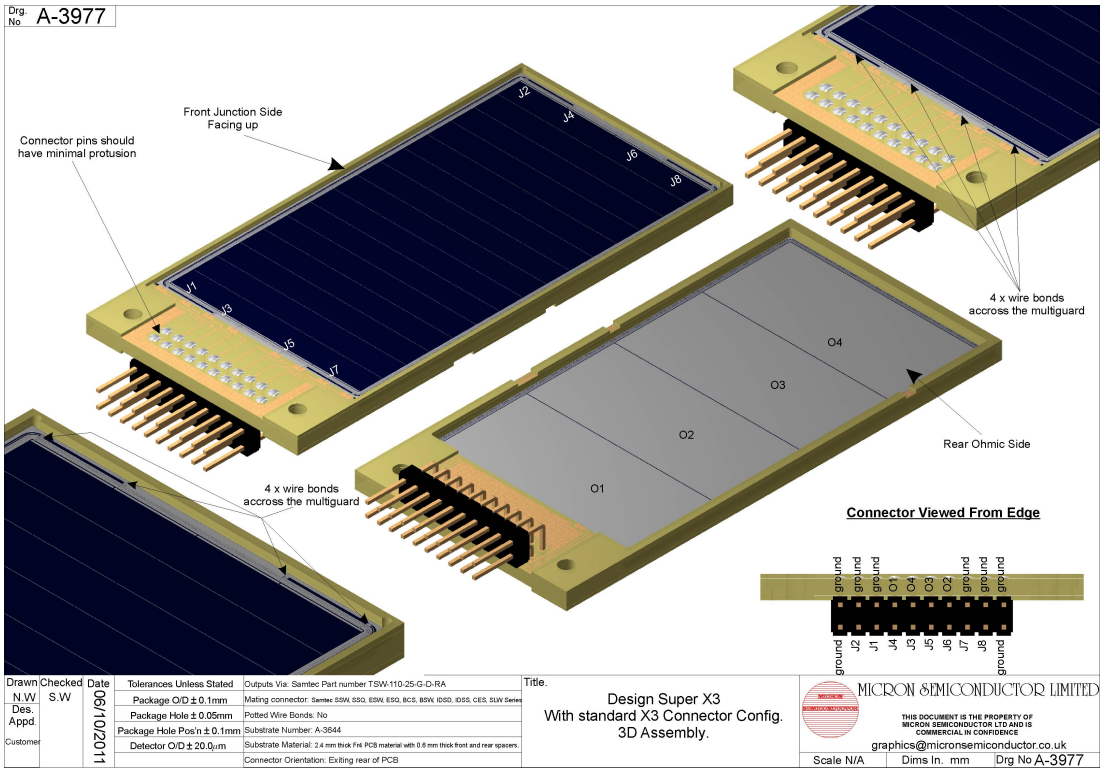

Figure 3.6: Design of the Super X3 detector.

observation of small signals from high energy protons at the gas pressures required for the operation as a "target" gas[56]. A cell, formed by 8 grounded cathode wires, shields every anode wire from the high ionization region near the beam axis and define a charge collection region with a cross sectional area of ~ 1 cm^2. Each of the cathode wires is made of gold-plated tungsten and with a diameter of 50 μm. In the process of ionization, the ions loose energy depending on the medium conditions, their velocity, charge and mass (this is discussed in more detail in section 3.6.2). The signals from the energy lost by the ions in the PC cells in combination with the final ion energy, measured by the SX3 detectors, provides the means for identifying different recoil particles.

ANASEN will be used primarily at the RESOLUT radioactive ion beam facility at the Florida State University and at the ReA3 reaccelerated beam facility at the National Superconducting Cyclotron Laboratory.

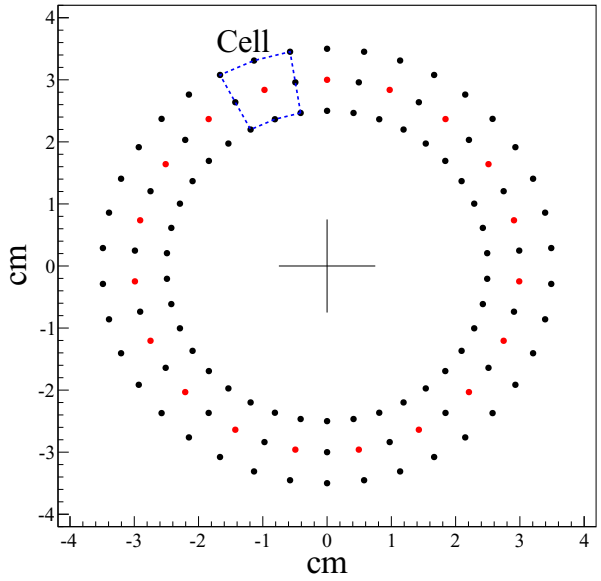

Figure 3.7: Beam view of proportional counter and grounding wires, in red and black respectively. The dashed-blue line represents the region covered by one cell.

3.5 SX3 and PC Calibration Procedures

Extensive computer codes were created to reduce the time employed in the calibration process of the (30) SX3 detectors and (19) PC wires in ANASEN. The codes were written using the object-oriented `C++` programming language where the so-called *classes* combine data structures and methods for data manipulation in a single scheme. Classes were created for each type of detector inheriting elements from a vast number of classes from the ROOT Data Analysis Framework[3]. In practice, the calibration steps are carried out by the use of computer *scripts*. The scripts used for the calibration of the ANASEN detectors in the present experiment can be found in Appendices C.2 and C.3. In the following subsection, each of the steps in the energy and position calibration procedures for the SX3 detectors as well as the steps in the position calibration of the PC wires are explained. It should be noted that all fits used to extract the calibrations parameters are linear. Second order fits were

[3]Website: `http://root.cern.ch`

attempted for the position calibration of both SX3s and PC wires but were unstable and resulted on larger errors than when using 1st order fits. Below, the calibration algorithms and nomenclature of the detectors are summarized.

The following conventions are made for the SX3 ring detectors, hence the assignment of a downstream and upstream sides of the detectors is natural. In the special case of the forward detectors the "downstream" ("upstream") side coincides with the farthest (closest) side to the z-axis. Each of the SX3 detectors has a total of 12 channels. Channels 0-3 correspond to the ohmic back segments, being channel 0 the closest to the pin connectors. Channels 4-11 are designated for the 4 resistive front strips, being channel 4-7 assigned to the downstream side and channels 8-11 to the upstream side. Once the calibration constants are obtained for a detector, the energy is obtained from the back segments and given in MeV, while the position is extracted from the front strips and given in cm. Table 3.2 shows the nomenclature and conventions related to the SX3 detectors that are used throughout the rest of this chapter.

The steps in the SX3 calibration procedure can be summarized as follows:

1. **Offset correction**: for every channel, determine the electronic offset from pulser data.

2. **Gain-matching back segments**: for every back segment, except the reference one, determine the relative coefficients that align the peaks from the ^{228}Th α source (placed in the evacuated chamber).

3. **Energy calibration of back segments**: using all back segments, determine the detector's linear energy coefficient and offset to match the energies of the α particles from the same data as in the previous step.

4. **Gain-matching front strips to back segments**: for every front strip and back segment combination, determine the parameters of the total front signal in order to match the calibrated back signal from *in-beam* data (few events are needed).

5. **Position calibration**: for every front strip, determine the position calibration coefficients from the border hits (usually from filtered *in-beam* data).

Table 3.2: Conventions for physical quantities (top) and channel subindices (bottom) of the SX3 detectors.

Symbol and relation	Description
q_{ch}	Raw signal
$Q_{ch} = q_{ch} - q_0^{(ch)}$	Electronic offset corrected signal
$Q_b^{\mathrm{cal}} = m_b Q_b$	Gain-matched back signal
$E_b = C_1 Q_b^{\mathrm{cal}} + C_0$	Calibrated energy from back channel (in MeV)
$Q_f^{\mathrm{cal}} = m_d Q_d + m_u Q_u + o_f$	Gain-matched front signal
$Q_d^{\mathrm{cal}} = m_d(Q_d + \frac{o_f}{m_d+m_u})$	Calibrated downstream signal
$Q_u^{\mathrm{cal}} = m_u(Q_u + \frac{o_f}{m_d+m_u})$	Calibrated upstream signal

Subindex	Name	Values
ch	channel number	0-11
b	back segment number	0-4
f	front strip number	0-4
d	downstream channel	4-7 (or $f+4$)
u	upstream channel	8-11 (or $f+8$)

Table 3.3: Conventions for physical quantities (top) and channel subindices (bottom) of the PC wires.

Symbol and relation	Description
q_{ch}	Raw signal
Q_{ch}	Calibrated response
$Q_t = Q_d + Q_u$	Total signal strength

Subindex	Name	Values
ch	channel number	0, 1
d	downstream channel	0
u	upstream channel	1

In the case of the PC, each wire has 2 electronics channels specified by the indices 0 and 1, which correspond to its downstream and upstream sides, respectively. Since it is difficult to find a calibration process for the typical energy range of the PC wires (0-100 keV), the voltage settings of the pulser module are used as the unit proportional to the energy loss in the wire cell. Once the calibration constants are obtained for a PC wire the total signal strength is given in V (volts), while the position is given in cm. Table 3.3 shows the nomenclature and conventions related to the PC wires that are used throughout the rest of this chapter. The steps in the PC wire calibration algorithm can be summarized as follows:

1. **Signal intensity calibration**: for every channel, determine the response of the electronics to the pulsed signals at different voltages.

2. **Position calibration**: determine the position calibration coefficients from the expected hit position of α particles emitted by sources (normally two *needle* sources of ^{210}Po are used).

3.5.1 Channel Maps

The starting point of the data analysis and calibration programs is the creation of the channel maps. A channel map is a text file with the correspondence between Application Specific Integrated Circuit (ASIC) motherboard, chip number and channel number (or the ADC/TDC module number and channel number) to the unique detector type, identification number and channel number. Example of the ASIC and CAEN (ADC/TDC) channel maps are presented in Appendix B. Once the channel maps have been created they are loaded to the data processing programs, where they are used to sort the raw data in every hit to the corresponding detector.

3.5.2 SX3: Offset Correction

To find the electronics offsets, pulsed signals at different voltages are directly supplied to the preamplifiers. The recorded the data yield comb-like spectra for the raw signals, as the one shown in Figure 3.8 (left). For the SX3 detectors, only a linear

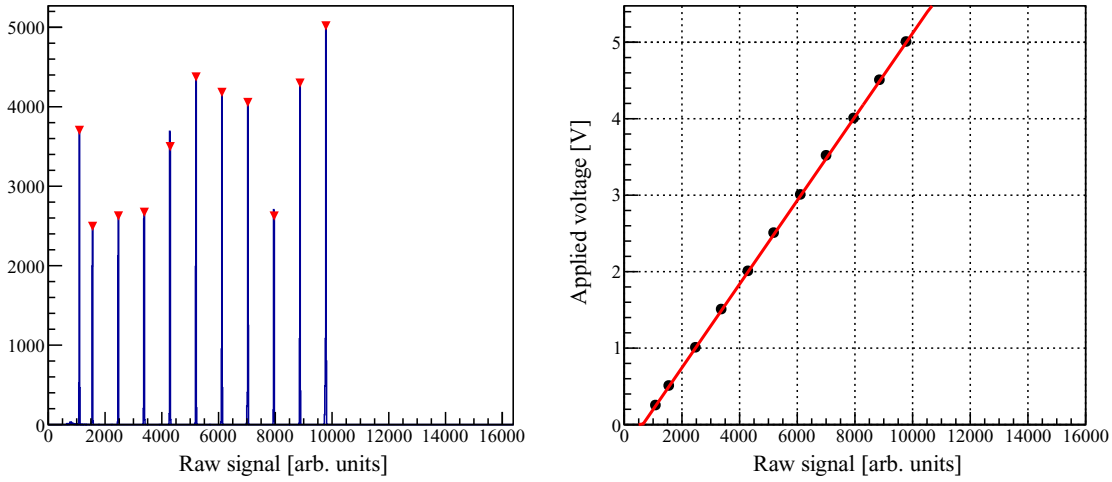

Figure 3.8: Left: Example of pulser data. The red symbols on the top of each peak indicate the the position of the peak has been automatically found. Right: Voltage as a function of the measured signal. The red line represents the linear fit.

behavior, $V = A_1 q + A_0$, was observed. Here, V is the voltage and q is the measured signal. Figure 3.8 (right) shows the linear fit of the positions of the peaks in the spectrum to the values of the provided voltages, from which the $A_{0,1}$ coefficients are extracted. In practice, only the signal offset $q_0 = -A_0/A_1$ is saved as a calibration constant for each channel in the detector. This constant is later subtracted from the raw signals of the corresponding channel when sorting data in an event-by-event basis.

3.5.3 SX3: Gain-Matching Back Segments

As a prerequisite for the energy calibration, in this step, all the back segments are gain-matched using data from the ^{228}Th α source. A reference channel is selected and its coefficient (gain), m_b, is set to 1. It is common to select the channel with the most counts to reduce statistical uncertainties when finding the centroids of the peaks. Then, the other channels are gain-matched by fitting the position of their peak centroids to the ones of the reference channel (this is basically a linear fit with no offset). This determines the gain-matching constants, m_b.

3.5.4 SX3: Energy Calibration of Back Segments

In this step, the data from the ^{228}Th α source needs to be resorted applying the gain-matching coefficients. A spectrum with the measured gain-matched back signals of all the back channels is obtained. Then, the positions of the centroids of the α peaks in this spectrum are plotted against the kinetic energy of the alpha particles emitted by the source. These points are then fit with an order-1 polynomial,

$$E_\alpha = C_1 Q_b^{\text{cal}} + C_0, \tag{3.1}$$

thus acquiring the absolute energy calibration constants, $C_{1,0}$. Figure 3.9 (left) shows a one dimensional spectrum of the Q_b^{cal} signals from all the back channels. The absence of multiple peaks emerging for each mono-energetic α particle demonstrates the quality of the gain-matching coefficients obtained for each back channel. In Figure 3.9 (right), the black points are the (emission) energies of selected α particles in the decay chain of ^{228}Th plotted against the centroid of the observed peaks (in the left panel). The red solid line is obtained from a linear fit of the data. In general, the energy resolution of the SX3 detectors is $\sim$ 50 keV (taken from the FWHM of the Gaussian fits to the peaks of mono-energetic α particles).

When calibrating a detector, one should use the α emission energy which is slightly lower than the α transition energy because it accounts for some energy transmitted to the parent nucleus as recoil energy. Table 3.4 lists the α emission energies in the ^{228}Th decay chain (top) and in the α decay in ^{210}Po (bottom). These values can be found in Refs. [57, 58, 59]. In practice, only 6 of the 8 α-emission energies are considered in the fits. The first two emission energies in the ^{228}Th decay chain, at 5.340 and 5.423, generate a single (slightly broader) peak which, accounting for the differences in the decay probabilities, has a maximum at 5.41 MeV. Similarly, the energies at 6.051 and 6.090 MeV are combined in a single peak with maximum at 6.06 MeV.

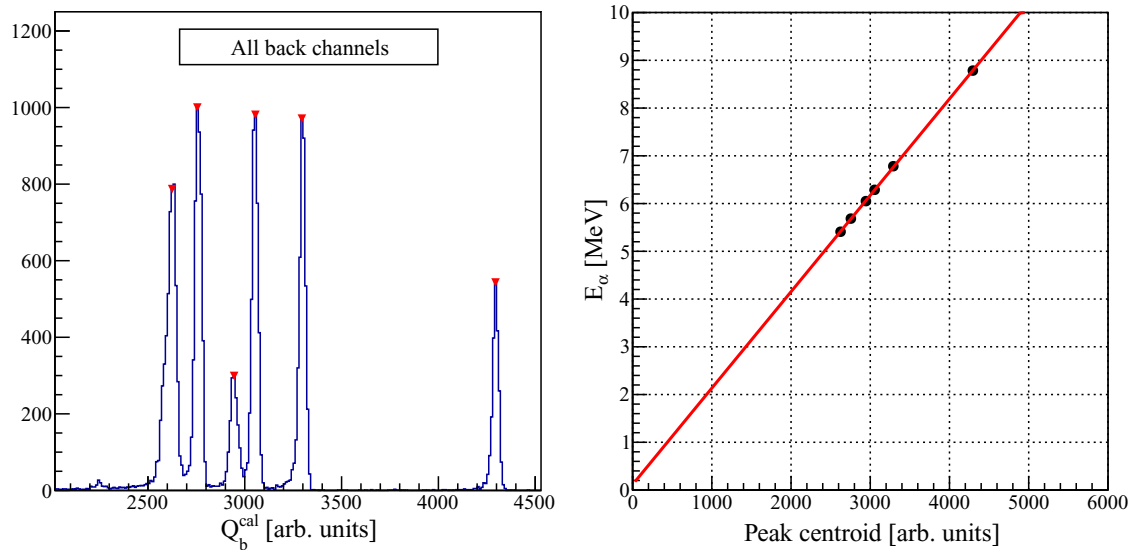

Figure 3.9: Left: Data of ^{228}Th α source after finding all gain-matching constants and electronics offsets. Right: Energy of α particle as a function of the peak centroid. The red line represents the linear fit.

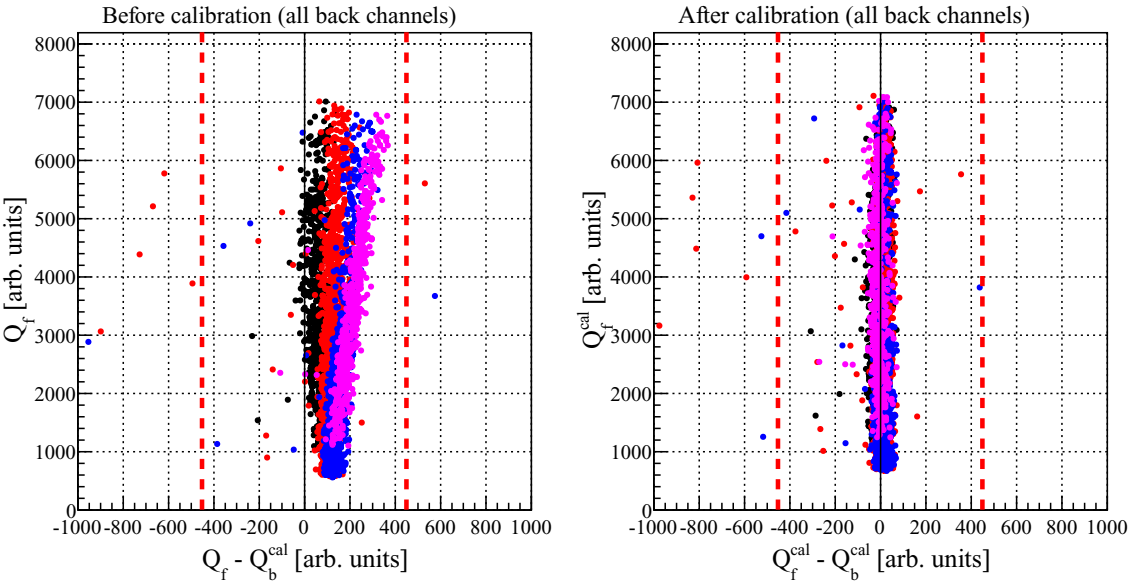

Figure 3.10: Left: Uncalibrated total front signal from one front strip plotted against the difference between the front signal and the gain-matched back signal. Data points in black, red, blue and pink are from back channels 0, 1, 2 and 3, respectively. Right: Same data points after gain-matching the front strip to the back segments, showing the equivalence between Q_f^{cal} and Q_b^{cal}. Dashed red vertical lines define the fitting region.

Table 3.4: Energy of α particles emitted in the ^{228}Th decay chain (top) and the ^{210}Po source (bottom). All decays end in the ground state unless denoted by *.

228-Thorium α-decay chain		
Decay	E_α [MeV]	Decay mode probability [%]
^{228}Th$\rightarrow$ ^{224}Ra*	5.340	26
^{228}Th$\rightarrow$ ^{224}Ra	5.423	73
^{224}Ra$\rightarrow$ ^{220}Rn	5.685	94
^{212}Bi$\rightarrow$ ^{208}Tl*	6.051	25
^{212}Bi$\rightarrow$ ^{208}Tl	6.090	10
^{220}Rn$\rightarrow$ ^{216}Po	6.288	99
^{216}Po$\rightarrow$ ^{212}Pb	6.778	99
^{212}Po$\rightarrow$ ^{208}Pb	8.785	100

210-Po α decay		
Decay	E_α [MeV]	Decay mode probability [%]
^{210}Po$\rightarrow$ ^{206}Pb	5.304	99

3.5.5 SX3: Gain-Matching Front Strips to Back Segments

Before determining the position calibration, one first needs to find a set of coefficients for the calibrated front signal to match the calibrated back signal for any real event. This step is necessary because the position calibration procedure described below uses the so-called *border hits*, which are particle hits at the border between two neighboring back segments spreading the energy of the hit and therefore the total signal strength. Reconstruction of the total signal strength by simple addition of the two calibrated back signals has proven to be unreliable. A more complicated reconstruction would most likely involve more calibration coefficients. Therefore, for this type of hits it is simpler to measure the "hit energy" from the front signals.

Assuming the values of the constants m_b and $q_0^{(d,u,b)}$ have already been extracted, only parameters related to the front strip need to be determined in order to complete the gain-matching of the total front signal to the back signal. From the convention in Table 3.2, the equality between the back and front signals can be written as

$$Q_b^{\rm cal} = m_u Q_u + m_d Q_d + o_f. \tag{3.2}$$

To extract the parameters $m_{u,d}$ and o_f, a two-dimensional fit is used where only events presenting one back and two front signals from the same front strip are considered. The effect of these parameters can be observed in Figure 3.10, where data for one strip is shown before (left) and after (right) this calibration step. On the left panel, the uncalibrated total front signal from the front strip is plotted against the difference between the front signal and the gain-matched back signal. Data for individual back channels are superimposed. The points in black, red, blue and pink correspond to back channels 0, 1, 2 and 3, respectively. On the right panel, the same data points are shown after using the gain-matching constants for front strip obtained in the fit. This demonstrates the equivalence between $Q_f^{\rm cal}$ and $Q_b^{\rm cal}$ in a large range of signals. After the values of the three front-strip parameters have been established, the calibrated upstream and downstream signals, given by

$$Q_d^{\rm cal} = m_d \left(Q_d + \frac{o_f}{m_d + m_u} \right) \tag{3.3}$$

$$Q_u^{\rm cal} = m_u \left(Q_u + \frac{o_f}{m_d + m_u} \right), \tag{3.4}$$

are ready to be used in the position calibration.

3.5.6 SX3: Position Calibration

The position at which a particle hits a front strip of the SX3 detector, p, can be found by a polynomial expansion of the ratio of the calibrated downstream or upstream signals upon the calibrated total signal (either from the back or the front sides). This is,

$$p_s = \sum_{n=0}^{N} C_{s,n} \left(\frac{Q_s^{\rm cal}}{Q_{\rm tot}} \right)^n \tag{3.5}$$

where $s = d, u$ and $Q_{\rm tot} = Q_b^{\rm cal} = Q_f^{\rm cal}$. In practice, the first order expansion yields excellent results. Besides, with the calibration method described below, fitting a higher order polynomial has proven to be unstable due to the small number of known positions. When both, downstream and upstream signals are observed, the final position is obtained with $p = (p_d + p_u)/2$, otherwise only one side is used to determine the position.

To calibrate the position to physical coordinates on the detector strip the so-called *border hits* are used. As mentioned above, these are particle hits that occur at the border between two back segments, triggering two back channels. These hits do not happen frequently, thus relatively large amounts of data need to be sorted to achieve reasonable statistics. The actual position of the border is known to a precision of 0.5 mm. Figure 3.11 illustrates how the position calibration coefficients are extracted by a linear fit of the expected hit position to the measured signal strength ratios, $Q_{d,u}^{\rm cal}/Q_{\rm tot}$. For energies greater than 2 MeV the SX3 detectors showed a position resolution in general better than 1.23 mm, which was extracted from the full width at half maximum of a Gaussian fit to the border hit calibrated data. From the actual size of the detector, the expected minimum and maximum position values along the main axis of the detector are 0 and 7.5 cm. The final, 3-dimensional hit position is a function of the p value, the front strip number and the SX3 detector identification number. The (x, y, z) hit coordinates are acquired after loading the so-called *world coordinates* file (see Appendix B.3) into the data processing programs, which places each SX3 detector in its corresponding geometrical position in ANASEN (see for example Figure 3.5).

One of the main advantages of this method for calibrating the position in the SX3 detectors is that it can be performed with the same events produced by the reactions between the beam and target. Furthermore it does not require the fabrication of hardware for its realization. An alternative calibration procedure was envisioned in which detector masks with thin cuts ($\sim$ 1 mm wide) made at specific locations are fabricated and later attached to the detectors. Then, the position of the particle hits

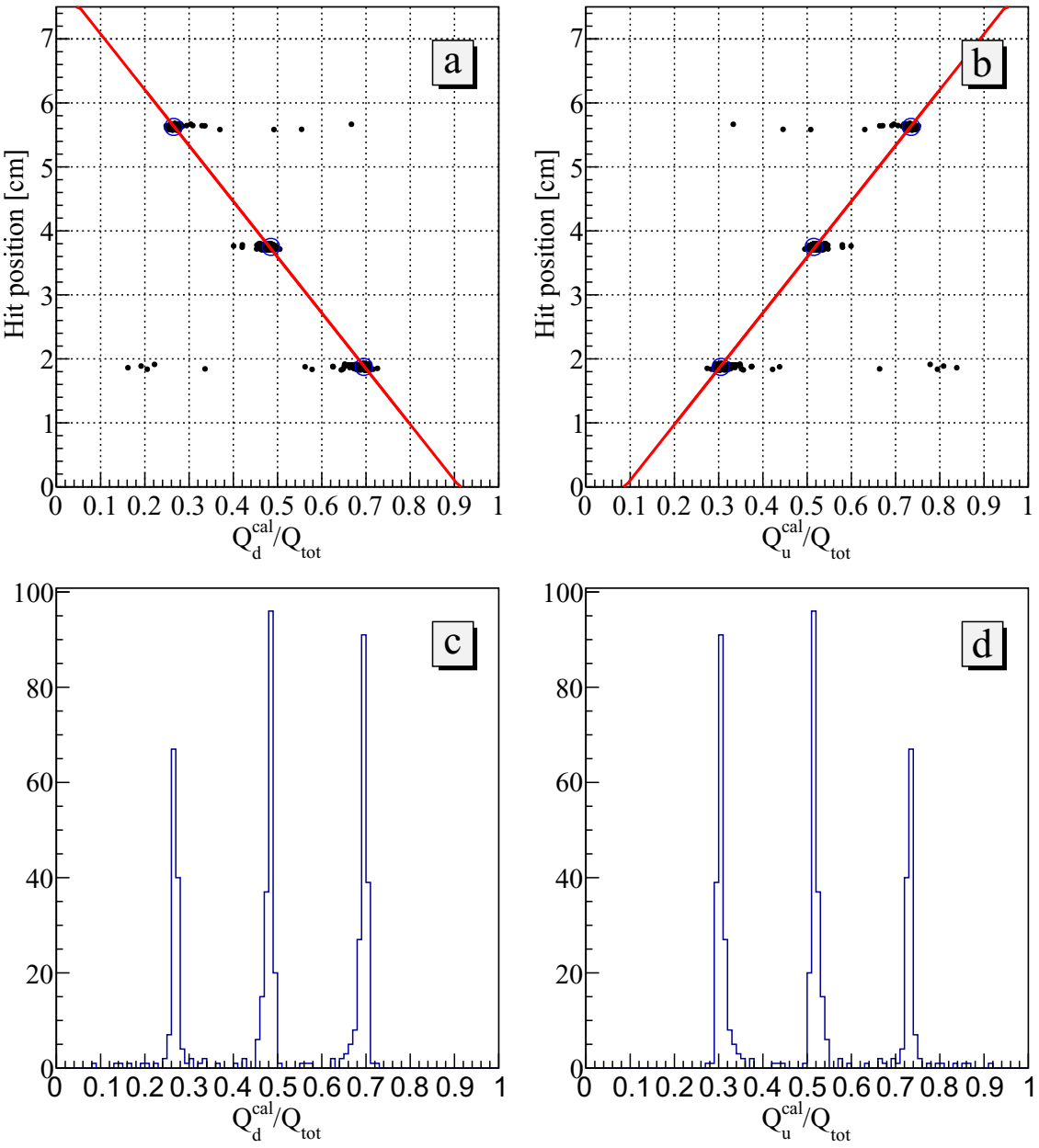

Figure 3.11: Border hits data used in the position calibration of an SX3 front strip. (a) and (b) show the expected hit position as a function of the signal strength fraction measured from the downstream and upstream sides, respectively. The blue circles in the top panels represent the position of the centroids of the peaks observed in the histogram of ratios of the downstream and upstream calibrated signal upon the total signal, in panel (c) and (d), respectively.

would be known since they would only be able to strike the detector through the cuts. In such case the second order coefficients, in equation 3.5, may be determined reliably, as more hit positions would be known. However, such process would be very labor-intensive and time-consuming, considering that 30 masks would need to be machined and that, every time position calibration data needs to be acquired, the chamber of ANASEN would need to be taken to atmospheric pressure and evacuated after the masks have been attached.

This is the last step in the calibration procedure of the SX3 detector. The calibration steps for the PC wires is presented in the remaining subsections.

3.5.7 PC: Signal Intensity Calibration

In order to calibrate the PC wires it is necessary to determine the response of the electronics modules used in the processing of the raw wire signals. The is because, the preamplifiers used for the PC wires have a linear response to small signals and a logarithmic one to larger signals. The objective in this step is to eliminate dependencies on the electronics used for each wire, however, this does not eliminate variations from the intrinsic differences to each wire (for example, their resistivity values). Pulsed signals at different voltages are sent to the preamplifiers and the observed raw signals are recorded to disk. As in the case of the SX3 detectors, a comb-like spectrum is obtained when the data from the pulser is sorted. In the simplest case, the signals and voltages will exhibit a linear relation,

$$V = A_1 q + A_0. \tag{3.6}$$

Then, the fitted parameters $A_{1,0}$ are saved[4]. In the case the pulsed signals reach the logarithmic range, the response is linearly interpolated from the known pulser calibration points. Let the centroid of the i-th pulser peak be q_i^{pc} for a given voltage V_i. Then, for a raw signal (q) between q_i^{pc} and q_{i+1}^{pc}, the voltage (V) is given by

$$V = \frac{V_{i+1} - V_i}{q_{i+1}^{pc} - q_i^{pc}} (q - q_i^{pc}) + V_i. \tag{3.7}$$

[4]Notice the difference with respect to the SX3 case, where only the ratio $-A_0/A_1$ is saved.

The closer the interpolating points, the better the results of this approximation. Therefore, it is recommended to apply small increments ($\lesssim 0.5$ V) to the voltages of the pulsed signals when saving the data used in this calibration step.

Independently on whether the linear or interpolation methods are used, each PC wire outputs a downstream and an upstream signal, which require its own calibration constants to translate the raw signals into downstream and upstream "voltages", V_d and V_u, respectively.

3.5.8 PC: Position Calibration

Similarly to the SX3 position determination, the position at which a charged particle crosses the center of the active cell of a PC wire is given by an expansion of ratio of the downstream (upstream) signal to the total signal. However, in this case, the calibrated SX3 signals are substituted by the PC "voltages", $V_{d,u}$. Moreover, there is no analogous to the SX3 back signal in the PC wires, thus, the "total voltage" is the sum of the upstream and downstream voltages. The downstream and upstream positions are then given by

$$p_s = \sum_{n=0}^{N} C_{s,n} \left(\frac{V_s}{V_d + V_u} \right)^n , \tag{3.8}$$

where $s = d, u$. In this case, both signals need to be present. Events exhibiting only a signal from one side are considered noise and are ignored. The final position is obtained from the average of p_d and p_u,

$$p = \frac{p_d + p_u}{2}. \tag{3.9}$$

Data from two ^{210}Po *needle* sources (approximately 5 mm long and 1 mm wide) is used for the purposes of position calibration. The sources are placed at known positions along the z-axis, close to the downstream and upstream ends of the proportional counter. Then, the chamber is filled with gas at conditions nearly identical to the ones used when sending the beam into ANASEN. It is assumed that all SX3

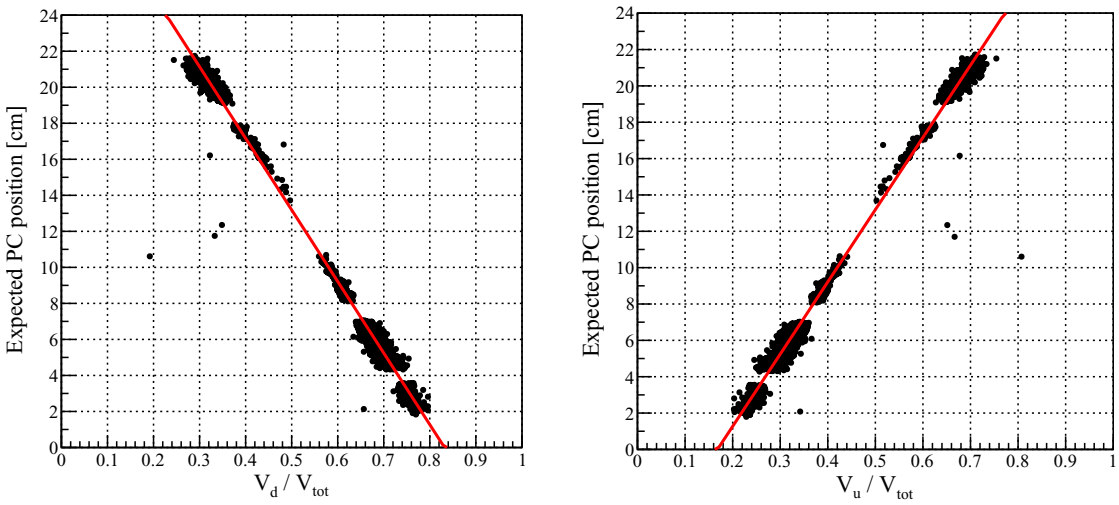

Figure 3.12: Expected position on a PC wire as function of the ratio of down-stream (left) or up-stream (right) voltage to total voltage. Data form two ^{210}Po needle sources placed at 5.0 and 21.5 cm from the forward silicon detectors.

detectors have been fully calibrated at this point. The final position of the mono-energetic alpha particles (see Table 3.4) emitted by the needle sources is know from the SX3 position and from the world coordinates file. The origin of the observed α particles (*i.e.* the downstream or upstream source) can be determined by comparing the reconstructed energy of the α particles to the emission energy of 5.304 MeV. The source which yields the smallest difference is selected as the origin of the α particle. The radius at which the PC wires are located, with respect to the z-axis, is $\rho_{\rm PC} = 3$ cm. If $i = (0, 0, z_i)$ and $f = (x_f, y_f, z_f)$ denote the initial and final points of the α particle track (from the source to the SX3 detector), then, the z-coordinate at which the particle is expected to cross the PC wire is given by

$$z_{\rm PC} = z_i - (z_i - z_f)\,\frac{\rho_{\rm PC}}{\sqrt{x_f^2 + y_f^2}}. \tag{3.10}$$

In the left (right) panel in Figure 3.12, the expected $z_{\rm PC}$ is plotted as a function of the measured ratio of the downstream (upstream) voltage to the total voltage. The linear behavior is evidenced by the red straight line resulting from the linear fit.

3.6 Event Reconstruction

The kinematic reconstruction of events in ANASEN is based on the geometrical determination of the reaction point, on the energy loss calculations of the beam and light particles and on the four-momentum conservation at the reaction point. In the sections below each of these elements is described in detail assuming *true* particle hits.

In the context of events registered by the detectors in ANASEN, a *true* particle hit (from now on referred simply as particle hit) is one where a full or partial SX3 hit[5] is registered and, in the same event, both signals from selected PC wires are also registered. Only selected coincidences of PC wires and SX3 detectors are considered, based on the geometrical constraints on the azimuthal angle of the trajectory of the light particle. These constraints arise from the fact that light particles, emanating from an interaction between the beam and target particles, are emitted radially outward from the beam axis. Scenarios in which an SX3 and PC wire show valid signals but the wire does not satisfy the geometrical constraints are regarded as random coincidences.

3.6.1 Reaction Point

Once the SX3 detectors and PC wires have been calibrated, each particle hit generates coordinates for two points along the particle trajectory, namely, an intermediate point, i, obtained from PC wire signals, and the final point, f, obtained from the SX3 detector signals. The so-called particle track, is represented by the vector going from the reaction point, r, to f, passing by i. To determine r, the points (x, y, z) along the particle track are parametrized as follows,

$$x = (x_f - x_i)t + x_i \tag{3.11}$$

$$y = (y_f - y_i)t + y_i \tag{3.12}$$

$$z = (z_f - z_i)t + z_i. \tag{3.13}$$

[5]A partial (full) hit in an SX3 detector needs two (three) signals: downstream or (and) upstream signal(s) from a single front strip and single signal from a back segment.

The parameter t is normalized such that at $t = 0$ ($t = 1$) the coordinates of point i (f) are recovered. The reaction point is assumed to be the point along the particle track closest to the z-axis (the beam direction). The distance, D, between a point on the track and the z-axis is given by $D = \sqrt{x^2 + y^2}$. Then, the parameter that minimizes D can be found by solving the equation

$$\left.\frac{\partial D}{\partial t}\right|_{t=t_r} = 0. \tag{3.14}$$

The solution is given by

$$t_r = -\frac{x_i(x_f - x_i) + y_i(y_f - y_i)}{(x_f - x_i)^2 + (y_f - y_i)^2}. \tag{3.15}$$

By substituting t_r in equations 3.12 to 3.13 the coordinates (x_r, y_r, z_r) of the reaction point are determined.

3.6.2 Energy Loss

In an active thick target, such as ANASEN, the kinematics of the particles involved in a reaction are affected by the gas in which they are moving. Ions travelling in a medium (also called absorber) experience a kinetic energy loss (mostly) due to the electromagnetic interaction between the ion and electrons in the molecules of the medium. The rate of energy loss for an ion travelling a differential distance, also known as *linear stopping power* (S), is described by the Bethe-Bloch formula[60, 61],

$$S \equiv -\frac{dE}{dx} = \frac{4\pi e^4 z^2 n Z}{m_e v^2} B, \tag{3.16}$$

where

$$B \equiv \ln\left(\frac{2m_e v^2}{I}\right) - \ln\left(1 - \frac{v^2}{c^2}\right) - \frac{v^2}{c^2}. \tag{3.17}$$

Here, m_e and e are the mass and charge of the electron, v and ze are the velocity and charge of the ion, n and Z are the number density and the atomic number of the absorber atoms. The parameter I represents the average excitation energy and ionization potential of the absorber and is normally determined experimentally[41]. In general, B varies slowly with v, hence the global behavior of dE/dx is primarily

determined by the multiplicative factor to the left of B in equation 3.16. The magnitude of dE/dx decreases for increasing ion velocity (kinetic energy). In contrast, for a given value of v, the ion looses more energy if it possesses a large charge (ze), if the absorber's density is high or if it is composed by atoms with large Z.

The program Stopping and Range of Ions in Matter (SRIM)[62] tabulates values of the stopping power as a function of the kinetic energy of the ion and depending on the medium's characteristics. An example of the SRIM output files is shown in Appendix D for α particles in a gas of molecular hydrogen (H_2) with pressure of 400 Torr and temperature of 294 K. By loading the corresponding table for an ion (proton, beam particle, etc.) into the ANASEN analysis program the energy loss is numerically integrated given the path length and the initial or final ion energy, depending on the case. To test the accuracy of the SRIM calculations, a ^{228}Th α source was placed inside the ANASEN chamber, which was filled with hydrogen gas (H_2) at 400 Torr and 294 K. The source was positioned along the z-axis, 26 cm from the forward SX3 detectors. In Figure 3.13, the final energy of the α particles is plotted against the distance of detection. The black solid lines, obtained from energy loss calculations using data generated by SRIM, show remarkable agreement with the experimental data. While the results presented here apply only for alpha particles in a very specific medium, more examples of the consistency of the SRIM calculations with heavier nuclei, in particular oxygen isotopes in hydrogen gas can be found in the SRIM website[6]. For the analysis of the present data, SRIM tables were calculated for protons, deuterons, ^{4}He, ^{17}O and ^{19}O particles in D_2 gas at 400 Torr and 294 K.

For each light particle hit, the programs developed for processing ANASEN data calculate the kinetic energy of the light particle at the point of reaction, $K_{l,r}$, by dividing the track length in N small segments of length Δs_l ($\sim 1/2$ mm) and then using the recursive formula

$$K_{l,n} = K_{l,n-1} + S_l(K_{l,n-1})\Delta s_l \,, \tag{3.18}$$

[6]Go to `www.srim.org` and then to the Experimental Data Plots link.

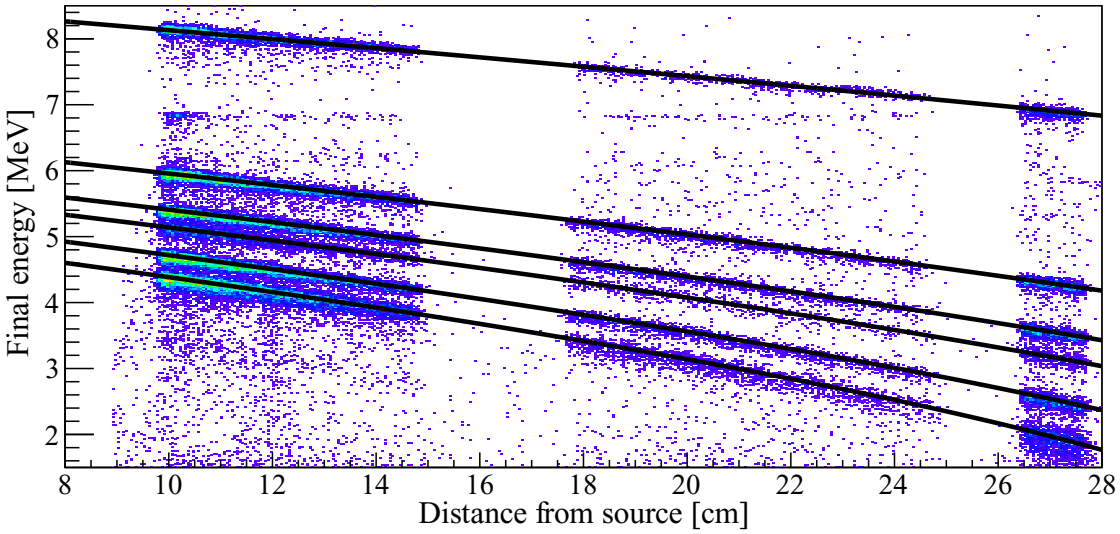

Figure 3.13: Alpha particles from a ^{228}Th source in H_2 gas at 400 Torr and 294 K. The source was placed at 26 cm with respect to the plane of the forward SX3 detectors. The solid black lines are calculated using stopping power tables generated by the program SRIM.

where the stopping power is interpolated for each point at the kinetic energy value computed in the preceding step, $K_{l,n-1}$. In the previous section, it was proven that the coordinates of the reaction point (x_r, y_r, z_r) can be obtained from points i and f, given by the PC and SX3 detectors, respectively. Then, the path length of the light particle is

$$D_{rf} = \sqrt{(x_f - x_r)^2 + (y_f - y_r)^2 + (z_f - z_r)^2}. \tag{3.19}$$

Therefore, the length of the track segments is

$$\Delta s_l = D_{rf}/N. \tag{3.20}$$

The point $n = 0$ corresponds to the final point on the particle track, f, where the kinetic energy of the light particle (measured by the SX3 detector) is $K_{l,f}$. At the opposite end of the track, the point $n = N$ coincides with the reaction point, r, where the calculated kinetic energy of the light particle is $K_{l,r}$.

On the other hand, the initial kinetic energy of the beam particle is known at the location of the window $(0, 0, z_w)$, where the beam enters the ANASEN chamber.

Uncertainties in the x and y initial beam coordinates due to the finite size of the beam spot are not taken into account in the current version of the data processing programs. However they are not expected to be large since a collimator with diameter of 5 mm was placed 5 cm upstream of the entrance window. The beam kinetic energy at the reaction point is determined by a recursive formula similar to 3.18 in which the energy loss is subtracted from the initial energy,

$$K_{b,n} = K_{b,n-1} - S_b(K_{b,n-1})\Delta s_b. \tag{3.21}$$

The track length of the beam particle is

$$D_{wr} = \sqrt{x_r^2 + y_r^2 + (z_w - z_r)^2} \tag{3.22}$$

and the length of the track segments is

$$\Delta s_b = D_{wr}/N. \tag{3.23}$$

In conclusion, the kinetic energy of the light recoil and beam particle at the reaction point is determined by the recursive relations 3.18 and 3.21, respectively. The final step in the event reconstruction is the computation of the excitation energy of the heavy recoil through the conservation of the total four-momentum.

3.6.3 Four-Momentum Conservation

Although four-momenta are generally used in special relativity and hence associated with fast-moving particles (*i.e.* $v/c \gtrsim 0.1$), their properties simplify the calculations of the excitation energy of the heavy recoils.

In the laboratory reference frame the conservation of four-momentum at the reaction point, r, can be written as,

$$P_b + P_t = P_l + P_h, \tag{3.24}$$

where the b, t, l and h subindices are for the beam, target, light recoil and heavy recoil, respectively. The components of the four-momenta P_b, P_t and P_l are determined

experimentally and have the explicit forms

$$P_b = \left((m_b^2c^2 + p_b^2)^{1/2},\, p_b\cos\phi_b\sin\theta_b,\, p_b\sin\phi_b\sin\theta_b,\, -p_b\cos\theta_b\right) \quad (3.25)$$

$$P_t = (m_t, 0, 0, 0) \quad (3.26)$$

$$P_l = \left((m_l^2c^2 + p_l^2)^{1/2},\, p_l\cos\phi_l\sin\theta_l,\, p_l\sin\phi_l\sin\theta_l,\, -p_l\cos\theta_l\right), \quad (3.27)$$

where $p_b = \sqrt{2m_bK_{b,r}}\left(1 + \frac{K_{b,r}}{2m_b}\right)^{1/2}$ and $p_l = \sqrt{2m_lK_{l,r}}\left(1 + \frac{K_{l,r}}{2m_l}\right)^{1/2}$ are the magnitudes of the linear momentum of the beam and light particles, respectively. The azimuthal angles $\phi_{b,l} \in [-\pi, \pi)$ are measured with respect to the x-axis. The angles $\theta_{b,l} \in [0, \pi)$ are measured with respect to the $(-z)$-axis. Note that the standard polar angle is $(\pi - \theta_{b,l})$, hence the minus sign in the 4th component of the four-momenta above. All angles are extracted from the vectors representing the particle tracks.

In the case of the four-momentum of the heavy particle, the minimum rest energy is given by m_hc^2. Any excess energy can be regarded as excitation energy, $E_{\rm exc}$, of the heavy recoil in its rest frame. Then, the explicit form of the four-momentum of the heavy recoil is

$$P_h = \left(\left[\frac{(m_hc^2 + E_{\rm exc})^2}{c^2} + p_h^2\right]^{1/2}, \boldsymbol{p}_h\right) \quad (3.28)$$

where $\boldsymbol{p}_h$ is the unobserved linear momentum. From conservation of the total four-momentum (equation 3.24) P_h can be expressed in terms of the fully determined four-momenta of the beam, target and light particles,

$$P_h = P_b + P_t - P_l. \quad (3.29)$$

Finally, the excitation energy can be extracted by squaring P_h,

$$\frac{(m_hc^2 + E_{\rm exc})^2}{c^2} = P_h \cdot P_h \quad (3.30)$$

$$E_{\rm exc} = c\sqrt{P_h \cdot P_h} - m_hc^2 \quad (3.31)$$

A more classical approach to calculate the excitation energy can be found in the appendix C.1 of Ref. [48]. Tests with the data of the present experiment have been performed yielding the same energy of excitation spectra, thus confirming the equivalence between both methods.

3.7 Results

3.7.1 Particle Identification

Alternatively to the particle identification method described in section 2.4.1, where the energy loss of the residual particles was plotted against their time of flight, particle identification can be attained by plotting the energy loss against the final energy. In ANASEN, these two quantities are obtained for the light particles from the PC signals and the SX3 energy. Figure 3.14 (top) shows an example of a particle identification plot obtained from the stable beam test, ^{17}O+d. The regions of points corresponding to α particles, deuterons and protons are tagged with "α", "d" and "p", respectively. Deutrons and protons can be readily separated for final energy values less than 5 MeV. However, both regions merge for larger energies, making their separation more difficult. The points in the region of α particles are rather scattered, but they collapse into a narrow band once the so-called *path corrections* are made, as shown in Figure 3.14 (bottom). The correction approximates the PC signals to the characteristic energy loss of the particles, by effectively making constant the length of the path travelled by the particle in the PC cell. This is done by multiplying the PC signal by $\sin\theta_l$, where θ_l is the angle of the light particle trajectory, measured from the $(-z)$-axis. Path-corrected plots, such as the one in Figure 3.14 (bottom), were used to identify light particles emitted in the reactions in the stable (^{17}O) and radioactive (^{19}O) beam experiments.

3.7.2 Excitation Energy Spectrum

Once the light particles are identified, the kinematic reconstruction can be performed using the steps described in section 3.6. Figure 3.15 shows one of the excitation energy spectra of ^{20}O generated in the ^{19}O(d,p) reactions in ANASEN, gated on beam energy between 42 and 52.5 MeV and proton scattering angle between 35 and 160° (in the laboratory reference frame). The dark blue histogram is a statistical prediction of the background based on the sensitive non-linear iterative peak clipping algorithm[63]. The black dashed lines represent the location of the main peaks observed by Hoffman

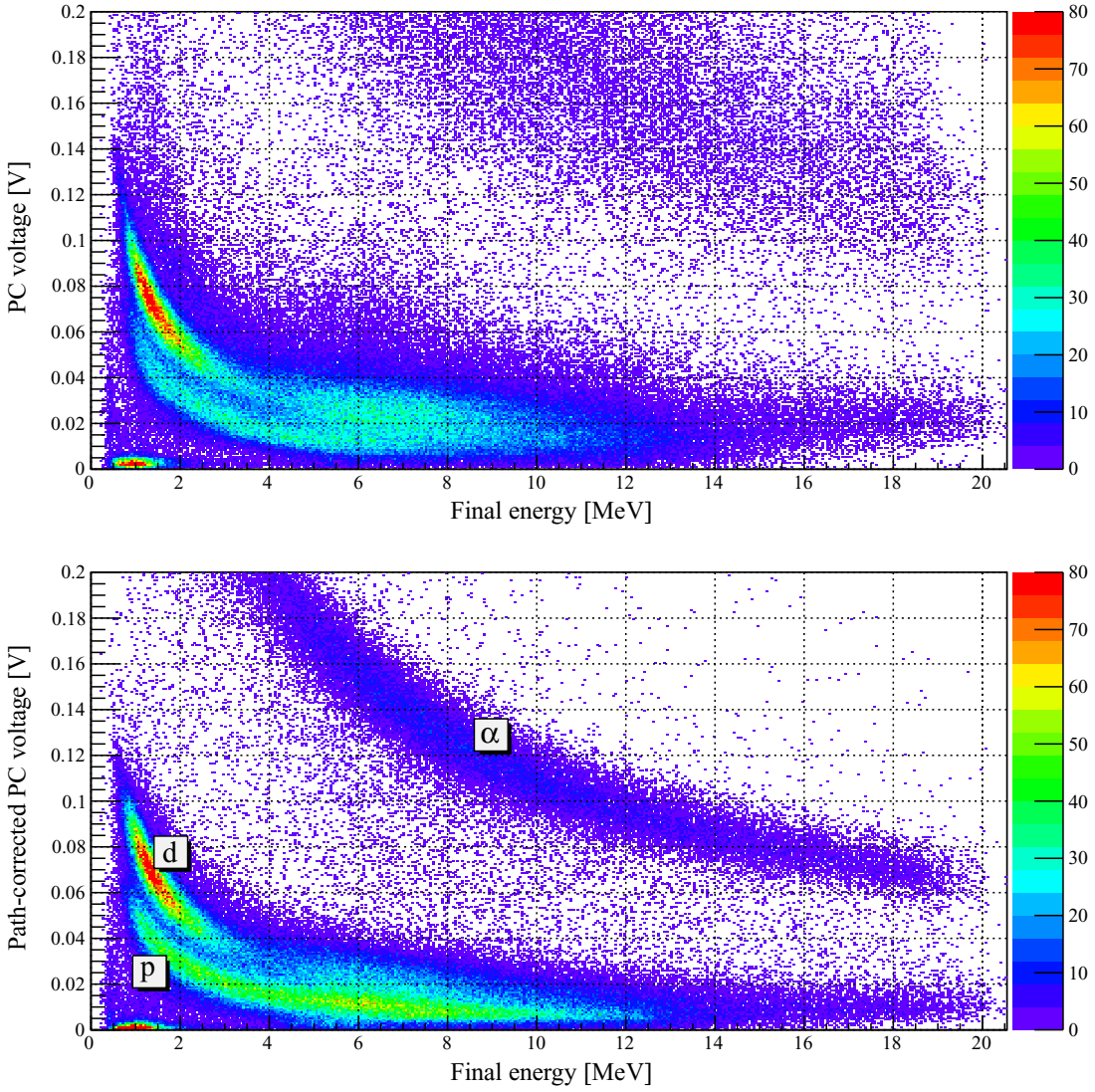

Figure 3.14: Uncorrected (top) and corrected (bottom) PC voltage plotted against the final energy measured by the SX3s. Clusters of data points for protons, deuterons and alpha particles are labelled with "p", "d" and "α", respectively.

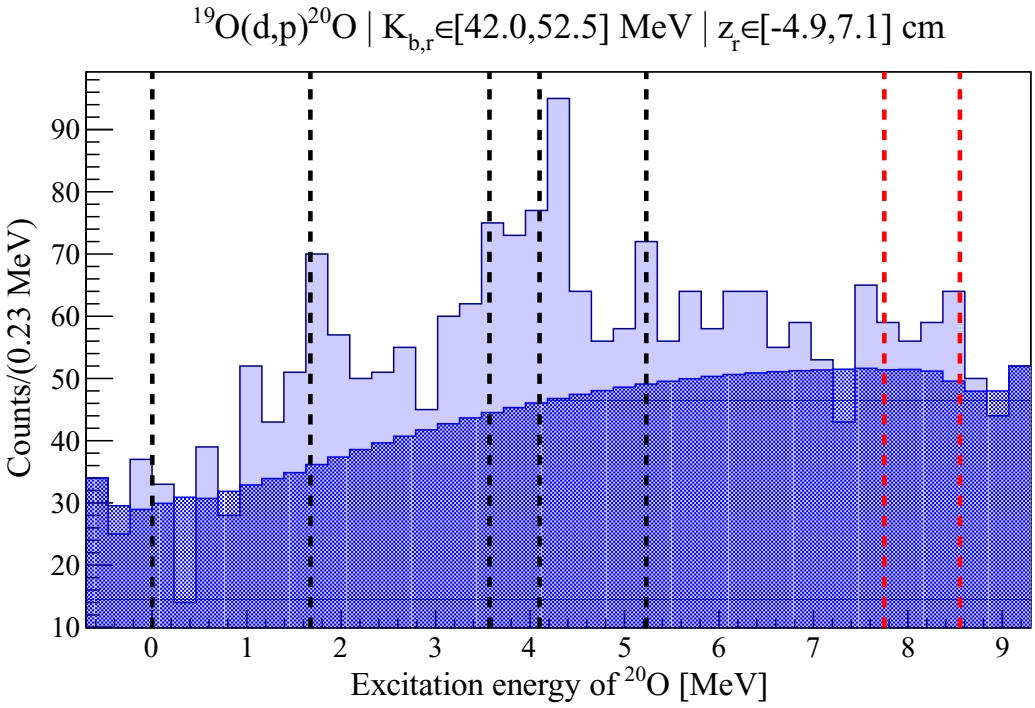

Figure 3.15: Energy of excitation spectrum of ^{20}O obtained through the ^{19}O(d,p) reaction in inverse kinematics. Only reactions with a reconstructed beam energy between 42 and 52.5 MeV (or equivalently a reaction z coordinate between -4.9 and 7.1 cm) and θ_l^{lab} from 35 to 165° were considered.

et al. [52] (see Figure 3.3). The spectrum from the present experiment shows peaks at the same locations with similar relative intensities, demonstrating that the selected protons were emitted from the ^{19}O$(d,p)^{20}$O reaction. The red dashed lines represent the location of known neutron unbound states in ^{20}O, namely, a 4^+ at 7.75 MeV and another 4^+ at 8.55 MeV[64]. The presence of the mentioned unbound states is hinted by the small peaks observed in the spectrum at those excitation energies. Considering that the excitation energy spectrum of ^{20}O spectrum shown here was generated from approximately 48 hours of beam time, a longer experimental campaign could solve the problem of low statistics. Moreover, coincidences with identified heavy recoils has proven to significantly reduce the background in experiments with radioactive beams. Therefore, it is recommended to utilize an ionization chamber downstream of ANASEN for the detection and separation of the heavy recoils.

3.8 Conclusions

The anomalous behavior of the neutron dripline on the oxygen isotopic chain can be interpreted in terms of the evolution of the single-particle energies of the *sd* orbitals for increasing neutron number. Theoretical models relying only on nucleon-nucleon interactions fail to predict location of the last bound oxygen isotope, ^{24}O, which was experimentally established by Fauerbach *et al.* [45] and by Hoffman *et al.* [46]. On the other hand, nuclear models based on phenomenological forces, such as the USD-B and SDPF-M, and models including three-body forces are consistent with the experimental location of the neutron dripline. To determine which interaction provides a better description of the nuclear force, experiments to extract the spectroscopic factors of the neutron $0d_{3/2}$ orbital in neutron-rich oxygen isotopes are necessary.

From the results by Hoffman *et al.* [52], spectroscopic factors of excited states in ^{20}O are compared to shell-model calculations, showing remarkable agreement. States with energy of excitation less than 6 MeV where populated, yet most of the strength of the $0d_{3/2}$ orbital are predicted to be at larger excitation energies. Result from the present experiment to study ^{20}O, show the capabilities of the new active gas target/detector ANASEN and prove the success in producing a radioactive ^{19}O beam at the John D. Fox Superconducting Accelerator Laboratory. The results also show that, identification of the light particles is possible by using pure deuterium gas in the proportional counter. Due to time constraints and technical limitations in the detection of the heavy recoils, the statistics achieved in the present experiment were too low for a more in depth analysis of ^{20}O, although bound excited states were observed.

Identification of the heavy recoils has proven to be necessary for the background reduction of the excitation energy spectra extracted from ANASEN. This could be achieved by placing a ΔE-E telescope inside the active volume of the detector. However, the development of such heavy-recoil detector and the mechanism to remotely change its position along the beam line is a complicated task and may need several months to be fulfilled. Alternatively, if the beam particles are not stopped within the

active volume of ANASEN, an ionization chamber may be place immediately after ANASEN, provided that the window separating the two volumes can withstand the pressure differences from the gasses in ANASEN and in the ionization chamber.

3.9 Summary

In order to study the location and fragmentation of the $0d_{3/2}$ orbital in ^{20}O a beam of the short-lived ^{19}O was produced at the RESOLUT radioactive beam facility of the Florida State University. The new the active gas target detector ANASEN, for which extensive data analysis and calibration codes were created, was used to measure the light-recoiling particles emitted from the reactions induced in its active volume filled with pure deuterium gas. ^{20}O was produced via the direct neutron-transfer reaction (d, p) from the incident ^{19}O beam. In a separate experiment, data from the $^{17}\mathrm{O}(d, p)^{18}\mathrm{O}$ reaction was acquired to verify our experimental methods and analysis techniques. The excitation energy spectrum of ^{20}O, extracted from the detected protons and from the reactions kinematics reconstruction, shows clear evidence of well-known bound states and suggests the presence of neutron unbound states. However, due to large background from other proton-emitting reactions spectroscopic factors could not be derived. Repetition of these measurements with ANASEN is proposed with the addition of a heavy-recoil detector to reduced the proton background.

APPENDIX A

RELATIVISTIC DOPPLER EFFECT

The relativistic Doppler effect is the change in the photon's frequency, ν, emitted by a source moving with respect to the observer as compared to the *true* frequency of the same photon, ν_0, in the reference frame where the source is at rest[26]. The frequency of a photon is proportional to its energy, $E_\gamma = h\nu$, where $h = 6.62606957(29) \times 10^{34}$ J·s is Planck's constant. Thus, corrections to the photons frequency are equivalent to corrections to its energy.

The relativistic Doppler effect follows as a consequence of the invariance of *intervals* in four-dimensional space. Let $P_s^{\rm lab} = (E_s^{\rm lab}/c, p_s^{\rm lab}\hat{z})$ be the four-momentum of the source (nucleus) travelling with speed v in the $\hat{z}$ direction. From special relativity the energy and magnitude of the (three-)momentum are

$$E_s^{\rm lab} = \frac{m_s c^2}{\sqrt{1-(v/c)^2}} \tag{A.1}$$

$$p_s^{\rm lab} = \frac{m_s v}{\sqrt{1-(v/c)^2}}. \tag{A.2}$$

Let $P_\gamma^{\rm lab} = \left(E_\gamma^{\rm lab}/c, E_\gamma^{\rm lab}/c\,\hat{u}\right)$ be the four-momentum of a photon emitted in the laboratory reference frame by the moving source, such that $\hat{z}\cdot\hat{u} = \cos\theta_\gamma^{\rm lab}$, where $\theta_\gamma^{\rm lab}$ is the angle at which the photon is detected. Similarly, in the source's rest frame the four-momenta for the source and photon are $P_s^s = (m_s c, \mathbf{0})$ and $P_\gamma^s = \left(E_\gamma^s/c, E_\gamma^s/c\,\hat{w}\right)$, respectively. In virtue of the invariance of the intervals under Lorentz transformations, one can draw the following equality among the intervals squared of the total four-

momentum in both reference frames:

$$\left(P_s^s + P_\gamma^s\right)^2 = \left(P_s^{\text{lab}} + P_\gamma^{\text{lab}}\right)^2 \tag{A.3}$$

$$(P_s^s)^2 + (P_\gamma^s)^2 + 2P_s^s \cdot P_\gamma^s = (P_s^{\text{lab}})^2 + (P_\gamma^{\text{lab}})^2 + 2P_s^{\text{lab}} \cdot P_\gamma^{\text{lab}} \tag{A.4}$$

$$m_s^2c^2 + 0 + 2m_sE_\gamma^s = m_s^2c^2 + 0 + 2\left(E_s^{\text{lab}}E_\gamma^{\text{lab}}/c^2 - p_s^{\text{lab}}E_\gamma^{\text{lab}}/c\hat{z}\cdot\hat{u}\right) \tag{A.5}$$

$$m_sE_\gamma^s = E_s^{\text{lab}}E_\gamma^{\text{lab}}/c^2 - p_s^{\text{lab}}E_\gamma^{\text{lab}}/c\cos\theta_\gamma^{\text{lab}} \tag{A.6}$$

Substituting equations A.1 and A.2,

$$m_sE_\gamma^s = \frac{m_sc^2}{\sqrt{1-(v/c)^2}}E_\gamma^{\text{lab}}/c^2 - \frac{m_sv}{\sqrt{1-(v/c)^2}}E_\gamma^{\text{lab}}/c\cos\theta_\gamma^{\text{lab}} \tag{A.7}$$

$$E_\gamma^s = E_\gamma^{\text{lab}}\frac{1-v/c\cos\theta_\gamma^{\text{lab}}}{\sqrt{1-(v/c)^2}} \tag{A.8}$$

Equation A.8 shows the Doppler-corrected energy of the photon. As an example, consider two photons $\gamma 1$ and $\gamma 2$, both with $E_{\gamma 1}^{\text{lab}} = E_{\gamma 2}^{\text{lab}} = 1$ MeV and emitted at $\theta_{\gamma 1}^{\text{lab}} = 90^\circ$ and $\theta_{\gamma 2}^{\text{lab}} = 30^\circ$ by a source travelling at $v/c = 0.4$. The energy of $\gamma 1$ in the rest frame of the source $E_{\gamma 1}^s = 1.091$ was incremented with respect to the value in the laboratory reference frame. On the other hand, the opposite comportment is shown by $\gamma 2$, since $E_{\gamma 2}^s = 0.713$ MeV.

In conclusion, if an excited nucleus travelling at relativistic speeds emits a photon at an angle $\theta_\gamma^{\text{lab}}$ in a transition to a less excited state, the measured energy of the photon in the laboratory reference frame must account for the corrections of this effect in order to get the actual photon's energy in the rest frame of the nucleus.

APPENDIX B

CHANNEL MAP FILES

The channel map files are plain text files where each row maps the information of one channel in ASIC or the CAEN modules into the respective detector. The ANASEN data processing programs assume a fixed format for the channel map files. If the current programs are to be reused, the user must keep the same format when creating his or her own channel map files. Descriptions and examples of the channel maps used in the data analysis of the present experiments are given in this appendix.

B.1 ASIC Map

In the ASIC channel map, the sequence of the elements in one row is as follows:

`MB`: integer representing the ASIC motherboard identification number.

`Chip`: integer representing the ASIC chip identification number in an ASIC motherboard.

`Chan`: integer representing the ASIC channel identification number for a given ASIC chip and motherboard.

`DetType`: string of characters with no spaces corresponding to the type of detector (current possible values are SX3 and Q3).

`DetID`: integer representing the identification number of a detector of a given type.

`DetCh`: integer representing the channel in the detector.

`Comment`: string of characters (spaces allowed) reserved for comments or description of channel.

A fragment of the ASIC channel map is shown below.

```
MB    Chip  Chan  DetType    DetID      DetCh      Comment                  1
1     5     4     SX3        0          0          F_A_Back                 2
1     5     5     SX3        0          3          F_A_Back                 3
1     5     6     SX3        0          2          F_A_Back                 4
1     5     7     SX3        0          1          F_A_Back                 5
...                                                                         6
2     1     12    SX3        29         1          IIb_F_Back               7
2     1     13    SX3        29         2          IIb_F_Back               8
2     1     14    SX3        29         3          IIb_F_Back               9
2     1     15    SX3        29         0          IIb_F_Back               10
1     9     8     SX3        0          11         F_A_Front                11
1     9     9     SX3        0          7          F_A_Front                12
1     9     10    SX3        0          10         F_A_Front                13
1     9     11    SX3        0          6          F_A_Front                14
1     9     12    SX3        0          5          F_A_Front                15
1     9     13    SX3        0          9          F_A_Front                16
1     9     14    SX3        0          4          F_A_Front                17
1     9     15    SX3        0          8          F_A_Front                18
...                                                                         19
2     6     0     SX3        29         11         IIb_F_Front              20
2     6     1     SX3        29         7          IIb_F_Front              21
2     6     2     SX3        29         10         IIb_F_Front              22
2     6     3     SX3        29         6          IIb_F_Front              23
2     6     4     SX3        29         5          IIb_F_Front              24
2     6     5     SX3        29         9          IIb_F_Front              25
2     6     6     SX3        29         4          IIb_F_Front              26
2     6     7     SX3        29         8          IIb_F_Front              27
```

B.2 CAEN Map

In the CAEN channel map, the sequence of the elements in one row is as follows:

`Module`: integer representing the CAEN module identification number.

`Channel`: integer representing the CAEN channel identification number for a given module.

`DetType`: string of characters with no spaces corresponding to the type of detector (current possible values are IC, PC, MCP, SiPM and RF).

`DetID`: integer representing the identification number of a detector of a given type.

`DetCh`: integer representing the channel in the detector.

`Comment`: string of characters (spaces allowed) reserved for comments or description of channel.

A fragment of the CAEN channel map is shown below.

```
Module    Channel   DetType   DetID     DetCh     Comment                          1
7         0         IC        0         0         IC RawE 0                        2
7         1         IC        0         1         IC RawE 1                        3
7         2         IC        0         2         IC RawE 2                        4
4         0         PC        0         1         PC wire 0 upstream               5
4         1         PC        1         1         PC wire 1 upstream               6
...                                                                                  7
5         17        PC        17        0         PC wire 17 downstream            8
5         18        PC        18        0         PC wire 18 downstream            9
11        0         SiPM      0         0         Silicon photo-multiplier time    10
11        1         RF        0         0         RF time                          11
11        16        MCP       0         0         MCP chan 0                       12
11        17        MCP       0         1         MCP chan 1                       13
11        18        MCP       0         2         MCP chan 2                       14
11        19        MCP       0         3         MCP chan 3                       15
```

B.3 World Coordinates File

In the *world coordinates* file, the sequence of the elements in one row is as follows:

`DetID`: integer representing the identification number of an SX3 detector.

`ZOffset`: z-position of the edge of the detector's active area closest to the plane of forward detectors (the "downstream edge").

`X0`: x-coordinate of the corner formed by the downstream edge and front strip 0.

`X4`: x-coordinate of the corner formed by the downstream edge and front strip 4.

`Y0`: y-coordinate of the corner formed by the downstream edge and front strip 0.

`Y4`: y-coordinate of the corner formed by the downstream edge and front strip 4.

`Comment`: string of characters (spaces allowed) reserved for comments.

An example of a world coordinates file is shown below.

```
DetID   ZOffset     X0        X4        Y0        Y4        Comment          1
6         3.1       -2.00     2.0       8.9       8.9       R1a_A            2
7         3.1       -6.30     -2.55     6.65      8.7       R1a_B            3
8         3.1       -8.70     -6.55     2.55      6.3       R1a_C            4
9         3.1       -8.90     -8.9      -2.0      2.0       R1a_D            5
10        3.1       -6.65     -8.7      -6.3      -2.55     R1a_E            6
11        3.1       -2.55     -6.3      -8.7      -6.65     R1a_F            7
12        3.1       +2.0      -2.0      -8.9      -8.9      R1b_A            8
13        3.1       +6.3      2.55      -6.65     -8.7      R1b_B            9
14        3.1       +8.7      6.65      -2.55     -6.3      R1b_C            10
15        3.1       +8.9      8.9       2.0       -2.0      R1b_D            11
16        3.1       +6.65     8.7       6.3       2.55      R1b_E            12
```

```
17      3.1     +2.55   6.3     8.7     6.65    R1b_F
18      14.3    -2.0    2.0     8.9     8.9     R2a_A
19      14.3    -6.3    -2.55   6.65    8.7     R2a_B
20      14.3    -8.7    -6.65   2.55    6.3     R2a_C
21      14.3    -8.9    -8.9    -2.0    2.0     R2a_D
22      14.3    -6.65   -8.7    -6.3    -2.55   R2a_E
23      14.3    -2.55   -6.3    -8.7    -6.65   R2a_F
24      14.3    +2.0    -2.0    -8.9    -8.9    R2b_A
25      14.3    +6.3    2.55    -6.65   -8.7    R2b_B
26      14.3    +8.7    6.65    -2.55   -6.3    R2b_C
27      14.3    +8.9    8.9     2.0     -2.0    R2b_D
28      14.3    +6.65   8.7     6.3     2.55    R2b_E
29      14.3    +2.55   6.3     8.7     6.65    R2b_F
```

APPENDIX C

ROOT SCRIPTS

Examples of ROOT scripts for the conversion of `.evt` files to `.root` files, for the calibration of SX3 and PC detectors in ANASEN and for the conversion of the "raw" event data structure (with ADC module and channel and ASIC motherboard, chip and channel) to the "physical" event data structure (with particle final and intermediate position, energy, etc.) are presented in this appendix. The scripts are also included as a supplement to this dissertation. The codes for the detector classes and the event processor are only included as a supplement. Each script contains a brief description of what is mean to accomplish and how to execute it in a terminal (its *usage*). Most of the parameters utilized by the scripts are enclosed in the `CONTROL PANEL` section, although, for the calibration scripts modification of the parameters unique to each step of the calibration is necessary (this was kept to a minimum for the rest of the scripts). All the scripts require precompilation of the `EventPorcessor` class and the user is responsible for specifying the path to the compiled library as a constant string in the function `gSystem->Load(path)`. The classes can be easily compiled with three simple steps using ROOT's Automatic Compiler of Libraries for CINT (ACLiC). For example, in the case of the `EventPorcessor`, these steps are:

1. Open a terminal and `cd` to the directory where the class `cpp` and `hpp` files are located.
2. Run ROOT by typing: `root`
3. Compile the code by typing: `.L EventProcessor.cpp++`

C.1 To Convert .EVT to .ROOT Files With Raw Events

```
////////////////////////////////////////////////////////////////////////////////
// Script name: evt2root.C
//
// Description: Script that converts an .evt file to a .root file.  It requires the
//              user to provide the name of the text file containing the list of .evt
//              files to be converted, as well as the number of 'words' in each
//              buffer used when reading the evt files.
//
// Example of list file:
// ------------------------------------------------------------------------------
// Output file: /data/ROOT_Files/r1361-2.root
// Input file(s) directory: /data/EVT_Files/
// 1361
// 1362
// ------------------------------------------------------------------------------
//
// Usage: root -l evt2root.C
//
// Created by: Daniel Santiago-Gonzalez
// Date: March 2013
////////////////////////////////////////////////////////////////////////////////
{
  //============================================================================
  // CONTROL PANEL
  //============================================================================
  string ListOfFiles = "data_files.list";
  int BufferWords = 13328;
  //============================================================================
  gSystem->Load("/DataAnalysisProject/ANASEN/EventProcessor_cpp.so");
  EventProcessor* EP = new EventProcessor();
  EP->ConvertEVTtoROOT(ListOfFiles, BufferWords);
}
```

C.2 For the Calibration of the SX3 Detectors

```
////////////////////////////////////////////////////////////////////////////////
// Script name: CalibrateSX3.C
//
// Description: Full calibration script for SX3 detectors in ANASEN.  Different
//              steps in the calibration procedure can be enabled by the 'switches'
//              (boolean parameters) below.  For each enabled switch, the correspond-
//              ing calibration will be performed from InitialDet to FinalDet.
//
// Usage: root -l CalibrateSX3.C
//
// Created by: Daniel Santiago-Gonzalez
// Date: March 2013
////////////////////////////////////////////////////////////////////////////////
{
  //============================================================================
  // CONTROL PANEL
  //============================================================================
  // General parameters:
```

```
string DataDir = "/data/ROOT_Files/";
string FilteredFilesDir = "/data/ROOT_Files/FilteredFiles/";
string TreeName = "DataTree";
string ParamDir = "../Parameters/";
string ASIC_map = "ASIC_channel_map.2013-05-17";
string CAEN_map = "CAEN_channel_map.2013-03-25";
string SX3_PC_combinations = "SX3_PC_Combinations.2013-04-10";
string SX3_CsI_combinations = "SX3_CsI_Combinations.2013-05-27";
int InitialDet = 7;
int FinalDet = 7;
bool UseFilteredFiles = 1;  // If active, it will use filtered files when possible.
// Number of detectors and maximum multiplicity:
int N_Q3 = 0;
int N_SX3 = 30;
int N_PC = 19;
int N_CsI = 36;
int MaxMult = 10;
// Calibration switches:
bool NewPulserOffsets = 1;
bool OneChannePulserCal = 0; int Det = 6;  int Chan = 4;
bool CalibrateEnergy = 1;
bool FrontBackCalibration = 1;
bool CalibratePosition = 1;
// Extra switches:
bool MakeBorderHits = 0;
bool SetNewThresholds = 0;
//============================================================================
bool FileStatus;
float MinQ, MaxQ, MaxDiff, MinE, MaxE;
// Load the library.
gSystem->Load("/DataAnalysisProject/ANASEN/EventProcessor_cpp.so");
// Event processor.
EventProcessor* EP = new EventProcessor();
EP->SetSystemPointer(gSystem);
EP->SetMaxMemory(8000);
EP->SetTreeName(TreeName);
EP->SetParamDirectory(ParamDir);
EP->SetChannelMap(ASIC_map, CAEN_map);
EP->CreateDetectors(N_Q3, N_SX3, N_PC, N_CsI, MaxMult, SX3_PC_combinations,
                    SX3_CsI_combinations);
EP->LoadParamsSelectedDetectors("SX3", InitialDet, FinalDet);
//----------------------------------------------------------------------------
if (NewPulserOffsets) {
  int NPeaks = 17;
  float PeakSigma = 7.0;
  float MinPeakAmplitude = 0.05;
  float NormalChi2Value = 0.03;
  FileStatus = EP->OpenROOTFile(DataDir+"r1327_ASIC_pulser.root");
  if (FileStatus) {
    EP->SetBranches();
    EP->SetPeakFindingParameters(NPeaks, PeakSigma, MinPeakAmplitude,
                                 NormalChi2Value);
    if (OneChannePulserCal) {
      // In case you need to do only one channel use this.
      float SpecialVolts[16] = {0.5,1,1.5,2,2.5,3,3.5,4,4.5,5,5.5,6,6.5,7,7.5,8};
      EP->SX3_GetPulserOffsetsOneChannel(SpecialVolts, Det, Chan);
    } else {
      // This is the most common case.
      float Volts[17] = {0.25,0.5,1,1.5,2,2.5,3,3.5,4,4.5,5,5.5,6,6.5,7,7.5,8};
      EP->SX3_GetPulserOffsets(Volts, InitialDet, FinalDet);
    }
    EP->ResetChain();
  }
}
//----------------------------------------------------------------------------
```

```
  if (CalibrateEnergy) {
    int NPeaks = 6;
    float SourcesPeaks[6]={5.41, 5.685, 6.06, 6.288, 6.778, 8.785};
    // SourcePeaks[0] is the expected value from the sum of the peaks at 5.340 and
    // 5.423 MeV taking into account their relative decay probabilities (for 228Th
    // decay chain). SourcePeaks[2] is similarly obtained from the peaks at 6.051 and
    // 6.090 MeV.
    float PeakSigma = 2;
    float MinPeakAmplitude = 0.025;
    MinQ=2000;  MaxQ=6000;
    if (UseFilteredFiles) {
      FileStatus = 1;
      for (int d=InitialDet; d<=FinalDet; d++)
        FileStatus *= EP->OpenROOTFile(FilteredFilesDir +
                                       Form("r1334-6_228Th_in_vacuum_SX3_%i.root",d));
    } else {
      FileStatus = EP->OpenROOTFile(DataDir+"r1334-6_228Th_in_vacuum.root");
    }
    if (FileStatus) {
      int SX3_back_ref[30];
      for (int i=0; i<30; i++) SX3_back_ref[i] = 3;
      EP->SetBranches();
      EP->SetPeakFindingParameters(NPeaks, PeakSigma, MinPeakAmplitude);
      EP->SX3_CalibrateEnergy(SX3_back_ref, SourcesPeaks, MinQ, MaxQ,
                              InitialDet, FinalDet);
      EP->ResetChain();
    }
  }
  //---------------------------------------------------------------------------
  if (FrontBackCalibration) {
    MaxDiff = 800;
    const int Cuts=8;
    float EnergyCuts[Cuts] = ={1.5,2.0,2.5,3.5,4.5,5.41,8.785,12};
    float Uncertainty = 0.04;
    if (UseFilteredFiles) {
      FileStatus = 1;
      for (int d=InitialDet; d<=FinalDet; d++)
       FileStatus *= EP->OpenROOTFile(FilteredFilesDir +
                                       Form("r1215-24_SX3_%i.root", d));
    } else {
      FileStatus = EP->OpenROOTFile(DataDir+"r1215-24.root");
    }
    if (FileStatus) {
      EP->SetBranches();
      EP->SX3_CalibrateFrontBack(MaxDiff, Cuts, EnergyCuts, Uncertainty,
                                 InitialDet, FinalDet);
      EP->ResetChain();
    }
  }
  //---------------------------------------------------------------------------
  if (MakeBorderHits) {
    FileStatus = EP->OpenROOTFile(DataDir+"r1215-24.root");
    if (FileStatus) {
      EP->SetBranches();
      EP->SX3_MakeBorderHitsFile(DataDir+"r1215-24_border_hits.root",300,7000);
      EP->ResetChain();
    }
  }
  //---------------------------------------------------------------------------
  if (CalibratePosition) {
    MinE = 0;  MaxE = 20;
    int NPeaks = 3;
    float PeakSigma = 3;
    float MinPeakAmplitude = 0.15;
    float NormalChi2Value = 0.03;
```

```
    EP->SetPeakFindingParameters(NPeaks, PeakSigma, MinPeakAmplitude,
                                 NormalChi2Value);
    FileStatus = EP->OpenROOTFile(DataDir+"r1215-24_border_hits.root");
    if (FileStatus) {
      EP->SetBranches();
      EP->SX3_CalibratePosition(MinE, MaxE, InitialDet, FinalDet);
      EP->ResetChain();
    }
  }
  //-------------------------------------------------------------------------------
  if (SetNewThresholds) {
    FileStatus = EP->OpenROOTFile(DataDir+"r1216.root");    // Stable beam data.
    if (FileStatus) {
      EP->SetBranches();
      EP->SX3_SetThresholds(3000, InitialDet, FinalDet);
      EP->ResetChain();
    }
  }
}
```

C.3 For the Calibration of the PC Wires

```
////////////////////////////////////////////////////////////////////////////////
// Script name: CalibratePC.C
//
// Description: Full calibration script for PC wires in ANASEN.  Different steps in
//              the calibration procedure can be enabled by the 'switches' (boolean
//              parameters) below.  For each enabled switch, the corresponding cali-
//              bration will be performed from InitialWire to FinalWire.
//
// Usage: root -l CalibratePC.C
//
// Created by: Daniel Santiago-Gonzalez
// Date: March 2013
////////////////////////////////////////////////////////////////////////////////
{
  //============================================================================
  // CONTROL PANEL
  //============================================================================
  // General parameters:
  string DataDir = "/data/ROOT_Files/";
  string FilteredFilesDir = "/data/ROOT_Files/FilteredFiles/";
  string TreeName = "DataTree";
  string ParamDir = "../Parameters/";
  string ASIC_map = "ASIC_channel_map.2013-05-17";
  string CAEN_map = "CAEN_channel_map.2013-03-25";
  string World_coords = "WorldCoordinates.2012-06-14";
  string SX3_PC_combinations = "SX3_PC_Combinations.2013-04-10";
  int InitialWire = 17;
  int FinalWire = 17;
  bool UseFilteredFiles = 0;  // If active, it will use filtered files when possible.
  // Number of detectors and maximum multiplicity:
  int N_Q3 = 0;
  int N_SX3 = 30;
  int N_PC = 19;
  int N_CsI = 36;
  int MaxMult = 10;
  // Calibration switches:
```

```
  bool NewPulserOffsets = 1;
  bool CalibratePosition = 1;
  //============================================================================
  bool FileStatus;
  // Load the event processor library.
  gSystem->Load("/DataAnalysisProject/ANASEN/EventProcessor_cpp.so");
  // Event processor.
  EventProcessor* EP = new EventProcessor();
  EP->SetSystemPointer(gSystem);
  EP->SetMaxMemory(8000);
  EP->SetTreeName(TreeName);
  EP->SetParamDirectory(ParamDir);
  EP->SetChannelMap(ASIC_map, CAEN_map, World_coords);
  EP->CreateDetectors(N_Q3, N_SX3, N_PC, N_CsI, MaxMult, SX3_PC_combinations);
  //----------------------------------------------------------------------------
  if (NewPulserOffsets) {
    int NPeaks = 11;
    float PeakSigma = 7.0;
    float MinPeakAmplitude = 0.05;
    float NormalChi2Value = 0.03;
    EP->LoadParamsSelectedDetectors("PC", InitialWire, FinalWire);
    FileStatus = EP->OpenROOTFile(DataDir+"r1328_CAEN_pulser.root");
    if (FileStatus) {
      EP->SetBranches();
      EP->SetPeakFindingParameters(NPeaks, PeakSigma, MinPeakAmplitude,
                                   NormalChi2Value);
      float Volts[11] = {0.025, 0.05, 0.1, 0.15, 0.2, 0.3, 0.4, 0.5, 0.6, 0.7, 0.8};
      EP->PC_GetPulserCoeffs(Volts, InitialWire, FinalWire);            // Option 1
      //EP->PC_GetPulserCentroids(Volts, 0, 4096, InitWire, FinalWire); // Option 2
    }
  }
  //----------------------------------------------------------------------------
  if (CalibratePosition) {
    // We use needle source data to calibrate the wires.
    string AlphaELossFile = "a_in_H2_400Torr.eloss";
    float pos_source_DS = 5;
    float pos_source_US = 21.5;
    EP->LoadDetectorsParameters();
    FileStatus = EP->OpenROOTFile(DataDir + "r1330-2_210Po_in_H2_400Torr.root");
    EP->DataFraction = 0.25;
    if (FileStatus) {
      EP->SetBranches();
      EP->PC_CalibratePosition(pos_source_DS, pos_source_US, AlphaELossFile,
                               InitialWire, FinalWire);
    }
  }
}
```

C.4 To Convert Raw Events to Physical Events

```
////////////////////////////////////////////////////////////////////////////////
// Script name: GetPhysicalEvents.C
//
// Description: Processes a file with raw data from ASIC, ADCs and TDCs channels
//              and, using the calibration constants converts the data to a list of
//              hits, for the SX3 detectors, with energy, detector number, triggered
//              back channel and front strip, and (x,y,z) hit coordinates; and for
//              the PC wires, the wire number, voltage and hit z-coordinate.
```

```
//
// Usage: root -l GetPhysicalEvents.C
//
// Created by: Daniel Santiago-Gonzalez
// Date: March 2013
////////////////////////////////////////////////////////////////////////////////
{
  //============================================================================
  // CONTROL PANEL
  //============================================================================
  // General parameters:
  string DataDir = "/data/ROOT_Files/";
  string TreeName = "DataTree";
  string ParamDir = "../Parameters/";
  string ASIC_map = "ASIC_channel_map.2013-05-17";
  string CAEN_map = "CAEN_channel_map.2013-03-25";
  string World_coords = "WorldCoordinates.2012-06-14";
  string SX3_CsI_combinations = "SX3_CsI_Combinations.2013-05-27";
  string SX3_PC_combinations = "SX3_PC_Combinations.2013-04-10";
  string InputDataFile = "r1215-24.root";
  string OutputPEFile = "PE_r1215-24.root";
  float DataFraction = 1.0;  // Select fraction of total data to be converted.
  // Number of detectors and maximum multiplicity:
  int N_Q3 = 0;
  int N_SX3 = 30;
  int N_PC = 19;
  int N_CsI = 36;
  int MaxMult = 10;
  // Define RF-time cut(s):
  const int T1Cuts = 1;
  float T1Low[T1Cuts]  = {0};
  float T1High[T1Cuts] = {4096};
  //============================================================================
  gSystem->Load("/DataAnalysisProject/ANASEN/EventProcessor_cpp.so");
  // Event processor.
  EventProcessor* EP = new EventProcessor();
  EP->SetSystemPointer(gSystem);
  EP->SetMaxMemory(8000);
  EP->SetTreeName(TreeName);
  EP->SetParamDirectory(ParamDir);
  EP->SetChannelMap(ASIC_map, CAEN_map, World_coords);
  EP->CreateDetectors(N_Q3, N_SX3, N_PC, N_CsI, MaxMult, SX3_PC_combinations,
                      SX3_CsI_combinations);
  EP->LoadDetectorsParameters();
  EP->CreatePhysicalEventsFile(DataDir + OutputPEFile);
  EP->OpenROOTFile(DataDir + InputDataFile);
  EP->SetBranches();
  if (T1Cuts>0)
    EP->SetTime1Cuts(T1Cuts, T1Low, T1High);
  EP->DataFraction = DataFraction;
  EP->ExtractData();
  EP->WritePhysicalEventsFile();
}
```

APPENDIX D

EXAMPLE OF SRIM OUTPUT

The following file was generated by the program SRIM[62] for α particles in a gas of molecular hydrogen (H_2) with pressure of 400 Torr and temperature of 294 K. The selected range of ion energy for which the stopping power values were calculated was from 0.5 MeV to 5.0 MeV.

```
 ==================================================================
              Calculation using SRIM-2006
 ==================================================================
 Ion = Helium [2] , Mass = 4.003 amu
 Target Density =  8.8140E-05 g/cm3 = 2.6353E+19 atoms/cm3
 Target is a GAS
 ======= Target  Composition ========
    Atom   Atom   Atomic    Mass
    Name   Numb   Percent   Percent
    ----   ----   -------   -------
      H      1    100.00    100.00
 ====================================
 Stopping Units =  MeV / mm

   Ion         dE/dx      dE/dx     Projected  Longitudinal   Lateral
  Energy       Elec.      Nuclear     Range     Straggling   Straggling
-----------  ---------- ---------- ----------  ----------  ----------
 500.00 keV   3.643E-02  3.944E-05   23.48 mm   734.09 um   849.83 um
 550.00 keV   3.657E-02  3.633E-05   24.85 mm   760.58 um   857.62 um
 600.00 keV   3.643E-02  3.371E-05   26.22 mm   786.10 um   864.88 um
 650.00 keV   3.608E-02  3.145E-05   27.60 mm   811.10 um   871.77 um
 700.00 keV   3.558E-02  2.950E-05   28.99 mm   835.86 um   878.37 um
 800.00 keV   3.426E-02  2.627E-05   31.85 mm   930.74 um   891.06 um
 900.00 keV   3.273E-02  2.372E-05   34.84 mm     1.02 mm   903.41 um
   1.00 MeV   3.114E-02  2.164E-05   37.97 mm     1.12 mm   915.70 um
   1.10 MeV   2.960E-02  1.991E-05   41.26 mm     1.21 mm   928.16 um
   1.20 MeV   2.814E-02  1.845E-05   44.72 mm     1.31 mm   940.93 um
   1.30 MeV   2.678E-02  1.720E-05   48.36 mm     1.41 mm   954.14 um
   1.40 MeV   2.553E-02  1.612E-05   52.19 mm     1.51 mm   967.89 um
   1.50 MeV   2.439E-02  1.517E-05   56.19 mm     1.61 mm   982.25 um
   1.60 MeV   2.334E-02  1.433E-05   60.38 mm     1.72 mm   997.30 um
   1.70 MeV   2.238E-02  1.359E-05   64.75 mm     1.83 mm     1.01 mm
   1.80 MeV   2.150E-02  1.292E-05   69.31 mm     1.94 mm     1.03 mm
   2.00 MeV   1.994E-02  1.177E-05   78.97 mm     2.38 mm     1.07 mm
   2.25 MeV   1.831E-02  1.061E-05   92.05 mm     3.02 mm     1.12 mm
   2.50 MeV   1.694E-02  9.664E-06  106.24 mm     3.63 mm     1.17 mm
   2.75 MeV   1.578E-02  8.881E-06  121.53 mm     4.23 mm     1.23 mm
   3.00 MeV   1.479E-02  8.221E-06  137.89 mm     4.82 mm     1.30 mm
```

```
  3.25 MeV   1.392E-02  7.656E-06  155.31 mm     5.42 mm     1.38 mm
  3.50 MeV   1.315E-02  7.168E-06  173.78 mm     6.02 mm     1.46 mm
  3.75 MeV   1.248E-02  6.740E-06  193.29 mm     6.63 mm     1.55 mm
  4.00 MeV   1.187E-02  6.364E-06  213.83 mm     7.24 mm     1.65 mm
  4.50 MeV   1.083E-02  5.728E-06  257.93 mm     9.57 mm     1.86 mm
  5.00 MeV   9.962E-03  5.213E-06  306.07 mm    11.75 mm     2.09 mm
=============================================================================
(C) 1984,1989,1992,1998,2008 by J.P. Biersack and J.F. Ziegler
```

BIBLIOGRAPHY

[1] R. Casten, *Nuclear Structure from a Simple Perspective*, Oxford science publications (Oxford University Press, 2000).

[2] S. DeBenedetti, *Nuclear Interactions* (John Wiley & Sons, Incorporated, 1964).

[3] M. G. Mayer, Phys. Rev. **75**, 1969 (1949).

[4] O. Haxel, J. H. D. Jensen, and H. E. Suess, Phys. Rev. **75**, 1766 (1949).

[5] S. Takeuchi, M. Matsushita, N. Aoi, P. Doornenbal, K. Li, T. Motobayashi, H. Scheit, D. Steppenbeck, H. Wang, H. Baba, D. Bazin, L. Càceres, H. Crawford, P. Fallon, R. Gernhäuser, J. Gibelin, S. Go, S. Grévy, C. Hinke, C. R. Hoffman, R. Hughes, E. Ideguchi, D. Jenkins, N. Kobayashi, Y. Kondo, R. Krücken, T. Le Bleis, J. Lee, G. Lee, A. Matta, S. Michimasa, T. Nakamura, S. Ota, M. Petri, T. Sako, H. Sakurai, S. Shimoura, K. Steiger, K. Takahashi, M. Takechi, Y. Togano, R. Winkler, and K. Yoneda, Phys. Rev. Lett. **109**, 182501 (2012).

[6] T. Otsuka, T. Suzuki, J. D. Holt, A. Schwenk, and Y. Akaishi, Phys. Rev. Lett. **105**, 032501 (2010).

[7] C. M. Campbell, N. Aoi, D. Bazin, M. D. Bowen, B. A. Brown, J. M. Cook, D.-C. Dinca, A. Gade, T. Glasmacher, M. Horoi, S. Kanno, T. Motobayashi, W. F. Mueller, H. Sakurai, K. Starosta, H. Suzuki, S. Takeuchi, J. R. Terry, K. Yoneda, and H. Zwahlen, Phys. Rev. Lett. **97**, 112501 (2006).

[8] B. Bastin, S. Grévy, D. Sohler, O. Sorlin, Z. Dombrádi, N. L. Achouri, J. C. Angélique, F. Azaiez, D. Baiborodin, R. Borcea, C. Bourgeois, A. Buta, A. Bürger, R. Chapman, J. C. Dalouzy, Z. Dlouhy, A. Drouard, Z. Elekes, S. Franchoo, S. Iacob, B. Laurent, M. Lazar, X. Liang, E. Liénard, J. Mrazek, L. Nalpas, F. Negoita, N. A. Orr, Y. Penionzhkevich, Z. Podolyák, F. Pougheon, P. Roussel-Chomaz, M. G. Saint-Laurent, M. Stanoiu, I. Stefan, F. Nowacki, and A. Poves, Phys. Rev. Lett. **99**, 022503 (2007).

[9] L. A. Riley, P. Adrich, T. R. Baugher, D. Bazin, B. A. Brown, J. M. Cook, P. D. Cottle, C. A. Diget, A. Gade, D. A. Garland, T. Glasmacher, K. E. Hosier, K. W. Kemper, T. Otsuka, W. D. M. Rae, A. Ratkiewicz, K. P. Siwek, J. A. Tostevin, Y. Utsuno, and D. Weisshaar, Phys. Rev. C **78**, 011303 (2008).

[10] P. Van Duppen, E. Coenen, K. Deneffe, M. Huyse, K. Heyde, and P. Van Isacker, Phys. Rev. Lett. **52**, 1974 (1984).

[11] O. Sorlin, D. Guillemaud-Mueller, A. C. Mueller, V. Borrel, S. Dogny, F. Pougheon, K.-L. Kratz, H. Gabelmann, B. Pfeiffer, A. Wöhr, W. Ziegert, Y. E. Penionzhkevich, S. M. Lukyanov, V. S. Salamatin, R. Anne, C. Borcea, L. K. Fifield, M. Lewitowicz, M. G. Saint-Laurent, D. Bazin, C. Détraz, F.-K. Thielemann, and W. Hillebrandt, Phys. Rev. C **47**, 2941 (1993).

[12] S. Grévy, J. C. Angélique, P. Baumann, C. Borcea, A. Buta, G. Canchel, W. N. Catford, S. Courtin, J. M. Daugas, F. de Oliveira, P. Dessagne, Z. Dlouhy, A. Knipper, K. L. Kratz, F. R. Lecolley, J. L. Lecouey, G. Lehrsenneau, M. Lewitowicz, E. Liénard, S. Lukyanov, F. Maréchal, C. Miehé, J. Mrazek, F. Negoita, N. A. Orr, D. Pantelica, Y. Penionzhkevich, J. Péter, B. Pfeiffer, S. Pietri, E. Poirier, O. Sorlin, M. Stanoiu, I. Stefan, C. Stodel, and C. Timis, Physics Letters B **594**, 252 (2004).

[13] S. Grévy, J. Mrazek, J. C. Angélique, P. Baumann, C. Borcea, A. Buta, G. Canchel, W. Catford, S. Courtin, J. M. Daugas, F. D. Oliveira, P. Dessagne, Z. Dlouhy, A. Knipper, K. L. Kratz, F. R. Lecolley, J. L. Lecouey, G. Lehrsenneau, M. Lewitowicz, E. Liénard, S. Lukianov, F. Maréchal, C. Miehé, F. Negoita, N. A. Orr, D. Pantelica, Y. Penionzhkevich, J. Péter, B. Pfeiffer, S. Pietri, E. Poirier, O. Sorlin, M. Stanoiu, C. Stodel, and C. Timis, Nuclear Physics A **722**, C424 (2003).

[14] R. Anne, D. Bazin, A. Mueller, J. Jacmart, and M. Langevin, Nuclear Instruments and Methods in Physics Research Section A: Accelerators, Spectrometers, Detectors and Associated Equipment **257**, 215 (1987).

[15] T. Glasmacher, B. Brown, M. Chromik, P. Cottle, M. Fauerbach, R. Ibbotson, K. Kemper, D. Morrissey, H. Scheit, D. Sklenicka, and M. Steiner, Physics Letters B **395**, 163 (1997).

[16] S. Grévy, F. Negoita, I. Stefan, N. Achouri, J. Angélique, B. Bastin, R. Borcea, A. Buta, J. Daugas, F. De Oliveira, O. Giarmana, C. Jollet, B. Laurent, M. Lazar, E. Liénard, F. Maréchal, J. Mrázek, D. Pantelica, Y. Penionzhkevich, S. Piétri, O. Sorlin, M. Stanoiu, C. Stodel, and M. St-Laurent, The European Physical Journal A - Hadrons and Nuclei **25**, 111 (2005).

[17] R. Anne and A. C. Mueller, Nuclear Instruments and Methods in Physics Research Section B: Beam Interactions with Materials and Atoms **70**, 276 (1992).

[18] C. Force, S. Grévy, L. Gaudefroy, O. Sorlin, L. Cáceres, F. Rotaru, J. Mrazek, N. L. Achouri, J. C. Angélique, F. Azaiez, B. Bastin, R. Borcea, A. Buta, J. M. Daugas, Z. Dlouhy, Z. Dombrádi, F. De Oliveira, F. Negoita, Y. Penionzhkevich,

M. G. Saint-Laurent, D. Sohler, M. Stanoiu, I. Stefan, C. Stodel, and F. Nowacki, Phys. Rev. Lett. **105**, 102501 (2010).

[19] H. Mach, M. Moszyski, R. Gill, F. Wohn, J. Winger, J. C. Hill, G. Molnr, and K. Sistemich, Physics Letters B **230**, 21 (1989).

[20] J. L. Wood, E. F. Zganjar, C. D. Coster, and K. Heyde, Nuclear Physics A **651**, 323 (1999).

[21] D. Morrissey, B. Sherrill, M. Steiner, A. Stolz, and I. Wiedenhoever, Nuclear Instruments and Methods in Physics Research Section B: Beam Interactions with Materials and Atoms **204**, 90 (2003).

[22] D. Bazin, J. Caggiano, B. Sherrill, J. Yurkon, and A. Zeller, Nuclear Instruments and Methods in Physics Research Section B: Beam Interactions with Materials and Atoms **204**, 629 (2003).

[23] W. Mueller, J. Church, T. Glasmacher, D. Gutknecht, G. Hackman, P. Hansen, Z. Hu, K. Miller, and P. Quirin, Nuclear Instruments and Methods in Physics Research Section A: Accelerators, Spectrometers, Detectors and Associated Equipment **466**, 492 (2001).

[24] R. York, H. Blosser, T. Grimm, D. Johnson, D. Lawton, F. Marti, J. Vincent, X. Wu, and A. F. Zeller, in *Particle Accelerator Conference, 1995., Proceedings of the 1995*, Vol. 1 (1995) pp. 345–347 vol.1.

[25] F. Marti, P. Miller, D. Poe, M. Steiner, J. Stetson, and X. Y. Wu, AIP Conference Proceedings **600**, 64 (2001).

[26] L. D. Landau and E. M. Lifshitz, *The Classical Theory of Fields*, Course of theoretical physics, Vol. 2 (Butterworth-Heinemann, 1975).

[27] D. Sohler, Z. Dombrádi, J. Timár, O. Sorlin, F. Azaiez, F. Amorini, M. Belleguic, C. Bourgeois, C. Donzaud, J. Duprat, D. Guillemaud-Mueller, F. Ibrahim, J. A. Scarpaci, M. Stanoiu, M. J. Lopez, M. G. Saint-Laurent, F. Becker, F. Sarazin, C. Stodel, G. Voltolini, S. M. Lukyanov, V. Maslov, Y.-E. Penionzhkevich, M. Girod, S. Péru, F. Nowacki, G. Sletten, R. Lucas, C. Theisen, D. Baiborodin, Z. Dlouhy, J. Mrazek, C. Borcea, A. Bauchet, C. J. Moore, and M. J. Taylor, Phys. Rev. C **66**, 054302 (2002).

[28] A. Artna-Cohen, Nuclear Data Sheets **79**, 1 (1996).

[29] *Standard reference material 4218-C*, National Bureau of Standards (1978).

[30] GEANT – Detector description and simulation tool, *CERN Program Library Long Writeup W5013*, Geneva (1993).

[31] J. A. Tostevin, G. Podolyák, B. A. Brown, and P. G. Hansen, Phys. Rev. C **70**, 064602 (2004).

[32] J. A. Tostevin and B. A. Brown, Phys. Rev. C **74**, 064604 (2006).

[33] E. C. Simpson, J. A. Tostevin, D. Bazin, B. A. Brown, and A. Gade, Phys. Rev. Lett. **102**, 132502 (2009).

[34] E. C. Simpson, J. A. Tostevin, D. Bazin, and A. Gade, Phys. Rev. C **79**, 064621 (2009).

[35] E. C. Simpson and J. A. Tostevin, Phys. Rev. C **82**, 044616 (2010).

[36] F. Nowacki and A. Poves, Phys. Rev. C **79**, 014310 (2009).

[37] O. Tarasov and D. Bazin, Nuclear Instruments and Methods in Physics Research Section B: Beam Interactions with Materials and Atoms **266**, 4657 (2008).

[38] J. Fridmann, I. Wiedenhöver, A. Gade, L. T. Baby, D. Bazin, B. A. Brown, C. M. Campbell, J. M. Cook, P. D. Cottle, E. Diffenderfer, D.-C. Dinca, T. Glasmacher, P. G. Hansen, K. W. Kemper, J. L. Lecouey, W. F. Mueller, E. Rodriguez-Vieitez, J. R. Terry, J. A. Tostevin, K. Yoneda, and H. Zwahlen, Phys. Rev. C **74**, 034313 (2006).

[39] A. Volya and V. Zelevinsky, Phys. Rev. C **74**, 064314 (2006).

[40] A. Volya, *http://www.volya.net*.

[41] G. F. Knoll, *Radiation detection and measurement* (Wiley, 2000).

[42] W. Press, *Numerical Recipes: The Art of Scientific Computing*, 3rd ed. (Cambridge University Press, 2007).

[43] D. Santiago-Gonzalez, I. Wiedenhöver, V. Abramkina, M. L. Avila, T. Baugher, D. Bazin, B. A. Brown, P. D. Cottle, A. Gade, T. Glasmacher, K. W. Kemper, S. McDaniel, A. Rojas, A. Ratkiewicz, R. Meharchand, E. C. Simpson, J. A. Tostevin, A. Volya, and D. Weisshaar, Phys. Rev. C **83**, 061305 (2011).

[44] M. Thoennessen, Reports on Progress in Physics **67**, 1187 (2004).

[45] M. Fauerbach, D. J. Morrissey, W. Benenson, B. A. Brown, M. Hellström, J. H. Kelley, R. A. Kryger, R. Pfaff, C. F. Powell, and B. M. Sherrill, Phys. Rev. C **53**, 647 (1996).

[46] C. R. Hoffman, T. Baumann, D. Bazin, J. Brown, G. Christian, P. A. DeYoung, J. E. Finck, N. Frank, J. Hinnefeld, R. Howes, P. Mears, E. Mosby, S. Mosby, J. Reith, B. Rizzo, W. F. Rogers, G. Peaslee, W. A. Peters, A. Schiller, M. J. Scott, S. L. Tabor, M. Thoennessen, P. J. Voss, and T. Williams, Phys. Rev. Lett. **100**, 152502 (2008).

[47] M. H. Macfarlane and J. B. French, Rev. Mod. Phys. **32**, 567 (1960).

[48] C. Iliadis, *Nuclear Physics of Stars* (Wiley, 2008).

[49] B. Harss, R. C. Pardo, K. E. Rehm, F. Borasi, J. P. Greene, R. V. F. Janssens, C. L. Jiang, J. Nolen, M. Paul, J. P. Schiffer, R. E. Segel, J. Specht, T. F. Wang, P. Wilt, and B. Zabransky, Review of Scientific Instruments **71**, 380 (2000).

[50] A. Wuosmaa, J. Schiffer, B. Back, C. Lister, and K. Rehm, Nuclear Instruments and Methods in Physics Research Section A: Accelerators, Spectrometers, Detectors and Associated Equipment **580**, 1290 (2007).

[51] J. Lighthall, B. Back, S. Baker, S. Freeman, H. Lee, B. Kay, S. Marley, K. Rehm, J. Rohrer, J. Schiffer, D. Shetty, A. Vann, J. Winkelbauer, and A. Wuosmaa, Nuclear Instruments and Methods in Physics Research Section A: Accelerators, Spectrometers, Detectors and Associated Equipment **622**, 97 (2010).

[52] C. R. Hoffman, B. B. Back, B. P. Kay, J. P. Schiffer, M. Alcorta, S. I. Baker, S. Bedoor, P. F. Bertone, J. A. Clark, C. M. Deibel, B. DiGiovine, S. J. Freeman, J. P. Greene, J. C. Lighthall, S. T. Marley, R. C. Pardo, K. E. Rehm, A. Rojas, D. Santiago-Gonzalez, D. K. Sharp, D. V. Shetty, J. S. Thomas, I. Wiedenhöver, and A. H. Wuosmaa, Phys. Rev. C **85**, 054318 (2012).

[53] B. A. Brown and W. A. Richter, Phys. Rev. C **74**, 034315 (2006).

[54] A. Rojas, *Experimental study of the proton capture on ^{25}Al using the ^{25}Al(d,n)^{26}Si reaction in inverse kinematics*, Ph.D. thesis, The Florida State University (2010).

[55] D. Tilley, H. Weller, C. Cheves, and R. Chasteler, Nuclear Physics A **595**, 1 (1995).

[56] M. Matos, J. C. Blackmon, L. E. Linhardt, L. L. Mondello, E. Johnson, G. Rogachev, and I. Wiedenhöver, in *11th Symposium on Nuclei in the Cosmos*, Vol. 1 (2010) p. 226.

[57] M. M. Bé, V. Chisté, C. Dulieu, E. Browne, V. Chechev, N. Kuzmenko, R. Helmer, A. Nichols, E. Schönfeld, and R. Dersch, *Table of Radionuclides*, Monographie BIPM-5, Vol. 2 (Bureau International des Poids et Mesures, Pavillon de Breteuil, F-92310 Sèvres, France, 2004).

[58] M. M. Bé, V. Chisté, C. Dulieu, E. Browne, V. Chechev, N. Kuzmenko, F. Kondev, A. Luca, M. Galán, A. Pearce, and X. Huang, *Table of Radionuclides*, Monographie BIPM-5, Vol. 4 (Bureau International des Poids et Mesures, Pavillon de Breteuil, F-92310 Sèvres, France, 2008).

[59] M. M. Bé, V. Chisté, C. Dulieu, X. Mougeot, V. P. Chechev, F. G. Kondev, A. L. Nichols, X. Huang, and B. Wang, *Table of Radionuclides*, Monographie BIPM-5, Vol. 7 (Bureau International des Poids et Mesures, Pavillon de Breteuil, F-92310 Sèvres, France, 2013).

[60] H. Bethe, Annalen der Physik **397**, 325 (1930).

[61] F. Bloch, Annalen der Physik **408**, 285 (1933).

[62] J. F. Ziegler, Nuclear Instruments and Methods in Physics Research Section B: Beam Interactions with Materials and Atoms **219220**, 1027 (2004), Proceedings of the Sixteenth International Conference on Ion Beam Analysis.

[63] M. Morháč and V. Matoušek, Appl. Spectrosc. **62**, 91 (2008).

[64] D. Tilley, C. Cheves, J. Kelley, S. Raman, and H. Weller, Nuclear Physics A **636**, 249 (1998).

BIOGRAPHICAL SKETCH

Daniel Santiago-Gonzalez was born in Monterrey, México, on May 21st, 1983. On August 2001 he entered the school of Physics and Mathematics of the Universidad Autónoma de Nuevo León, where he finished all the courses on December 2005. He started his undergraduate thesis project on nanoparticles of Au-Pd on the last semester of his undergraduate studies and obtained his B.S. in Physics on July 2007. While he was working on his thesis he also took preparatory courses to enter the Ph.D. program of the Physics Institute of the Universidad de Guanajuato. Although he was accepted in that program, he decided to pursue a Ph.D. degree in the U.S.A. On August 2007 he started his doctoral studies at Florida State University where, shortly afterwards, he joined the group of Experimental Nuclear Physics under the supervision of Dr. Ingo Wiedenhöver. He is the first author of the article "Triple configuration coexistence in ^{44}S" published in Phys. Rev. C 83, 061305(R). On March 2012 he accepted a postdoctoral offer to work at Argonne National Laboratory under the direction of Catherine Deibel of Louisiana State University. He successfully defended his Ph.D. dissertation on November 12th, 2013.